Astronomy Reports, Vol. 48, No. 4, 2004, pp. 261–266. Translated from Astronomicheskiĭ Zhurnal, Vol. 81, No. 4, 2004, pp. 291–297.
Original Russian Text Copyright © 2004 by Bogdanov, Cherepashchuk.

Analysis of a High-Amplitude Event in Component A of the Gravitational Lens QSO 2237+0305

M. B. Bogdanov[1] **and A. M. Cherepashchuk**[2]

[1]*Chernyshevskiĭ University, Saratov, Russia*
[2]*Sternberg Astronomical Institute, Universitetskiĭ pr. 13, Moscow, 119992 Russia*

Received June 28, 2003; in final form, November 10, 2003

Abstract—We present an analysis of a high-amplitude event in the flux curve of component A of the gravitational lens QSO 2237+0305 observed by the OGLE and GLITP groups in autumn 1999. Hypothesizing this event to be associated with microlensing of a fold caustic, we analyzed the observational data using a method for the successive reconstruction of branches of the one-dimensional strip brightness distribution across the source corresponding to positive and negative arguments. The search for the branches was carried out on compact sets of nonnegative, monotonically nonincreasing, convex downward functions. The resulting shape of the strip brightness distribution for the accretion disk of the quasar is in agreement with results obtained earlier via model fitting. Features in the lensing curve that could be associated with curvature of the caustic, nearness of a cusp, or the influence of nearby caustics are noted.

1. INTRODUCTION

According to our current understanding, the main source of the energy of quasars and other active galactic nuclei is accretion onto a supermassive black hole. The properties of the accretion disk that is formed determine to an appreciable extent the observed characteristics of these objects. One way to study accretion processes is via spectral analyses. Such studies have yielded most of the currently available information, with the most interesting results being derived from analyses of the profile of the iron K_α X-ray line, believed to be emitted in the central regions of the accretion disk [1].

Another independent way to obtain information about the accretion processes is to investigate the spatial structure of the disk, which requires observations with very high angular resolution, exceeding a microarcsecond. In spite of the seemingly unrealistic smallness of this figure, a proposed space X-ray interferometer project would in fact provide this resolution [2]. However, a similar resolution can be obtained in the visible using observations of gravitational lens systems: intervening galaxies that give rise to multiple images of distant quasars. Microlensing by stars in the lensing galaxy produces a random field of caustics, which can lead to a high-amplitude event in the measured fluxes from the images when a caustic crosses the accretion disk of the quasar [3, 4]. The most probable type of microlensing occurs when a fold caustic intersects the disk, in which case the observed flux-variation curve contains information about the one-dimensional strip brightness distribution across the disk in the direction of the local normal to the caustic.

The gravitational lens QSO 2237+0305, which is also called Huchra's lens or the Einstein cross, is the best known representative of this class of object. Four images of a distant ($z_s = 1.695$) quasar are created by the gravitational field of a fairly nearby ($z_d = 0.0394$) galaxy that is lying nearly in the line of sight to the observer. As a result, the time delay between the images is less than a day, and the characteristic duration of microlensing events should be several tens of days. Uncorrelated fluctuations in the fluxes from the different images that were probably associated with microlensing by stars in the lensing galaxy were first detected by Irwin *et al.* [5] and used to estimate the size of the accretion disk [6, 7]. Later, various groups of observers monitored this object in hopes of detecting the effects of microlensing [8–11].

The most complete series of observations, obtained by the international OGLE group [12, 13], demonstrated the presence of possible high-amplitude events in components A (in 1998) and C (in summer 1999). The data for these events were analyzed with the aim of deriving the size of the accretion disk, both using statistical methods [14, 15] and via model fitting of the brightness distribution for a circularly symmetrical source [16, 17]. The analysis of the high-amplitude event for component C also yielded a reconstructed strip brightness distribution for the accretion disk [18].

1063-7729/04/4804-0261$26.00 © 2004 MAIK "Nauka/Interperiodica"

Alcalde *et al.* [19] recently presented observations by the GLITP group that nicely supplement the data of the OGLE group in autumn 1999; these display a high-amplitude event in component A. Based on the hypothesis that this event was associated with microlensing by a fold caustic, these observations were analyzed by fitting both symmetric source models [20] and a model brightness distribution of the form expected for a standard geometrically thin and optically thick Newtonian accretion disk [21] surrounding a Schwartschild black hole, allowing for the inclination of the plane of the disk to the line of sight [22]. In the latter case, it was possible to derive constraints on the mass of the black hole at the center of the quasar: $10^7 M_\odot < M < 6 \times 10^8 M_\odot$.

Together with many advantages, model fitting also has certain disadvantages. The main one is the possibility that the model is inadequate as a description of the real object. It is clear, for example, that the possibility that the plane of the disk is inclined to the line of sight makes circularly symmetrical models potentially inadequate. Similarly, there is a good basis to suppose that there should be a Kerr black hole rotating at close to the maximum rotation rate at the center of a quasar [1]. In this case, the accretion disk is appreciably relativistic. The edge of the rotating disk that is approaching the observer will appear to be brighter than the receding edge, leading to a loss of symmetry in the strip brightness distribution of the disk [18]. Therefore, model-independent methods for the analysis of observational data based on the reconstruction of the brightness distribution are especially important.

Here, we analyze the variability curve for a high-amplitude event observed by the OGLE and GLITP groups in component A of the gravitational lens QSO 2237+0305 in autumn 1999, in order to derive the shape of the strip brightness distribution for the accretion disk of the lensed quasar.

2. OBSERVATIONAL DATA

We obtained the V-band fluxes of component A (in millijansky, mJy) measured by the OGLE and GLITP groups (PSFphotII photometry) from these groups' servers over the Internet. The GLITP data, $I_G(t_i)$, form a fairly dense series but cover only the upper part of the ascending branch and the maximum of the flux-variation curve. The OGLE data, $I_O(t_i)$, were more sparse but cover the lower part of the ascending branch of the curve well. Therefore, we decided to use both of these photometric series in our subsequent analysis.

When the OGLE and GLITP photometric data are plotted together, it is obvious that there is an offset between them and that the $I_O(t_i)$ values exceed the $I_G(t_i)$ values measured at the same epochs. Since this offset is not large, and the data obtained in each photometric system cover a fairly extensive time interval with appreciable flux variations, we decided to unify the data series by assuming a linear relation between them: $I_O(t_i) = aI_G(t_i) + b$. The coefficients in this relation were determined from a least-squares fit with a linear interpolation of the $I_G(t_i)$ values in the overlapping time interval and were found to be $a = 1.125$ and $b = -0.042$. Figure 1 shows the flux measurements in the OGLE photometric system as a function of the modified Julian date, JD − 2450000.0. The filled and hollow circles show the OGLE and GLITP observations. The vertical line segments indicate intervals corresponding to two standard deviations ($\pm\sigma$). The flux values do not display systematic differences, and the unified series of observations is fairly uniform.

3. METHOD FOR RECONSTRUCTING THE STRIP BRIGHTNESS DISTRIBUTION

Let us suppose that the image of a quasar accretion disk is scanned by a fold caustic, which can be taken to have the form of a straight line due to the small angular size of the disk. Let $b(x, y)$ be the brightness distribution in the disk for a distant external observer in a Cartesian coordinate system (x, y) in the plane of the sky, with the x axis oriented perpendicular to the caustic and the coordinate origin coincident with the center of the disk. The observed lensing curve will then depend only on the one-dimensional strip brightness distribution $B(x)$, defined by the expression

$$B(x) = \int_{-\infty}^{\infty}\int_{-\infty}^{\infty} b(\xi, y)\delta(\xi - x)d\xi dy, \qquad (1)$$

where $\delta(x)$ is the Dirac delta function. When the intersection of the caustic leads to the appearance of additional images of the source accompanied by a sharp amplification of the flux, the lensing curve $I(x)$ is given by the convolution equation

$$I(x) = A(x) * B(x) = \int_{-\infty}^{\infty} A(x - \xi)B(\xi)d\xi, \qquad (2)$$

whose core has the form [23–25]

$$A(x - \xi) = A_0 + \frac{K}{\sqrt{x - \xi}}H(x - \xi), \qquad (3)$$

where $H(x - \xi)$ is the Heaviside step function, which is equal to zero for negative and unity for positive values of its argument. The quantity A_0 in (3) depends on the flux from all remaining images of the source, which remains constant during the intersection of the caustic, and the factor K characterizes the amplification of the caustic. The values of A_0 and K are usually not known. Thus, reconstruction of the strip brightness distribution involves solving the inverse problem for integral equation (2), which is an ill-posed problem.

When (3) is substituted into (2), we can see that A_0 determines the initial flux level I_0, which is a free parameter of the problem. The absence of information about K means that $B(x)$ can be reconstructed only to within a constant factor. The second free parameter is the time when the caustic passes through the center of the disk t_0, which defines the origin for the x axis. If the projection of the tangential velocity of the caustic onto this axis is $V_\perp$, the time dependence of the spatial variable x has the form $x = V_\perp(t - t_0)$. As for the parameter K from (3), the scanning velocity $V_\perp$ is, in general, unknown. Setting $K = 1$ and $V_\perp = 1$ and assuming $x = t - t_0$, we can reconstruct only the shape of the strip brightness distribution from microlensing observations.

The solution of the ill-posed inverse problem for integral equation (2) requires the application of regularizing algorithms that are stable against noise. This problem was first considered in [26], where the solution was found using the regularization method of Tikhonov. Methods for reconstructing the radial brightness distribution assuming a circularly symmetrical source [27] and in the locally comoving space of the accretion taking into account relativistic effects [28] have also been proposed. These analyses also applied regularization methods to solve the main integral equation. However, the presence of free parameters gives rise to certain difficulties. The parameter t_0 does not play a significant role in the reconstruction of the strip brightness distribution: we can see from (2) that a shift in the beginning of the measurement time leads only to a corresponding shift in the reconstructed profile $B(x)$ without changing its shape. In contrast, knowledge of I_0 is required in any case.

At first glance, it seems possible to simply estimate the initial flux level I_0 based on a best agreement with the observations. However, this automatically makes it impossible to apply the regularization method of Tikhonov to reconstruct the strip brightness distribution. The approximate solution yielded by this method is the smoothest function whose lensing curve is in agreement with the observations within the estimated errors [29, 30]. We will obtain a family of strip brightness distributions by varying the input flux level. All functions in this family, including those that have no physical meaning, will give the same residual when compared with the observations. There are no criteria that can be used to choose one of these functions as the best approximate solution. Imposing additional constraints on the brightness distribution (requiring that it be positive, for example) narrows the family of functions but does not completely eliminate this problem. Moreover, the regularization method makes the minimum use of *a priori* information about the solution of the ill-posed problem and is therefore not able to provide good stability of the solution against the effect of random noise.

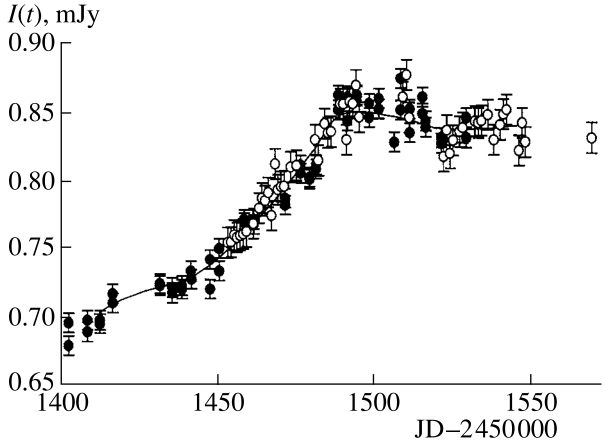

Fig. 1. Flux-variation curve for component A of the gravitational lens QSO 2237+0305 in the V band from OGLE (filled circles) and GLITP (hollow circles) observations. The solid curve corresponds to our reconstruction of the strip brightness distribution.

We have proposed a method for analyzing observations of high-amplitude events that is free from the drawbacks of the regularization method and enables the derivation of an unambiguous estimate of the strip brightness distribution that is stable against random noise [18]. This method is based on the properties of the core of (3), thanks to which only one branch of $B(x)$ participates in the formation of one branch of the lensing curve $I(x)$ (the negative branch when the source enters the caustic or the positive branch when it leaves the caustic), while both branches of the strip brightness distribution influence the other branch of $I(x)$. This makes it possible to realize a successive reconstruction of the branches of $B(x)$ by searching for them on compact sets of either nonnegative, monotonically nonincreasing functions or nonnegative, monotonically nonincreasing convex downward functions. In this case, the values of the free parameters I_0 and t_0 can be determined from the minimum residual corresponding to the reconstructed function $B(x)$, which is usually found using the sum of the squared deviations, the quantity χ^2_N. Since the set of functions on which the search for the solution is carried out is compact, this guarantees that the obtained profiles $B(x)$ and the values of the free parameters will approach their real values as the errors in the estimate of the flux $I(x)$ approach zero [29, 30].

The use of a large amount of *a priori* information about the possible form of the brightness distribution in accordance with the physics involved enables us to achieve a solution with a high degree of stability against the effects of noise.

We should note one other important circumstance, which has usually been neglected in the studies cited above. The main integral equation (2) has the singular core (3). When calculating such integrals, it is necessary to take special measures to ensure convergence of the corresponding integral sums. In particular, attempts to calculate the values $I(x_i)$ on a nonuniform grid x_i when $B(\xi_i)$ is specified on a uniform grid ξ_i can lead to large errors in the results. General questions with regard to the application of numerical methods for singular integral equations are considered in [31]. A simple proof of a sufficient condition for the convergence of the integral sum for the specific case of (2) and the core (3) is presented in [32]. This condition consists of the special selection of grids forming a so-called canonical division of the integration interval. Both grids are uniform, and either $\xi_i = (x_i + x_{i+1})/2$ or an integral number of grid steps $\Delta\xi$ fit into the interval Δx, with the points ξ_i being the centers of these intervals. The time spans between measurements in the observed flux curves are usually nonuniform. Therefore, the model curves that are to be fit to the observations must first be calculated on a uniform grid, then interpolated to the times of the observations. When reconstructing the brightness distribution, the observed values $I(x_i)$ must first be interpolated to the uniform grid.

4. RECONSTRUCTION OF THE STRIP BRIGHTNESS DISTRIBUTION

We used the method for the successive reconstruction of the branches of the strip brightness distribution of [18] to analyze the master series of photometric data for component A of the gravitational lens QSO 2237+0305 presented in Fig. 1. Adopting $V_\perp = 1$ and $x = t - t_0$, we measure the distance x and the variable of the integration ξ in units of time. The first version of the canonical division, with $\xi_i = (x_i + x_{i+1})/2$ and the intervals $\Delta\xi = \Delta x = 2^{\mathrm{d}}$, was used to obtain a numerical estimate of integral (2). The flux-variation curve was linearly interpolated onto a uniform grid with $N = 69$ points in the interval $[t_0 - 68^{\mathrm{d}}, t_0 + 68^{\mathrm{d}}]$. The search for the strip brightness distribution was carried out on a grid of $M = 68$ points in the interval $[-67^{\mathrm{d}}, 67^{\mathrm{d}}]$. The values of the free parameters I_0 and t_0 that yield the minimum residual

$$\chi^2_N = \sum_{i=1}^{N} [(I_o(x_i) - I_c(x_i))/\sigma_i]^2$$

were found via a simple exhaustive search (here, N is the number of measurements of the lensing curve $I_o(x_i)$, σ_i are the estimated errors for these measurements, and $I_c(x_i)$ are the flux values corresponding to the reconstructed strip brightness distribution). The best-fit values of the parameters were $I_0 = 0.697 \pm 0.001$ mJy and $t_0 = 1479.4 \pm 0.1^{\mathrm{d}}$. These are fairly close to the values obtained via model-fitting of the GLITP observations [20].

The values for the reconstructed branches of the strip brightness distribution are shown by the circles in Fig. 2 and the lensing curve corresponding to the derived strip brightness distribution by the solid curve in Fig. 1. The minimum residual was $\chi^2_N = 37.2$; the χ^2_N value corresponding to a 50% probability that the curve is in agreement with the data for the case of $N = 69$ degrees of freedom is 68.3. Thus, the agreement with the observations is fairly good. This is confirmed by Fig. 1, where we can see that the calculated flux-variation curve tracks the observed counts well. At the same time, the curve is not completely consistent with the expected shape of the lensing curve expected for a fold caustic. This is especially noticeable in the interval following the flux maximum, where a deviation from monotonic behavior is observed. This was also pointed out in connection with model-fitting of the brightness distribution [20]. It is possible that curvature of the caustic, nearness to a cusp, or the influence of other nearby caustics is manifest in this high-amplitude event.

The presence of possible deviations from a simple model with a linear caustic is also reflected by the shape of the reconstructed strip brightness distribution. We can see in Fig. 2 that the two branches differ appreciably. The shape of the positive branch is close to the expected strip brightness distribution for a relativistic accretion disk [18], while the negative branch forms a simple straight line segment. Nevertheless, the derived strip brightness distribution is in agreement with the results of fitting the GLITP data with a model for a standard Newtonian accretion disk, whose radius in time units proved to be 39.6^{d} [20].

5. ESTIMATED SIZE OF THE ACCRETION DISK

As was already noted above, if the time for the intersection of the source by the caustic is known, the linear size of the source can be derived from the projection of the tangential velocity of the caustic onto the axis normal to the caustic, $V_\perp$. In addition, the time of intersection of the accretion disk depends on the inclination of the plane of the disk to the line of sight and the direction of the motion of the caustic relative to the major axis of the ellipse corresponding

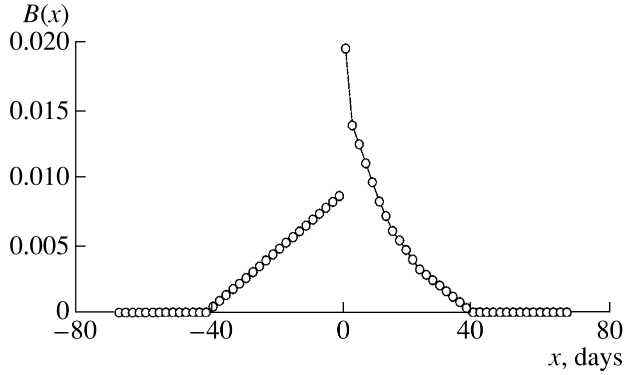

Fig. 2. The branches of the reconstructed strip brightness distribution for the accretion disk of the gravitationally lensed quasar QSO 2237+0305. The caustic scanning rate was taken to be unity.

to the projection of the disk onto the plane of the sky. Therefore, even if $V_\perp$ is known very accurately, we can determine only a lower limit for the linear size of the disk from the strip brightness distribution.

Let us project the spatial-velocity vectors of all the objects participating in the high-amplitude event onto a plane perpendicular to the line of sight from the observer to the center of the accretion disk. We denote $\mathbf{V}_s$, $\mathbf{V}_d$, and $\mathbf{V}_o$ to be the two-dimensional projected velocities of the source, gravitational lens, and observer, respectively. As was shown in [4], the projection of the motion of the caustic onto this plane $\mathbf{V}$ can be written as

$$\mathbf{V} = \frac{\mathbf{V}_s}{1+z_s} - \frac{\mathbf{V}_d}{1+z_d}\frac{D_s}{D_d} + \frac{\mathbf{V}_o}{1+z_d}\frac{D_{ds}}{D_d}, \quad (4)$$

where z_s and z_d are the redshifts of the quasar and gravitational lens and D_s, D_d, and D_{ds} are the angular-diameter distances between the observer and quasar, the observer and lens, and the lens and quasar, respectively. For the parameters of the gravitational lens QSO 2237+0305 ($z_s = 1.695$, $z_d = 0.0394$) and reasonable velocities for the motions involved, the second term in (4) is the determining one. Therefore, we can obtain for the velocity with which the source is scanned by the caustic

$$V_\perp \approx \frac{V_{\perp,d}}{1+z_d}\frac{D_s}{D_d}, \quad (5)$$

where $V_{\perp,d}$ is the projection of $\mathbf{V}_d$ onto the local normal to the caustic.

The precise value of $V_\perp$ is not known. A statistical analysis of the peculiar velocities of galaxies in [22] yielded the mean value 663 km/s, while the range of the projected velocity $V_{\perp,d}$ for the 90% confidence interval was roughly $100 \le V_{\perp,d}$ (km/s) ≤ 1000. The distances D_d and, especially, D_s in (5) depend on cosmological parameters. Taking into account possible variations from a flat Universe ($\Omega_0 = 1$) and models with a dominance of the vacuum energy consistent with modern observational data ($\Omega_0 = 0.3$, $\lambda_0 = 0.7$), the interval of possible caustic-scanning velocities $V_\perp$ becomes $765 \le V_\perp$ (km/s) $\le 10\,548$ [22]. If we formally adopt a value in the middle of this interval, $V_\perp = 5600$ km/s, the intersection time for the profile of the strip brightness distribution is 80^d (Fig. 2), which corresponds to a linear size of 3.9×10^{15} cm, or 1.3×10^{-3} pc.

6. CONCLUSIONS

We have analyzed a high-amplitude event in component A of the gravitational lens QSO 2237+0305 observed by the international OGLE and GLITP groups in autumn 1999 using a model-independent method developed by us earlier. This analysis has yielded an estimate of the shape of the strip brightness distribution of the accretion disk of the lensed quasar. Our results are consistent with the results of model-fitting to the GLITP observations and can be used to estimate the size of the accretion disk. Features in the flux-variation curve and the strip brightness distribution suggest that the disk was not scanned by a simple linear fold caustic. It is possible that curvature of the caustic, nearness to a cusp, or the influence of other nearby caustics is manifest in the details of the curve for this high-amplitude event.

It is of interest to compare the reconstructed brightness distribution with the results obtained earlier in our analysis of a high-amplitude event in component C of this same gravitational lens [18]. In that case, the shape of the strip brightness distribution corresponded to that expected for a relativistic accretion disk around a supermassive black hole. The shape of the flux-variation curve was also in good agreement with the curve expected if the disk was scanned by a linear caustic. The time for the scan of the strip brightness distribution was appreciably longer for the event in component C, 300^d. This could be due to a difference in either the scanning velocity or the direction of the caustic's motion relative to the major axis of the elliptical projection of the quasar's accretion disk onto the plane of the sky.

ACKNOWLEDGMENTS

The authors thank the OGLE and GLITP groups for the opportunity to obtain the observational material used in this study. This work was partially supported by the Federal Science and Technology Program in Astronomy, the Russian Foundation for Basic Research (project code 02-02-17524), and the program "Universities of Russia."

REFERENCES

1. J. H. Krolik, *Active Galactic Nuclei* (Princeton Univ. Press, Princeton, 1999).
2. N. White, Nature **407**, 146 (2000).
3. B. Paczynski, Astrophys. J. **301**, 503 (1986).
4. R. Kayser, S. Refsdal, and R. Stabell, Astron. Astrophys. **166**, 36 (1986).
5. M. J. Irwin, R. L. Webster, P. C. Hewitt, *et al.,* Astron. J. **98**, 1989 (1989).
6. K. P. Rauch and R. D. Blandford, Astrophys. J. **381**, L39 (1991).
7. M. Jaroszynski, J. Wambsganss, and B. Paczynski, Astrophys. J. **396**, L65 (1992).
8. R. T. Corrigan, M. J. Irwin, J. Arnaud, *et al.,* Astron. J. **102**, 34 (1991).
9. R. Ostensen, S. Refsdal, R. Stabell, *et al.*, Astron. Astrophys. **309**, 590 (1996).
10. V. G. Vakulik, V. N. Dudinov, A. P. Zheleznyak, *et al.*, Astron. Nachr. **318**, 73 (1997).
11. R. W. Schmidt, T. Kundic, U.-L. Pen, *et al.*, Astron. Astrophys. **392**, 773 (2002).
12. P. R. Wozniak, C. Alard, A. Udalski, *et al.*, Astrophys. J. **529**, 88 (2000).
13. P. R. Wozniak, A. Udalski, M. Szymanski, *et al.*, Astrophys. J. **540**, 65 (2000).
14. J. S. B. Wyithe, R. L. Webster, E. L. Turner, and D. J. Mortlock, Mon. Not. R. Astron. Soc. **315**, 62 (2000).
15. J. S. B. Wyithe, R. L. Webster, and E. L. Turner, Mon. Not. R. Astron. Soc. **318**, 1120 (2000).
16. V. N. Shalyapin, Pis'ma Astron. Zh. **27**, 180 (2001) [Astron. Lett. **27**, 150 (2001)].
17. A. Yonehara, Astrophys. J. **548**, L127 (2001).
18. M. B. Bogdanov and A. M. Cherepashchuk, Astron. Zh. **79**, 693 (2002) [Astron. Rep. **46**, 626 (2002)].
19. D. Alcalde, E. Mediavilla, O. Moreau, *et al.*, Astrophys. J. **572**, 729 (2002).
20. V. N. Shalyapin, L. J. Goicoechea, D. Alcalde, *et al.*, Astrophys. J. **579**, 127 (2002).
21. N. I. Shakura and R. A. Sunyaev, Astron. Astrophys. **24**, 337 (1973).
22. L. J. Goicoechea, D. Alcalde, E. Mediavilla, and A. Munoz, Astron. Astrophys. **397**, 517 (2003).
23. P. Schneider, J. Ehlers, and E. E. Falco, *Gravitational Lenses* (Springer, Berlin, 1992).
24. A. F. Zakharov, *Gravitational Lenses and Microlenses* (Yanus-K, Moscow, 1997), p. 328 [in Russian].
25. B. S. Gaudi and A. O. Petters, Astrophys. J. **574**, 970 (2002).
26. B. Grieger, R. Kayser, and T. T. Schramm, Astron. Astrophys. **252**, 508 (1991).
27. S. Mineshige and A. Yonehara, Publ. Astron. Soc. Jpn. **51**, 497 (1999).
28. E. Agol and J. Krolik, Astrophys. J. **524**, 49 (1999).
29. A. N. Tikhonov, A. V. Goncharskiĭ, V. V. Stepanov, and A. G. Yagola, *Regularization Algorithms and a priori Information* (Nauka, Moscow, 1983), p. 200 [in Russian].
30. A. V. Goncharskiĭ, A. M. Cherepashchuk, and A. G. Yagola, *Ill-Posed Problems in Astrophysics* (Nauka, Moscow, 1985), p. 352 [in Russian].
31. S. M. Belotserkovskiĭ and I. K. Lifanov, *Numerical Methods for Singular Integral Equations and Their Application to Aerodynamics, Elasticity Theory, and Electrodynamics* (Nauka, Moscow, 1985), p. 256 [in Russian].
32. M. B. Bogdanov, astro-ph/0102031 (2001).

Translated by D. Gabuzda

Astronomy Reports, Vol. 48, No. 4, 2004, pp. 267–274. Translated from Astronomicheskiĭ Zhurnal, Vol. 81, No. 4, 2004, pp. 298–305.
Original Russian Text Copyright © 2004 by Karachentsev, Karachentseva.

New Dwarf Galaxy Candidates in the Leo-I Group

I. D. Karachentsev[1] **and V. E. Karachentseva**[2]

[1]*Special Astrophysical Observatory, Russian Academy of Sciences, Nizhniĭ Arkhyz,*
Karachaĭ-Cherkessian Republic, 357147 Russia

[2]*Astronomical Observatory, Kiev Taras Shevchenko National University, Observatorna str.,*
Kiev, 304053 Ukraine

Received August 15, 2003; in final form, November 10, 2003

Abstract—We have carried out a search for low-surface-brightness dwarf galaxies in the region of the Leo-I Group (M96) in images of the second Palomar Sky Survey. We found a total of 36 likely dwarf members of the group with typical magnitudes $B_t \sim 18^m$–19^m in an area of sky covering 120 square degrees. Half of these galaxies are absent from known catalogs and lists of galaxies. The radial-velocity dispersion calculated for 19 galaxies is 130 km/s. The Leo-I Group has a mean distance from the Sun of 10.4 Mpc, a mean projected radius of 352 kpc, an integrated luminosity of $6.7 \times 10^{10}\,L_\odot$, a virial mass-to-luminosity ratio of $107\,M_\odot/L_\odot$, and a mean crossing time of 2.7 Gyr. The group shows evidence for a radial segregation of the galaxies according to morphological type and luminosity, suggesting that the group is in a state of dynamical relaxation. The subsystem of bright galaxies in the Leo-I Group is smaller in size (250 kpc) and has a lower velocity dispersion (92 km/s), resulting in a lower virial mass-to-luminosity ratio ($34\,M_\odot/L_\odot$), as is typical of the Local Group and other nearby groups of galaxies.

1. INTRODUCTION

Most of the dozen nearest groups of galaxies located within $D \sim 7$ Mpc of the Local Group (LG) are dominated by one or two spirals. The Local Group, with the two giant Sb galaxies the Milky Way and the Andromeda galaxy (M31) and about three dozen dwarf members, is a typical example of a poor group of galaxies in the local Universe. Rich groups, which include elliptical and lenticular galaxies in addition to the objects just mentioned, are much rarer. The nearest group of this type is Leo-I (M96), which is located at a distance of 10 Mpc. It includes seven bright galaxies with comparable luminosities: NGC 3351 (SBb), NGC 3368 (Sab), NGC 3377 (E5), NGC 3379 (E1), NGC 3384 (S0), NGC 3412 (S0), and NGC 3489 (S0). This group was noted as an isolated system of galaxies by Karachentsev [1], de Vaucouleurs [2], Turner and Gott [3], Materne [4], Geller and Huchra [5], and Vennik [6]. The Leo-I Group is object No. 15-1 in Tully's *Catalog of Nearby Galaxies* [7], noted as the densest part of the scattered Leo Spur cloud. According to [7], this group includes nine members and has a linear radius of 220 kpc, a radial-velocity dispersion of $\sigma_v = 112$ km/s, and a virial mass-to-luminosity ratio of $92\,M_\odot/L_\odot$.

Ferguson and Sandage [8] found about 50 new dwarf galaxies through their analysis of the central part of the Leo-I Group using large-scale images taken with the 2.5-m du Pont telescope. They pointed out that, judging from their morphologies and radial velocities, about half of these galaxies could be real members of the Leo-I Group. Recently, Flint *et al.* [9] searched for extremely faint dwarf members of the Leo-I Group in deep R-band images taken with a CCD array mounted on a 0.9-m telescope with a field of view of about one square degree. The instruments employed enabled the identification of low-surface-brightness objects in the Leo-I Group with absolute magnitudes of about -10^m, comparable to the faintest dwarf satellites of the Milky Way.

Observations of the central part of the Leo-I Group in the 21-cm neutral-hydrogen line with the Arecibo telescope enabled Schneider [10, 11] to detect several intergalactic gas clouds with radial velocities of 800–1000 km/s, values typical of the Leo-I Group. The hydrogen clouds in the group are located along a giant ellipse with a diameter of 200 kpc, which shows signs of overall Keplerian rotation. The origin of these HI clouds is evidently related to interactions (collisions) of massive members of the group, suggesting that the Leo-I Group is in a dynamically relaxed state.

1063-7729/04/4804-0267$26.00 © 2004 MAIK "Nauka/Interperiodica"

2. SEARCH FOR NEW MEMBERS ON POSS II IMAGES

Karachentsev and Karachentseva [12] used copies of the plates of the Second Palomar Observatory Sky Survey (POSS II) to search for candidate dwarf galaxies in the vicinity of known nearby galaxies. They found four low-surface-brightness dwarf galaxies in the region of Leo-I (KK 93, KK 94, KK 96, and KK 98), with angular diameters greater than $0.6'$, corresponding to linear diameters exceeding 1.8 kpc at a distance of 10 Mpc.

About half of the dwarf galaxies in the Local Group have linear diameters of 0.5–1.5 kpc, and it seemed reasonable to search for dwarf galaxies in the Leo-I Group with smaller angular diameters and fainter apparent magnitudes. We performed such a survey using copies of the blue (B) and red (R) POSS II plates in May 2003. We searched for new dwarf members of the group in the four POSS II fields 639, 640, 711, and 712, which span from $+7°$ to $+18°$ in declination and from $10^{\mathrm{h}}28^{\mathrm{m}}$ to $11^{\mathrm{h}}12^{\mathrm{m}}$ in right ascension (epoch 1950.0) and cover a total area of 120 square degrees. Thus, the area covered by our search is a factor of 16 greater than that for the survey of Ferguson and Sandage [8] and corresponds to an area 1.0×1.0 Mpc^2 in size.

We found a total of 36 likely dwarf members of the Leo-I Group, which we named "LeGxx." Table 1 gives data for these galaxies. Cross-identification of these objects with the NASA Extragalactic Database (NED) showed that only half are included in the list of Ferguson and Sandage [8] or the list of low-surface-brightness objects of Schombert *et al.* [17]. Figure 1 shows $4' \times 4'$ images of 18 new probable members of the Leo-I Group extracted from the blue POSS II Digital Sky Survey plates. For completeness, we also include in Table 1 known bright members of the group, as well as fainter galaxies with appropriate radial velocities. The columns give for each galaxy (1) its number in our list (LeG) or in the lists of Ferguson and Sandige (FS), Schombert *et al.* (D440), Karachentsev and Karachentseva (KK), or in various catalogs (NGC, UGC, CGCG); (2) the equatorial coordinates at epoch 2000.0; (3), (4) the angular size of the major axis and the axial ratio, respectively; (5) the NED apparent integrated B magnitude (we estimated B_t for new objects by comparing them with galaxies from [8] with the appropriate brightnesses); (6) the foreground Galactic absorption in the B band according to Schlegel *et al.* [18]; (7) the morphological type according to the de Vaucouleurs classification (VL and EL indicate objects with very low or extremely low surface brightnesses, respectively); (8), (9) the NED heliocentric radial velocity and the radial velocity reduced to the Local Group centroid with the apex parameters adopted from [19]; and (10) comments given at the end of the table. For five bright members of the group, column 10 gives their Cepheid-based distances from the list of Ferrarese *et al.* [20].

Figure 2 shows the sky distribution of 50 likely members of the Leo-I Group. The squares and circles show the seven brightest members and dwarf galaxies with apparent magnitudes $B_t > 13^m$, respectively; open circles and squares show E, S0, and dSph early-type galaxies; and gray circles show the positions of nine hydrogen clouds found by Schneider [10]. Table 2 gives the designations of these clouds together with their coordinates, radial velocities, and HI line widths (W_{50}). As is evident from the data in Tables 1 and 2, the position and radial velocity of hydrogen cloud V coincides (within the beam of the Arecibo telescope, $\sim 3.3'$) with those of the dwarf galaxy KK 94. The same is true for HI cloud IIe and the galaxy PGC 32327 and for cloud IV and the compact object PGC 1424345, which is probably a background galaxy.

3. PRINCIPAL CHARACTERISTICS OF THE LEO-I GROUP

Figure 3 shows the absolute-magnitude distribution of the 50 likely members of the Leo-I Group (lower histogram). The upper histogram presents a similar distribution for 80 members of the three nearest groups: the Local Group and groups located around M81 and Cen A, according to the data of Karachentsev *et al.* [21, 22]. It is evident from this figure that the two luminosity functions are similar, and both have their maximum at $M_B \sim -11^m$. This suggests that our survey of dwarf galaxies in the Leo-I Group has led to the detection of most of the population of this group.

Figure 4 presents the distribution of the relative radial velocities of the galaxies and HI clouds in Leo-I measured with respect to the radial velocity of the centroid of the Local Group. The lower, middle, and upper panels correspond to the seven brightest galaxies, 12 dwarf galaxies, and nine hydrogen clouds, respectively.

The following properties of the group can be identified based on the sky and radial-velocity distributions of its likely members.

(1) Dwarf galaxies in the vicinity of the group are scattered over a greater area than are bright galaxies. The mean projected distance from the geometric center of the Leo-I Group, which is located not far to the northeast of the pair NGC 3379/NGC 3384, is 350 kpc for the dwarf galaxies and 250 kpc for the seven bright galaxies. Here and below, we will assume that the mean distance of the group from the Earth

Table 1. List of likely Leo-I members

Object	RA, Dec (J2000.0)	a, arcmin	b/a	B_t	A_b	Type	V_h, km/s	V_{LG}, km/s	Comments (or distance)
1	2	3	4	5	6	7	8	9	10
LeG 01	103153.8+125535	0.5	0.60	18.7	0.14	Ir	–	–	
LeG 02	103319.4+101121	0.3	0.95	19.1	0.13	Ir, VL	–	–	
LeG 03	103548.8+082847	1.1	0.23	17.8	0.11	Im	–	–	
NGC 3299	103623.8+124227	2.2	0.77	13.30	0.11	Sdm	641	490	
LeG 04	103940.2+124406	0.6	0.50	18.7	0.12	Ir	–	–	
FS 01, LeG 05	103943.3+123804	0.75	0.53	16.77	0.11	dE	–	–	
P031727, LeG 06	103955.7+135428	0.6	0.65	18.3	0.15	Ir	1010	865	
UGC 5812, LeG 07	104056.6+122819	1.5	0.40	15.10	0.10	Im	1008	857	
FS 04, LeG 08	104200.3+122006	1.3	0.46	15.7	0.11	dS0	778	627	
LeG 09, FS 05?	104234.6+120902	1.2	0.83	19.1	0.11	Sph, VL	–	–	
LeG 10	104355.4+120807	0.15	0.95	19.2	0.11	Ir, VL	–	–	
NGC 3351	104357.7+114213	7.4	0.68	10.53	0.12	SBb	778	624	10.0 Mpc
LeG 11	104402.1+153520	0.5	0.90	18.8	0.14	Ir	–	–	
LeG 12	104407.8+113159	0.25	0.80	19.1	0.13	Ir	–	–	
FS 09, LeG 13	104457.6+115458	0.45	0.44	17.43	0.10	Ir	–	–	
FS 13, LeG 14	104614.4+125736	0.45	0.88	18.7	0.10	dE	886	739	(1)
KK 93, LeG 15	104624.8+140130	0.6	0.92	18.3	0.13	Ir	–	–	(2)
FS 15, LeG 16	104630.0+114521	0.4	0.98	19.0	0.11	dE, VL	–	–	
FS 17, Leg 17	104641.5+121935	0.7	0.78	16.98	0.10	Ir	–	–	
NGC 3368	104645.8+114911	7.6	0.68	10.11	0.11	Sab	897	744	10.4 Mpc
LeG 18, LeoDwa	104653.3+124440	0.8	0.75	18.9	0.10	Ir, EL	617	469	(3)
FS 20, LeG 19	104654.8+124717	0.5	0.70	18.2	0.10	Ir, VL	–	–	
KK 94, LeG 20	104657.3+125954	0.8	0.98	17.5	0.13	Ir	832	685	(4)
LeG 21	104700.8+125735	0.4	0.75	18.6	0.13	Ir	–	–	
UGC 5889	104722.3+140410	2.2	0.96	14.22	0.15	Sm	573	431	(4)
FS 23	104727.4+135323	0.4	0.75	17.79	0.15	Im	573	431	(5)
NGC 3377	104742.4+135908	5.2	0.58	11.24	0.15	E5	665	523	10.9 Mpc
NGC 3379	104749.6+123454	5.4	0.89	10.24	0.11	E1	911	762	11.1 Mpc
NGC 3384	104816.9+123745	5.5	0.45	10.85	0.12	S0	704	556	11.4 Mpc
P032327	104843.4+121856	0.2	0.95	17.51	0.11	dE	887	737	
P032348	104853.7+140728	1.2	0.50	15.5	0.17	dE	637	496	
FS 40, LeG 22	104937.1+112106	0.6	0.66	18.0	0.13	Ir, VL	–	–	
P1424345	104952.2+130942	0.08	0.90	20.?	0.15	?	754	608	(6)
LeG 23	105009.1+132901	0.3	0.95	19.1	0.14	Sph	–	–	
UGC 5944, LeG 24	105019.1+131619	1.1	0.97	14.8	0.13	dE	–	–	

Table 1. (Contd.)

1	2	3	4	5	6	7	8	9	10
KK 96, LeG 25	105027.1+122139	1.0	0.80	18.3	0.11	Sph, VL	–	–	(2)
NGC 3412	105053.3+132444	3.6	0.56	11.45	0.12	S0	841	697	
LeG 26	105121.1+125057	0.9	0.89	17.2	0.10	dEn	–	–	(7)
LeG 27	105220.1+144226	0.45	0.67	18.6	0.09	Ir	–	–	
LeG 28	105300.7+102245	0.6	0.50	18.3	0.11	Ir	–	–	
D6 40-16, LeG 29	105503.6+140536	0.3	0.83	18.6	0.10	Ir	–	–	(2)
D640-12, LeG 30	105557.1+122020	0.8	0.50	18.4	0.08	Ir	–	–	(2)
D640-13	105614.0+120037	0.7	0.57	17.66	0.08	Ir	990	841	(8)
D640-14, LeG 31	105810.5+115957	0.6	0.66	18.5	0.07	Ir	–	–	(2)
LeG 32	105917.3+150507	0.4	0.75	18.7	0.09	Ir	–	–	
NGC 3489	110018.6+135404	3.5	0.57	11.12	0.07	S0	677	538	
LeG 33	110045.2+141020	0.55	0.55	18.6	0.08	Ir	–	–	
D640-08, LeG 34	110052.1+135251	1.2	0.58	16.96	0.07	Sph	–	–	(2)
LeG 35	110302.1+080254	0.6	0.50	18.1	0.16	Ir	–	–	
CG 66-109, LeG 36	110426.5+114518	1.4	0.29	15.7	0.06	Ir	–	–	

Comments in column 10: (1) V_h taken from [9], (2) Not detected in the HI line [13], (3) V_h and B_t taken from [11], (4) V_h taken from [14], (5) HI confusion with UGC 5889, (6) V_h taken from [15], confusion with an HI cloud, (7) B_t may be erroneous in NED, (8) V_h taken from [16].

is 10.4 Mpc. The observed radial segregation of the bright and faint galaxies may indicate that the group is close to relaxation. However, the same effect could arise due to contamination by background objects among the dwarf galaxies.

(2) The Leo-I Group contains a high fraction of early-type galaxies (34%). Moreover, the early-type (E, S0, dSph) objects have a smaller mean projected distance from the center of the group (232 kpc) compared to that of spiral and irregular galaxies (414 kpc). Such morphological segregation likewise suggests the Leo-I Group is in a dynamically relaxed state.

(3) The mean radial velocity of 12 dwarf galaxies, 654±45 km/s, agrees within the errors with that of the seven brightest members of the group, 635 ± 38 km/s. However, the dwarf galaxies have an appreciably higher radial-velocity dispersion (150 km/s) than the bright galaxies (92 km/s). This difference between the kinematic behavior of the bright and faint members of the group is in good consistency with the radial segregation of galaxies according to luminosity.

(4) The subsystem of hydrogen clouds in the group is characterized by the mean radial velocity 755 ± 32 km/s and the radial-velocity dispersion $\sigma_v = 90$ km/s; i.e., the radial velocities of the HI clouds are systematically shifted relative to the radial velocity of the centroid of the group. Schneider [10] considered the hypothesis that the hydrogen clouds move in closed elliptical orbits around the galaxy pair NGC 3379/NGC 3384. In this case, Keplerian motion of the clouds with a period of four billion years yields a total mass-to-luminosity ratio of about $25\,M_\odot/L_\odot$ for this galaxy pair. Rood and Williams [23] suggested that the observed subsystem of HI clouds formed as a result of a collision between NGC 3368 and NGC 3384 only 0.5 billion years ago. It is evident that other, more complex scenarios for the origin of these intergalactic HI clouds are also possible. In particular, in the case of a triple collision between NGC 3368, NGC 3379, and NGC 3412, the mean radial velocity of the hydrogen clouds nearly coincides with that of the triplet of galaxies (Fig. 4).

We estimated the mass of the Leo-I Group using the formula of Limber and Mattews [24], which is based on the assumption that there is a virial balance of the kinetic and potential energy:

$$M_{VIR} = 3\pi N(N-1)^{-1}G^{-1}\sigma_v^2 R_H.$$

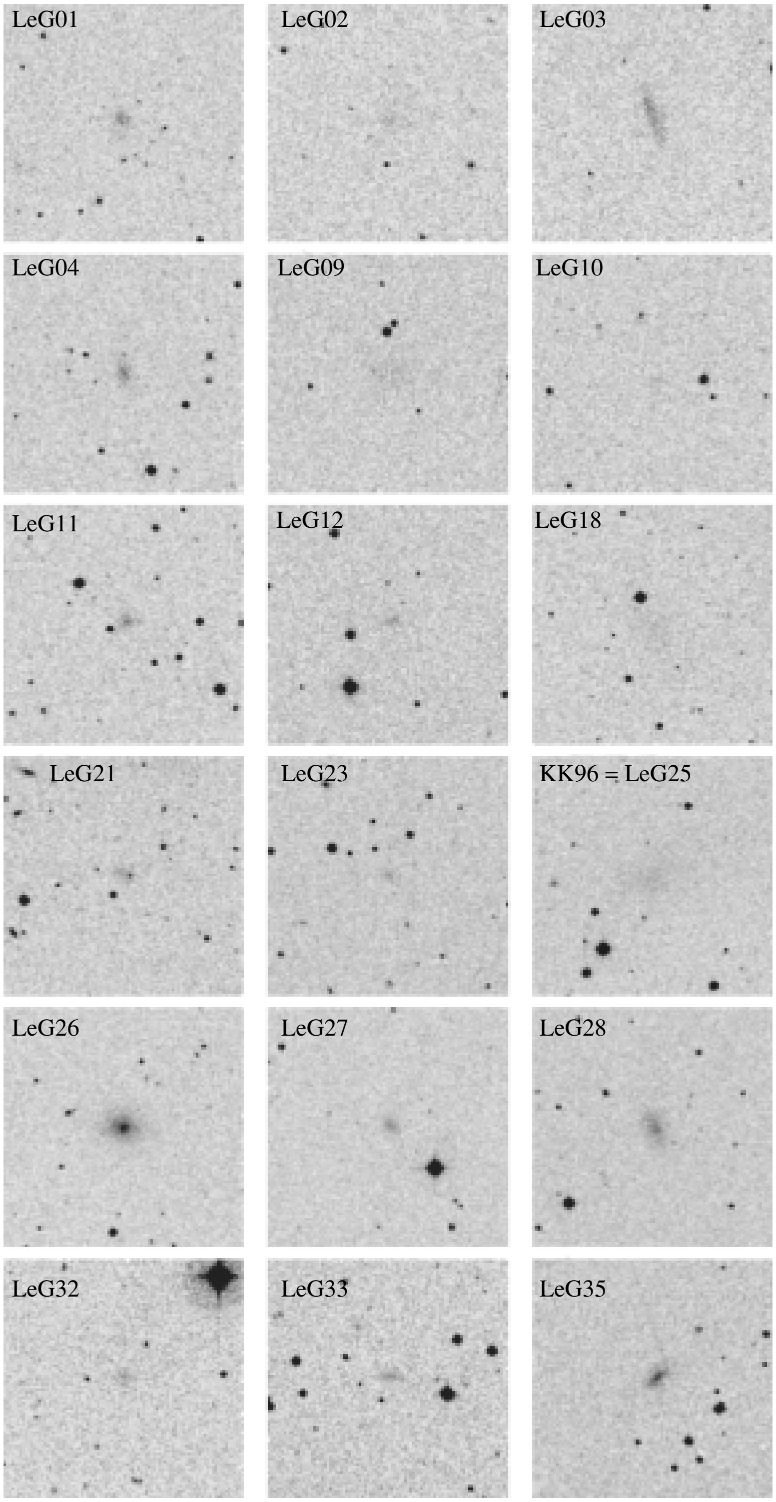

Fig. 1. Produced images of 18 new likely dwarf galaxies of the Leo-I Group from the POSS II Digital Sky Survey. Each image is $4' \times 4'$ in size.

Here, N is the number of members in the group, G is gthe gravitational constant, and R_H is the mean harmonic distance between galaxies. Treating the giant and dwarf members of the group as point masses with equal mass leads to $R_H = 191$ kpc, $\sigma_v = 130$ km/s, and $M_{VIR} = 7.2 \times 10^{12}\,M_{\odot}$. Since the total luminosity of the group is $L_B = 6.7 \times 10^{10}\,L_{\odot}$, this yields a total virial mass-to-luminosity ratio of $107\,M_{\odot}/L_{\odot}$.

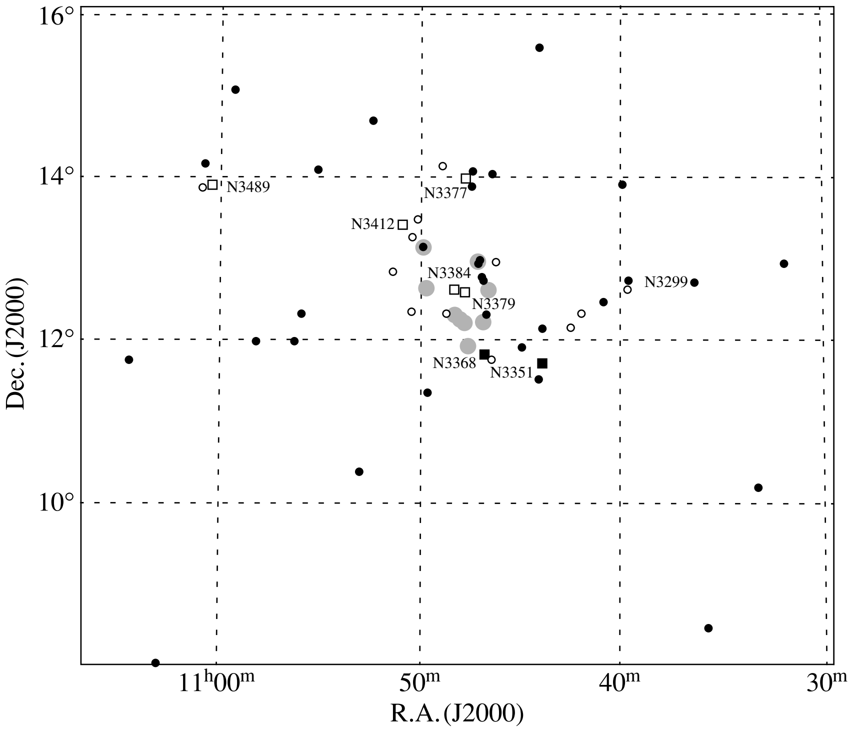

Fig. 2. Distribution of 50 likely members of the Leo-I Group in equatorial coordinates. The squares show galaxies that are brighter than 13^m; the circles, dwarf galaxies; open symbols, early-type galaxies (E, S0, dSph); and gray circles, intergalactic hydrogen clouds from [10], whose radial velocities are given in Table 2.

As noted above, the Leo-I Group shows evidence for equipartition of the kinetic energies of bright and faint galaxies. Applied to the seven brightest members of the group only, the virial relation yields $R_H = 102$ kpc, $\sigma_v = 92$ km/s, $M_{VIR} = 2.2 \times 10^{12}\, M_\odot$, and $M_{VIR}/L_B = 34\, M_\odot/L_\odot$. Thus, allowance for the range of luminosities (and masses) of the galaxies in the group decreases the estimated virial mass of the group by a factor of three. The luminosity-weighted estimate of M_{VIR}/L_B for the Leo-I Group agrees well with similar estimates for the Local Group and other nearby groups of galaxies.

Table 2. HI-clouds in the Leo-I Group

Cloud	R.A., Dec. (J2000.0)	V_h, km/s	W_{50}, km/s	V_{LG}, km/s
IV	104637+123740	970	45	821
III	104655+121405	1023	38	872
V	104707+125845	830	25	683
I	104738+115620	970	20	818
IIc	104751+121300	992	30	841
IId	104806+121620	930	30	780
IIe	104818+121840	896	30	746
VII	104943+123845	770	30	622
VI	104951+130855	760	25	614

The "crossing time," which is usually defined as $T_{cross} = \langle R \rangle / \sigma_v$, is an important parameter characterizing a group of galaxies. The crossing time for the Leo-I Group is 2.7 Gyr if derived using all 19 galaxies with measured radial velocities or 2.8 Gyr if derived using only the seven brightest members. The short T_{cross} for the Leo-I Group is consistent with the above evidence for the dynamically relaxed state of this group.

4. CONCLUDING REMARKS

The ratio of the mean velocity of the group, $\langle V_{LG} \rangle = 647 \pm 31$ km/s, to the mean distance based on the luminosities of Cepheids in five galaxies, 10.4 ± 0.3 Mpc, yields a formal Hubble constant of $H = 62 \pm 4$ km/(s Mpc) in the direction of the Leo-I Group, in good agreement with the global value of $H_0 = 71 \pm 4$ km/(s Mpc) [25]. It follows that the peculiar velocity of the Leo-I Group as a whole does not exceed $\sim$100 km/s. The angular distance between the centers of the Leo-I Group and of the Virgo cluster is only 25°, so that the small peculiar

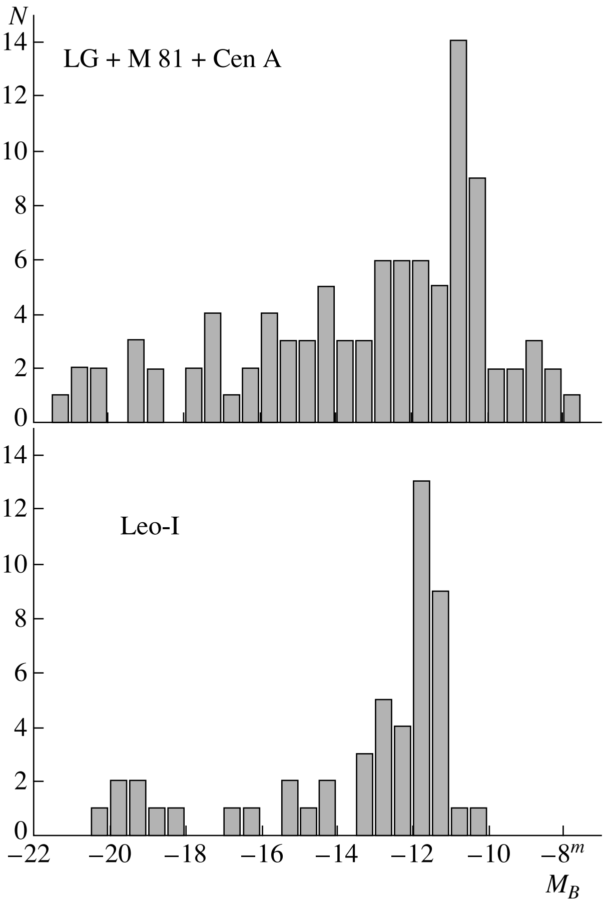

Fig. 3. The luminosity function of galaxies in the Leo-I Group (lower) and the three nearest groups: the Local Group, M81, and Cen A (upper).

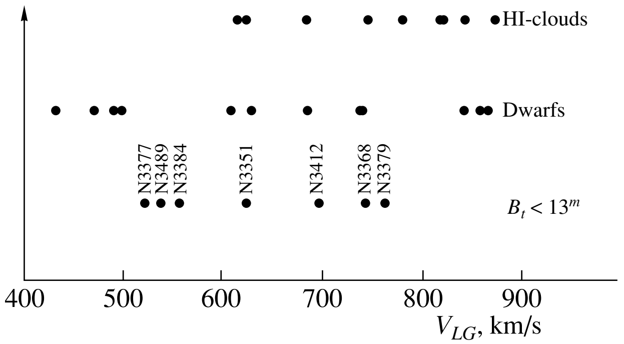

Fig. 4. Distribution of radial velocities of galaxies and HI clouds in the Leo-I Group.

velocity of the group imposes an upper limit on the total mass of the Virgo cluster.

The median crossing time for the seven nearest groups of galaxies around the Milky Way and M31 [26], IC 342 and Maffei 2 [27], M81 [21], Cen A, and M83 [22] is 2.5 Gyr. In this respect, the Leo-I Group does not stand out among other nearby groups that are dominated by one or two bright spiral galaxies. All the nearby groups noted above have rather low virial mass-to-luminosity ratios, with a median value of $\sim 30\,M_\odot/L_\odot$, implying an unusually low mean matter density in the local Universe, $\Omega_L \sim (1/7)\Omega_m$, where $\Omega_m \simeq 0.27$ is the global mean matter density [28].

According to Bahcall *et al.* [29], the M_{VIR}/L ratios for groups dominated by E and S0 galaxies are a factor of three higher than those for groups dominated by spiral galaxies. However, the case of the Leo-I Group shows that the strong discrepancy between the local and global density of matter cannot be resolved by taking into account rather rare Leo-I-type groups with moderately high virial mass-to-luminosity ratios.

Note that the Leo-I Group is very fortuitously located within the range of visibility of the Arecibo telescope. The observational capabilities of this instrument, which have been improved in recent years, open the prospect of detailed studies of the Leo-I Group via continuous "blind" surveys of the entire area of the group with the aim of finding new dwarf galaxies and hydrogen clouds.

ACKNOWLEDGMENTS

This work was partially supported by the Russian Foundation for Basic Research and the Deutschen Forschungsgemeinschaft (joint grant 02-02-04012).

REFERENCES

1. I. D. Karachentsev, Probl. Kosm. Fiz. **5**, 201 (1970).
2. G. de Vaucouleurs, in *Stars and Stellar Systems,* Ed. by A. Sandage and J. Kristian (Univ. of Chicago Press, Chicago, 1975), Vol. 9, p. 557.
3. E. L. Turner and J. R. Gott, Astrophys. J., Suppl. Ser. **32**, 409 (1976).
4. J. Materne, Astron. Astrophys. **63**, 401 (1978).
5. M. J. Geller and J. P. Huchra, Astrophys. J., Suppl. Ser. **52**, 61 (1983).
6. J. A. Vennik, Tartu Astron. Observ. Publ. **73**, 1 (1984).
7. R. B. Tully, *Nearby Galaxies Catalog* (Cambridge Univ. Press, Cambridge, 1988).
8. H. C. Ferguson and A. Sandage, Astron. J. **100**, 1 (1990).
9. K. Flint, A. J. Metevier, M. Bolte, and C. M. de Oliveira, Astrophys. J., Suppl. Ser. **134**, 53 (2001).
10. S. E. Schneider, Astrophys. J. **288**, L33 (1985).
11. S. E. Schneider, Astrophys. J. **343**, 94 (1989).
12. V. E. Karachentseva and I. D. Karachentsev, Astron. Astrophys., Suppl. Ser. **127**, 409 (1988).
13. W. K. Huchtmeier, I. D. Karachentsev, and V. E. Karachentseva, Astron. Astrophys., Suppl. Ser. **141**, 469 (2000).

14. W. K. Huchtmeier, I. D. Karachentsev, and V. E. Karachentseva, Astron. Astrophys. **401**, 483 (2003).
15. J. L. Rosenberg and S. E. Schneider, Astrophys. J., Suppl. Ser. **130**, 177 (2000).
16. J. M. Schombert, R. A. Pildis, and J. A. Eder, Astrophys. J., Suppl. Ser. **111**, 233 (1997).
17. J. M. Schombert, R. A. Pildis, and J. A. Eder, Astrophys. J., Suppl. Ser. **111**, 233 (1988).
18. D. J. Schlegel, D. P. Finkbeiner, and M. Davis, Astrophys. J. **500**, 525 (1998).
19. I. D. Karachentsev and D. I. Makarov, Astron. J. **111**, 794 (1996).
20. L. Ferrarese, H. C. Ford, J. Huchra, *et al.*, Astrophys. J., Suppl. Ser. **128**, 431 (2000).
21. I. D. Karachentsev, A. E. Dolphin, D. Geisler, *et al.*, Astron. Astrophys. **383**, 125 (2002).
22. I. D. Karachentsev, M. E. Sharina, and A. E. Dolphin, *et al.*, Astron. Astrophys. **385**, 21 (2002).
23. H. J. Rood and B. A. Williams, Astrophys. J. **288**, 535 (1985).
24. D. N. Limber and W. G. Mattews, Astrophys. J. **132**, 186 (1960).
25. D. N. Spergel, L. Verge, H. V. Peiris, *et al.*, astro-ph/0302209.
26. I. D. Karachentsev, M. E. Sharina, D. I. Makarov, *et al.*, Astron. Astrophys. **389**, 812 (2002).
27. I. D. Karachentsev, M. E. Sharina, A. E. Dolphin, and E. K. Grebel, Astron. Astrophys. **408** (2003, in press).
28. L. Verde, A. F. Heavens, W. J. Percival, *et al.*, Mon. Not. R. Astron. Soc. **335**, 432 (2002).
29. N. A. Bahcall, R. Cen, R. Dave, *et al.*, Astrophys. J. **541**, 1 (2000).

Translated by A. Dambis

Astronomy Reports, Vol. 48, No. 4, 2004, pp. 275–287. Translated from Astronomicheskiĭ Zhurnal, Vol. 81, No. 4, 2004, pp. 306–318.

Velocity Field in the Spiral-Wave Pattern Observed in Rotating Shallow-Water Experiments

A. Yu. Rylov, E. N. Snezhkin, and K. B. Titishov

Institute of Nuclear Fusion, Kurchatov Institute Russian Research Centre, pl. Akademika Kurchatova 1, Moscow, 123182 Russia

Received April 22, 2003; in final form, November 10, 2003

Abstract—The paper presents the first quantitative results of a laboratory study of the velocity field in a two-arm spiral-wave pattern generated in a steady-state fashion by a hydrodynamical instability in a differentially rotating, thin layer of liquid. The liquid layer has a free surface, and the rotational profile includes an interval where the velocity drops abruptly, as in the gaseous disks of spiral galaxies. The properties of anticyclonic vortices observed between the arms of this pattern at the corotation radius are considered. *© 2004 MAIK "Nauka/Interperiodica"*.

1. INTRODUCTION

This study represents a continuation of the laboratory investigations [1–9] aimed at modeling the hydrodynamical generation of galactic spiral structures in which there is an interval with an abrupt drop in the rotational-velocity profile. A thin layer of liquid ("shallow water") uniformly distributed over the specially profiled bottom of a rotating container served as a model of a gaseous galactic disk. The free surface and small thickness of the layer ensured the two-dimensional compressibility of the model medium (the characteristic speed of waves in the shallow water $\sqrt{gH}$ played the role of the sound speed; here, g is the gravitational acceleration and H is the thickness of the layer). The container bottom was composed of zonal pieces moving at different velocities, which created rotational profiles that are physically similar to those typical of galaxies.

The modeling results confirmed the basic conclusions of the previously developed linear theory [10–12]: the flow is unstable in an interval with an abrupt drop in the velocity with the resulting generation of a steadily rotating spiral pattern with lagging surface-density waves. The amplitude of these waves decreases in both directions with distance from the corotation circle, which passes through the instability zone. In the saturated-amplitude regime, a high degree of visual geometric similarity is achieved between the observed model pattern and its galactic counterparts. Some phenomena that may have galactic analogues were observed in these experiments, such as the branching of the arms during the rearrangement of instability modes in the case of time-dependent global rotation and the formation of anticyclonic vortices with trapped material at the corotation circle between the spiral arms. Later, the existence of galactic anticyclones predicted by Nezlin *et al.* [4] was confirmed in a series of observational studies stimulated by the modeling results and directly aimed at searches for vortical structures in the gaseous disks of spiral galaxies [13–18].

In most of these experiments, only macroscopic variables were measured quantitatively, viz., the rotation rate and the number of arms in the spiral pattern as a function of the parameters of the externally driven rotation [1–5]. The modeling results did not supply much information about the field characteristics—the distribution of the surface density and shallow-water velocity over the perturbed layer [6–9]—due to technical constraints imposed by the diagnostic instrumentation employed. However, precisely these characteristics, especially the perturbed velocity field, are of particular interest in view of the possibility of direct comparisons with astronomical observations.

The laboratory studies presented here are a first step toward filling this gap. They investigate the velocity field in a typical spiral pattern generated in a layer of shallow water with the simplest configuration of unstable rotation in which the rotational profile has a section with an abrupt drop in the velocity. A simple diagnostic technique was developed to record this field, which is based on relatively modern hardware and software and ensures satisfactory spatial and time resolutions. When analyzing the recorded velocity field, we paid particular attention to features that are of interest in the context of astrophysical applications.

Some idea of the experimental arrangement used in our study can be gained from Section 2, which presents an outline of the laboratory setup and recording instrumentation. The technique used to

1063-7729/04/4804-0275$26.00 © 2004 MAIK "Nauka/Interperiodica"

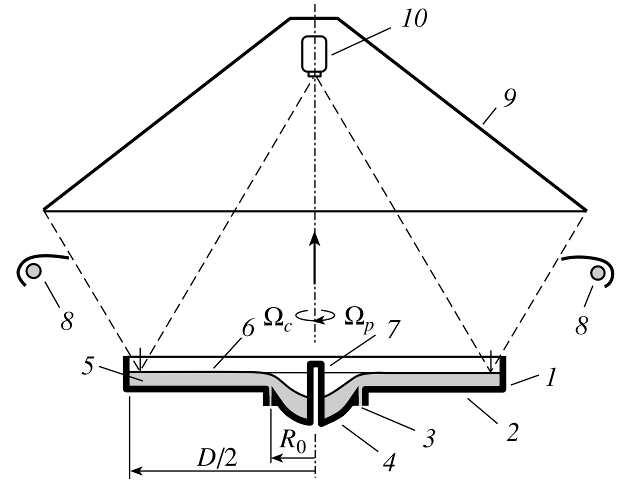

Fig. 1. Schematic of the experimental setup: (*1*) circular container, (*2*) fixed outer portion of the bottom, (*3*) annular gap between the outer and inner portions of the bottom, (*4*) rotating inner portion of the bottom, (*5*) layer of working liquid ("shallow water"), (*6*) free surface of the liquid, (*7*) central column, (*8*) fluorescent UV lamps with reflectors, (*9*) shield, (*10*) TV camera. Ω_c and Ω_p are the angular rotational velocities of the core and spiral pattern (when viewed from above, both rotate clockwise); the vertical arrow indicates the positive direction of angular velocity.

measure the velocities is described in Section 3. Section 4 presents the experimental results, their analysis, and astrophysical parallels. Some concluding remarks are given in Section 5.

2. EXPERIMENTAL SETUP AND DIAGNOSTIC INSTRUMENTATION

We carried out our experiments using a modernized form of the setup that was employed in [1–8], which is schematically depicted in Fig. 1. A thin layer of the working liquid ("shallow water" with a free surface) was distributed over the bottom of a circular container consisting of two parts—a fixed outer and a rotating inner section. The mechanical interaction of the liquid with the container bottom provided forced driving of rotation with an abrupt velocity drop in the zone between the corresponding portions of the liquid layer—the outer periphery and the inner core.

The outer portion of the bottom, which had an outer diameter of $D = 60$ cm, was flat. The surface of the inner portion was a paraboloid with a height of $z = (\Omega_0^2/2g)r^2$, where $\Omega_0 = 12.0$ rad/s and r is the radius (distance from the system axis). A cylindrical column 22 mm in diameter was mounted at the center of the paraboloid and was a structural member of the waterproof mechanical joint coupling to an electric motor beneath the container. The circular gap between the outer and central portions had a radius of $r = R_0 =$ 8 cm and a width of about 0.4 mm. The passage from one part of the bottom to another was smoothed by a common rounding of their upper edges next to the gap, which had a diameter of about 1 cm in the axial section. The surfaces of both parts of the bottom were painted mat white.

The working liquid was a water–glycerin mixture in the volume proportion 3 : 2; its density at room temperatures only slightly exceeded the density of the tracer particles (see below), which thus had minimum buoyancy. The increase in the viscosity due to the added glycerin suppressed small-scale perturbations and facilitated the generation of large-scale spiral-wave patterns (see [5, 7, 8]), including the two-arm structure analyzed here.

The structures generated in the shallow-water layer were viewed with a fixed black-and-white camera coaxial with the system and mounted 80 cm above the surface of the outer portion of the container bottom (the camera had a 753 × 582 CCD array with a sensitivity threshold and a lens stop of $f/1.2$ of 0.06 lx, CCIR with a horizontal resolution of 570 tvl). The video signal was recorded using a *Panasonic AG 7355* video tape recorder (S-VHS, PAL, horizontal resolution no less than 400 tvl, digital freeze-frame memory unit with a reduced noise level). An *Imaging Technologies ICI-PCI/AM-VS* capture board was used to digitize the video frames.

The shallow-water surface was illuminated from above by four 8-W fluorescent lamps with an emitting area of diameter 1.6 cm and length 27 cm. The lamps were equipped with reflectors and arranged axisymmetrically, along tangents to a circle of diameter 55 cm, coaxial with the system and lying in a horizontal plane 50 cm below the camera. This arrangement of the lamps (as well as the presence of a mat black shield covering the entire setup) minimized the illumination of the lens by light from the lamps that was direct, scattered, or reflected by the free surface of the liquid. The lamps were powered from the mains, with electronic ballasts (*Philips HF-M 108 TL/PLS*) used to remove the undesirable effects brightness variations during the exposure; these stabilized the voltage and increased its frequency to 30 kHz, which is well above the (standard) frame frequency of the camera.

3. DIAGNOSTIC AND DATA-PROCESSING TECHNIQUES

The velocity field in our experiments was determined by tracking the displacements of tracer particles floating on the surface of the liquid. We used images of these particles in sequences of video frames taken at a specified time interval, in nearly the same way as in the simple classic technique of recovering

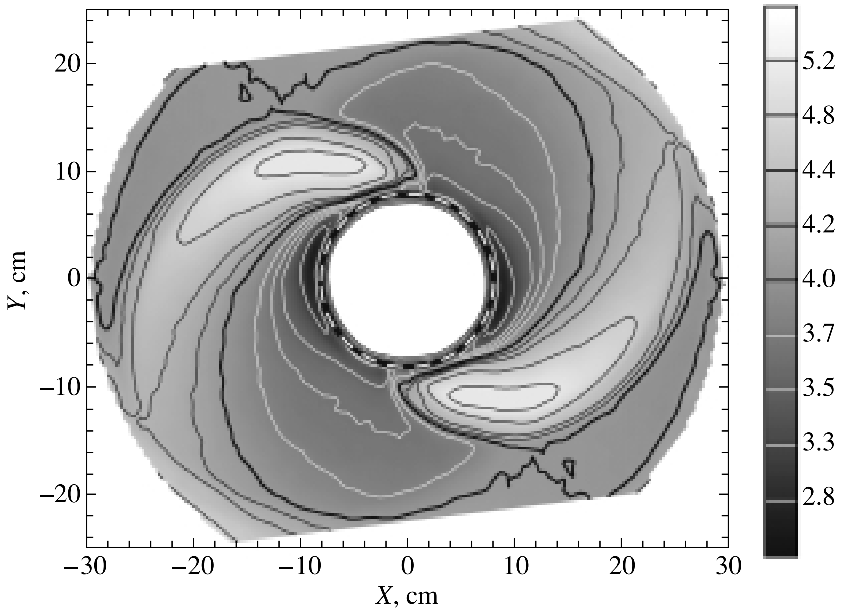

Fig. 2. Field of the perturbed thickness of the shallow-water layer with a free surface in a two-arm spiral-wave pattern obtained for $\Omega_c = -11.8$ rad/s and $\Omega_p = -2.39$ rad/s. The solid curves show thickness isolines (in mm), and the black-and-white dotted curve, the core–periphery interface. The nonmonotonic behavior of the isolines in the observed field near the upper and lower frame boundaries is due to the reflection of spiral waves from the outer walls of the container.

the velocity field from the tracks of particles in a photograph taken over a known exposure time.

To provide the necessary particle brightness and a sufficiently high signal-to-noise ratio, the working area with tracer particles fluorescent in the visible was illuminated with UV light. The particles were made of a 0.56-mm-diameter fluorescent fishing line (*Berkley Trilene XT Solar EXTSBP56-81*) cut into pieces with lengths of about 0.4 mm at right angles to its axis. The illumination was provided by *Philips Blacklight Blue TL 8W/08* lamps, which emit mainly from 320 to 380 nm, with an appreciable parasitic IR component. The illuminated tracer particles fluoresced at wavelengths of 490–560 nm, with the maximum flourescence near 510 nm. To keep the illuminative light from entering the camera due to the diffuse reflection of light from the bottom of the container into the camera, the working liquid was colored with dye (“green kiwi” B10 food coloring), which cut off fairly well both UV and IR illumination while remaining virtually fully transparent to the emission of the particles. The required image contrast was obtained without using any additional optical filters.

The pattern of the tracer-particle motions in the steadily rotating structure was surveyed using the maximum possible opening time for the electronic shutter of the camera (20 ms) in the S-VHS regime. Three consecutive frames were selected from the video recording (for a “standard” interval between frames of 40 ms), digitized with a resolution of 768 × 572 pixels and 256 gray-scale levels, and then used to derive particle-velocity vectors according to the following algorithm. For each particle, we (1) measured the polar coordinates of its image in all three frames; (2) determined the radial component of the velocity vector from the difference between the radial coordinates in the first and last frames; (3) determined the azimuthal velocity component from the difference between the azimuthal coordinates in the first and last frames multiplied by the radial coordinate in the middle frame; and (4) assigned the tail of the vector to the position of the particle in the middle frame. We took advantage of the symmetry of the arms to substantially improve the diagnostic resolution: after rotating the pattern of the vectors by 180°, both the original and rotated pattern were combined, doubling the number of tracer particles. The frame capture was controlled and the images digitally processed using a *Media Cybernetics Optimas 6.51* image processor.

The obtained distributions of the azimuthal and radial velocities of the tracer particles were translated into Cartesian coordinates and a linear-triangulation technique was used to interpolate them to a rectangular grid with steps of 0.5 cm in both coordinates, under the formal assumption that the azimuthal (linear) velocity vanishes at the center of the core ($r = 0$) and the radial velocity vanishes at the wall of the column ($r = 1.1$ cm). The triangulation results were smoothed by averaging over cells 5×5 gridpoints

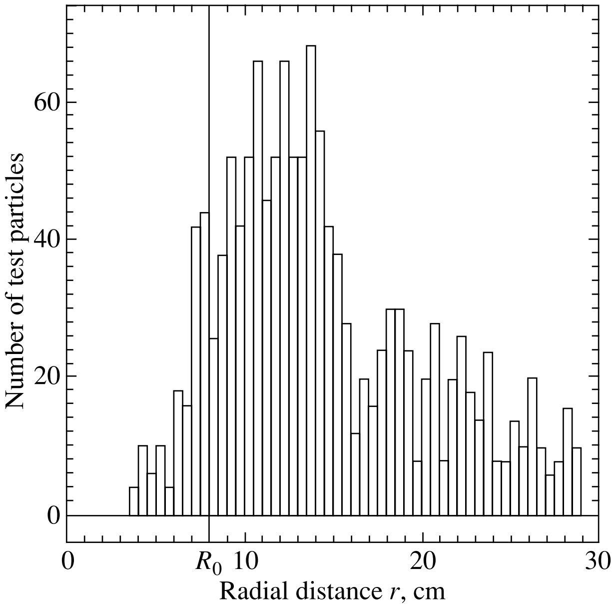

Fig. 3. Histogram of the radial distribution of the tracer particles.

in size, doubling the weight of the gridpoints at the cell centers. We assumed that the smoothed matrices represented the azimuthal and radial velocity fields of the shallow-water layer, $V_\varphi(x,y)$ and $V_r(x,y)$, respectively, in the laboratory frame. All other field characteristics of the flows presented below were directly calculated from these two matrices.

The spatial resolution of the entire video–digital system was limited by the capabilities of the video tape recorder. Our framing (with the image of the circle bounding the liquid layer inscribed between the short sides of the video frame) ensured a resolution of about 1 mm throughout the working area. In practice, the system could reliably resolve test-particle displacements about as small as the particle size; in terms of the minimum measurable speed, this corresponded to about 0.7 cm/s for an 80-ms interval between the utilized frames.

4. RESULTS AND DISCUSSION

4.1. General Questions and the Layer-Thickness Field

We chose the two-arm pattern steadily generated in the liquid layer due to the clockwise rotation of the inner portion of the bottom at a constant rate of $\Omega_c = -11.0$ rad/s to obtain the velocity field. This basic pattern consists of two lagging spiral waves on the liquid surface that form a single pattern rotating in the same direction at a rate of $\Omega_p = -2.72$ rad/s. An idea of the appearance of this pattern can be gained from Fig. 2, which shows the field of the perturbed layer thickness in a close "auxiliary" pattern generated under similar experimental conditions. We employed a diagnostic technique that enabled recording of the thickness field only at the periphery,[1] but the wave arms observed there are continued in the core, and their ridge lines intersect the circle $r = R_0$ smoothly, without a discontinuity or change in the twist angle (see the photographs taken in the previous experiments [5, 7, 8]). In the figure, the field of thickness has been turned "manually" to achieve phase coincidence with the fields of the kinematic parameters of the basic pattern in the zone next to the core–periphery interface (the accuracy of the coincidence is limited by the angle through which the pattern rotates within the standard time interval between video frames, which is about 6° at the observed rotation rate). The auxiliary pattern was generated in a somewhat thicker liquid layer, which gave rise to a small difference in the angles of the spiral twist [9, 20] and to a small azimuthal displacement between the fields of the two patterns away from the core.

We should comment here on the unperturbed layer thickness as a parameter that determines the analogue of the sound speed in a medium and, along with Ω_c, specifies the physical regime of the phenomenon studied. In theoretical and numerical analyses of the development of shallow-water instabilities in a given configuration, this parameter is normally regarded as an independent characteristic of the liquid layer in its initial state, with an already specified unstable rotation and the corresponding equilibrium profile of the free surface but without any perturbations. In contrast, such a state can never be realized in a laboratory experiment, where only the entrainment of the liquid into the rotation rather than the rotation itself is specified. As soon as the inner portion of the bottom starts rotating beneath the motionless layer of liquid, the following parallel and interrelated processes begin: (i) the gradual driving of the rotation (due to the frictional interaction with the bottom), (ii) the redistribution of the liquid between the core and periphery (a "globally equilibrated profile" of the free surface corresponding to the current rotation curve is established), and (iii) increases in the amplitudes of the inevitably present perturbations (these are primarily short-wave perturbations, which are predominant in terms of their growth rate at early stages of the instability development; the self-attraction of the system in short-wave modes is so efficient that the lowest modes, including the second mode considered

---

[1] The field of thickness was obtained via optical densitometry using light diffusely reflected by the bottom when the working area was illuminated by the fluorescent daylight lamps ; a detailed consideration of this technique, which was similar to those employed in [9, 19], and the physical results of thickness measurements is beyond the scope of this paper.

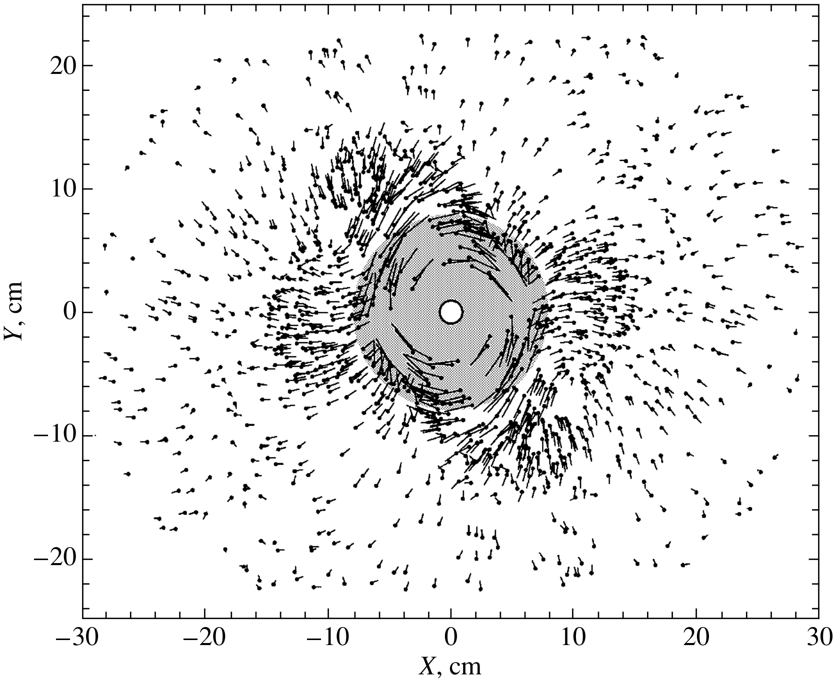

Fig. 4. Pattern of motion of the tracer particles floating on the surface of the shallow water. The dots show the positions of the tracer particles; the rectilinear segments issuing from the dots in the direction of motion, the velocity vectors of the particles in the laboratory frame; and the gray circle, the core of the liquid layer.

here, are essentially excited only due to transitions from previously generated higher modes which reach their peak amplitudes and then decay as the jump in the rotational velocity grows). In this situation, the closest physical analogue for the unperturbed thickness of the working layer, which is introduced *a priori* in theoretical and numerical models, is a quantity that can only be obtained *a posteriori* by averaging the perturbed thickness that is actually observed in regimes with well developed nonlinear structures. Under the conditions of Fig. 2, the layer thickness averaged over the entire peripheral region is about 4.0 mm (the corresponding speed of waves in the shallow water—the "sound speed"—is about 20 cm/s), which, as a number of indirect indications suggest, is 10–20% higher than for the basic pattern.

4.2. Velocity Fields and the Rotation Curve

The fields of kinematic variables in the basic structure were recovered from the azimuthal and radial velocities of the tracer particles at 1372 points, whose radial distribution is illustrated by the histogram in Fig. 3. The motions of the particles themselves based on these velocities are shown in Fig. 4; to better resolve small velocities, the dynamic range of relative variations in the lengths of the vectors is artificially shrunken, as it is in Fig. 7 below (so that the length is proportional to the square root of the velocity modulus). The recovered radial and azimuthal velocity fields in the laboratory frame are shown in Fig. 5.

In a steady-state regime, an azimuthally symmetric mechanism externally driving the rotation cannot directly introduce radial motions in the system; therefore, the entire observed radial-velocity field is made up of perturbations directly related to the self-organizing structure. The distribution of this field relative to the perturbed-thickness field should be particularly noted. In the spiral arms themselves, where the surface density is increased, the liquid moves away from the center, whereas it moves toward the center in the wider region between the arms, where the density is reduced (cf. Figs. 2 and 5a). As they run on the medium, the lagging arms being hydrodynamical waves of compression, i.e., potential humps, push the liquid away from the center, so that the sign of the radial velocity changes from minus to plus on the outer edge of the arms, where the leading front of the wave–medium interaction is located.[2] This feature of the correlated dispositions of the fields, which characterizes spiral structures of the type considered, can be used to identify such structures in galaxies. This is

---

[2] This correlation refers to the periphery only. The situation is the opposite in the core: the liquid moves toward the center in the arms and away from the center between the arms, with the leading fronts being at the inner edges of the arms.

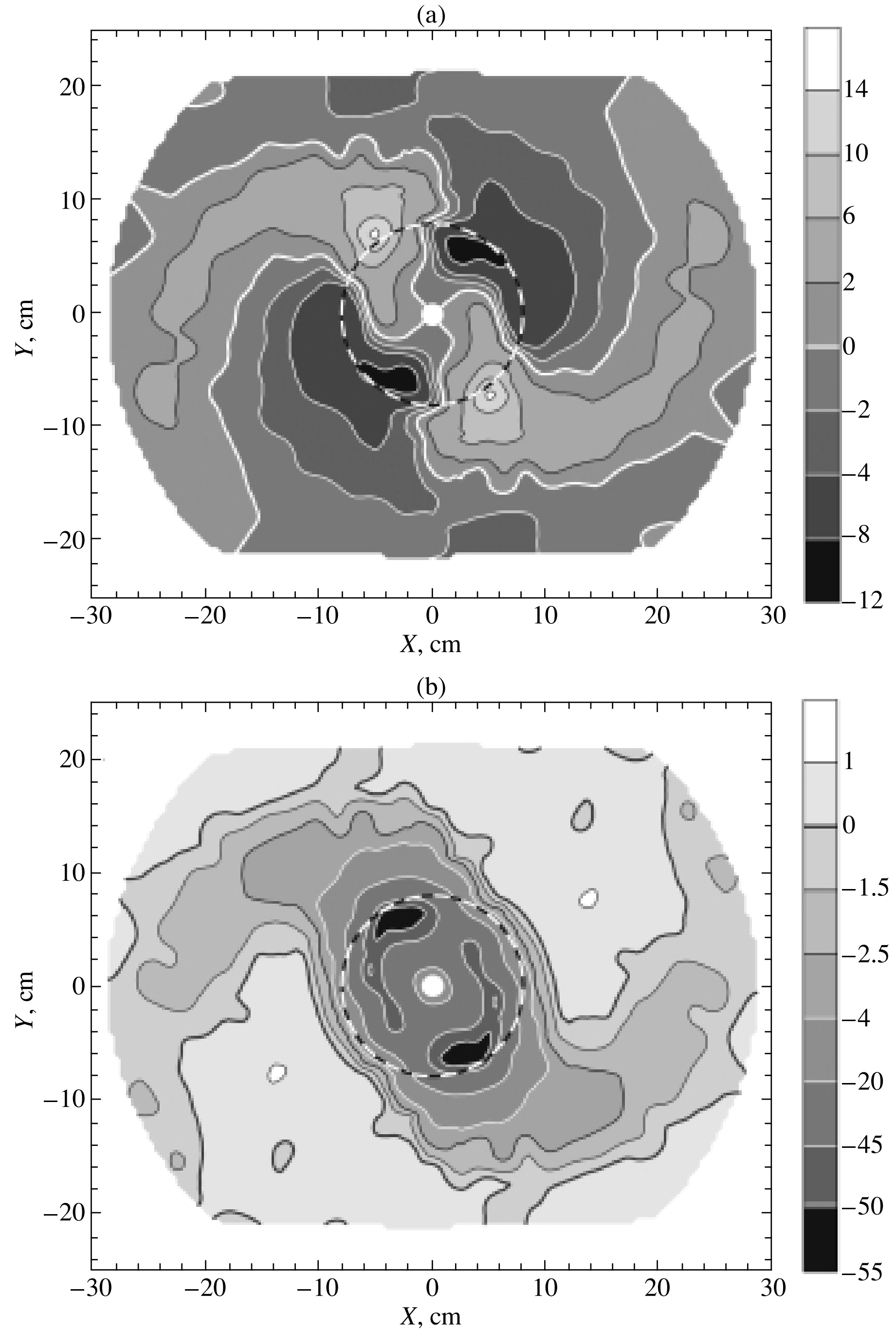

Fig. 5. Fields of the polar components of the velocity of the shallow water in the laboratory frame. The solid curves show isolines of the (a) radial velocity V_r and (b) azimuthal velocity V_φ in cm/s, and the dotted curve, the core–periphery interface.

facilitated by the fact that the field of the radial velocity (the velocity directed along the galactic radius) can be directly derived from observations: it is the field of spatial variations in the line-of-sight velocity in the vicinity of the minor axis of the galaxy (Nezlin and Snezhkin [6] proposed to identify hydrodynamical galactic spirals based on a geometric correlation between the observed pattern and the contours of the line-of-sight velocity in the vicinity of the minor axis).

The azimuthal-velocity field (Fig. 5b) can naturally be regarded as a superposition of the disturbance introduced by the generated structure and some azimuthally symmetric rotation that is directly driven from outside the system. This rotation can be determined simply by averaging the observed field over the azimuthal coordinate, to obtain an analogue of the galactic rotation curve. The result of such averaging over annular zones of width $\Delta r = 0.5$ cm is shown in Fig. 6a. A comparison of the resulting curve $\bar{V}_\varphi = \bar{V}_\varphi(r)$ with the straight line shown in the same plot, which corresponds to rigid rotation of the spiral pattern, shows that corotation occurs exactly at the core–periphery interface ($r = R_0$) at a velocity of $\Omega_p R_0 = -21.8$ cm/s, which exceeds the characteristic speed of waves in the shallow water by 10–20% in magnitude (note that the full range of the test-particle azimuthal velocities and unaveraged velocity V_φ comprises up to three times the “sound speed,” and, as can be seen from Figs. 5b and 6a, motions counter to the driven rotation are observed over a large portion of the periphery, between the arms).

It is noteworthy that the curve $\bar{V}_\varphi(r)$ is much flatter in the corotation region than it would be if the azimuthally symmetric differential rotation of the liquid remained stable under the same external-driving conditions. In the latter case, the transition from the rigidly rotating core to the motionless periphery would involve a velocity drop of more than quadruple the “sound speed” ($\Omega_c R_0 = -88$ cm/s) over a length scale that is close to the layer thickness. However, in a real regime with a well developed instability and a mature spiral pattern, a velocity drop that is almost half this value (the peak value of $\bar{V}_\varphi$ is about 47 cm/s) takes place on a much larger scale (at $r = R_0$, the corresponding characteristic length scale is $|\bar{V}_\varphi/(\partial\bar{V}_\varphi/\partial r)| \approx 2.2$ cm). If this comparison is made, the falling slope of the curve $\bar{V}_\varphi(r)$ appears highly smoothed; nevertheless, in absolute terms—from the standpoint of hydrodynamical stability or instability of a hypothetical azimuthally symmetric rotation with such a profile—the behavior of this curve near the corotation circle corresponds to a very strong radial dependence: $\bar{V}_\varphi(r) \propto r^{-3.7}$. Note that a similar situation arises when the realizability of a hydrodynamical mechanism for the generation of spiral patterns is considered for actual galaxies [13]. On the one hand, as can be judged from the large amplitude of the observed galactic spiral waves, the instability that generates them has proceeded in its development far from the initial stage, so that the current local nonuniformity of the rotation of the gaseous galactic disk—the immediate source of instability—should definitely be much weaker than it was initially. On the other hand, the velocity jump in observed galactic rotation curves is so sharp that azimuthally symmetric rotation of a gaseous disk with such a profile would be unstable.

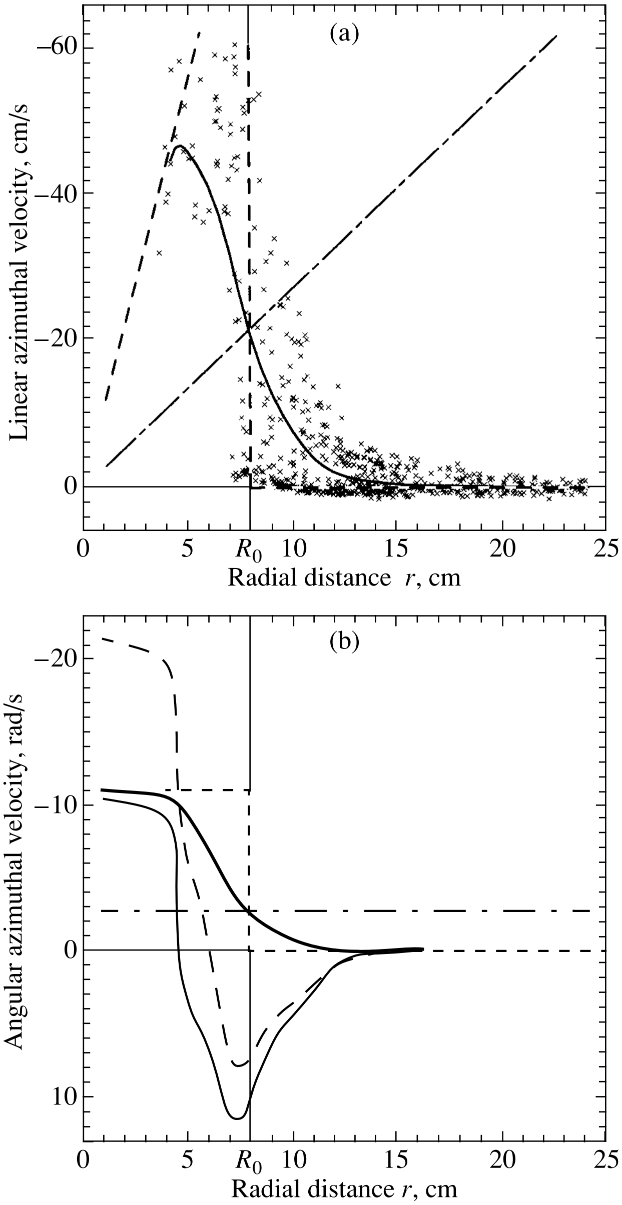

Fig. 6. (a) Characteristics of shallow-water rotation in terms of the linear velocity. The solid curve shows the azimuthal velocity given in Fig. 5b after averaging over the angular coordinate, $\bar{V}_\varphi$ (the observed rotation curve), and the crosses, experimentally measured azimuthal velocities of tracer particles. (b) Same as (a) in terms of angular velocity. The thick solid curve shows the averaged azimuthal angular velocity $\bar{V}_\varphi/r$; the thin solid curve, the radial derivative of the averaged linear azimuthal velocity $\partial\bar{V}_\varphi/\partial r$; and the dashed curve, the sum of the first two quantities, $\bar{V}_\varphi/r + \partial\bar{V}_\varphi/\partial r$ (this coincides with the absolute vorticity averaged over the angular coordinate). In both plots, the dotted curve shows the motion of the bottom of the container, and the dash–dot curve, rigid rotation at the velocity of the pattern.

Further details characterizing the smoothing of the original jump can be seen if the shallow-water rotation curve is represented in terms of the angular velocity (Fig. 6b). In the averaged profile of the az-

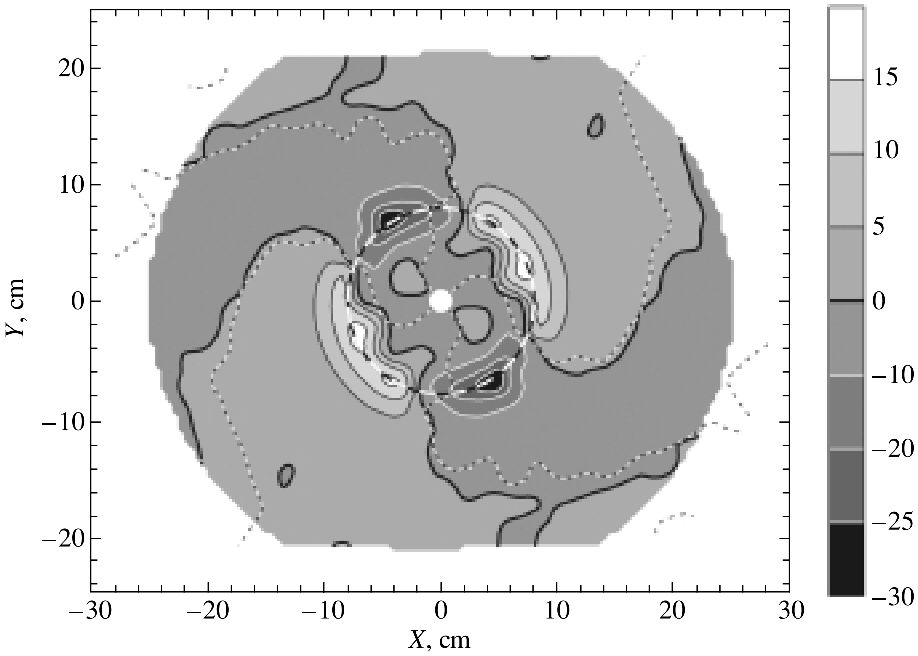

Fig. 7. Field of perturbations of the azimuthal velocity of the shallow water determined as the difference between the azimuthal velocity in the laboratory frame and averaged over the azimuthal angle. The solid curves show isolines of this residual azimuthal velocity ($V_\varphi - \bar{V}_\varphi$) in cm/s; the thin dotted curves, the isolines of zero radial velocity; and the thick dotted curve, the core–periphery interface.

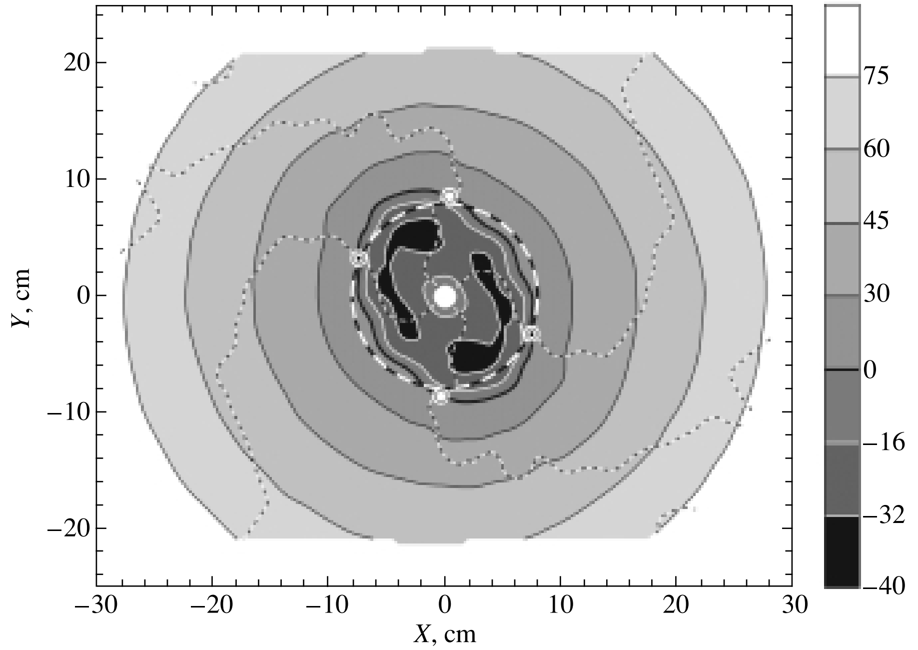

Fig. 8. Field of the azimuthal velocity of the shallow water in a frame corotating with the pattern. The solid curves show isolines of this velocity ($V_\varphi - \Omega_p r$) in cm/s; the thin dotted curves, the isolines of zero radial velocity; the thick dotted curve, the core–periphery interface; the circled dots, centers; and the hollow circles, saddles.

imuthal angular velocity $\bar{V}_\varphi/r$, a smooth decline in the absolute magnitude of this velocity can be observed within an interval whose width is comparable to the core radius R_0 in place of the sharp, "driven" jump several millimeters wide. This decline is nevertheless steep enough that the (azimuthally averaged) vorticity between the region of almost-rigid core rotation and the nearly motionless outer part of the periphery have signs opposite to the externally driven main rotation (such substructure is typical of so-called

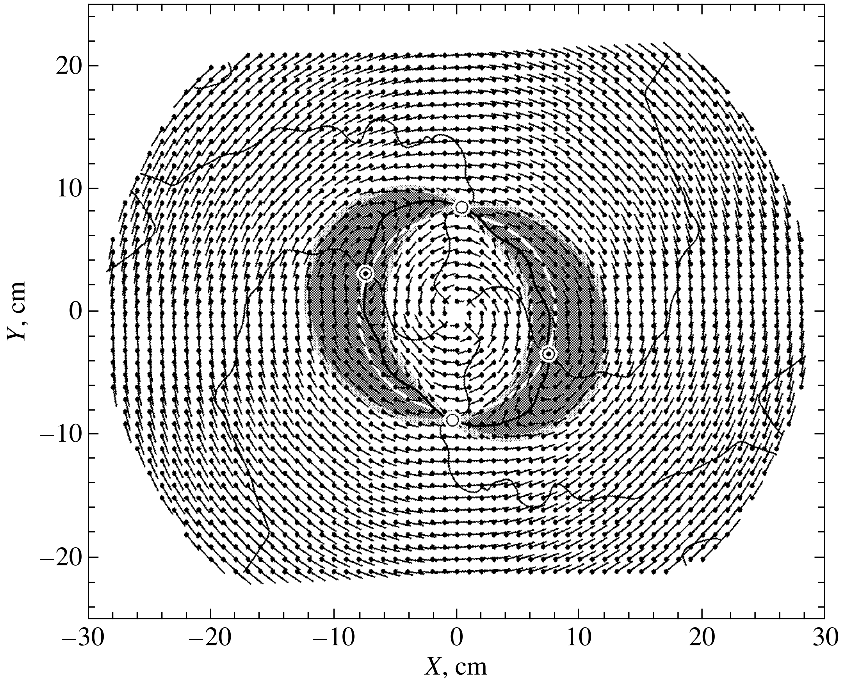

Fig. 9. Field of the total velocity of the shallow water in a frame corotating with the pattern. The rectilinear segments issuing from the interpolation gridpoints (marked with dots) in the direction of motion show the velocity vectors; the thick curve, the isoline of zero azimuthal velocity in this frame; the thin curves, the isolines of zero radial velocity; the white circle, the core–periphery interface; the gray areas, the approximate locations of regions where the liquid is trapped by vortices; the circled dots, centers; and the hollow circles, saddles.

isolated vortices [21]). The width of the annular zone with an anticyclonic velocity shear is likewise close to R_0.

Figure 7 shows the azimuthally asymmetric component of the azimuthal velocity, which is, in the above sense, a perturbation produced by the generated structure and is defined as the difference $V_\varphi - \bar{V}_\varphi$ (the residual azimuthal velocity). The pattern of the correlation between this field and the density and radial-velocity fields (cf. Fig. 7 to Figs. 2 and 5a) is quite expected. The observed spiral waves are lagging, i.e., curved backward. As they run on the liquid outside the corotation circle, their leading fronts push the liquid not only away from the center, but also in the direction of rotation of the pattern, so that the perturbation of the azimuthal velocity just behind the fronts in the arms, where the liquid moves outward, coincides in sign with Ω_p. Within the corotation circle, where the liquid moves in the arms inward, the sign of the perturbation of the azimuthal velocity is opposite to the sign of Ω_p (see also Footnote 2).

4.3. Vortical Structure

Figure 8 depicts the field of $V_\varphi - \Omega_p r$, i.e., the field of the azimuthal velocity in a frame that rotates together with the pattern, in which the liquid motions are, accordingly, stationary. We can see that the liquid is motionless at four points in this pattern, where the isoline of zero azimuthal velocity $V_\varphi - \Omega_p r$ is intersected by the isolines of zero radial velocity (shown in the same graph). These points are among the elements characterizing the vortical structure that can be identified in the vector field of the total velocity represented in the same rotating frame (Fig. 9).

The structure consists of two vortices occupying banana-like regions between the spiral arms. Based on the topology of the field and the assumption of purely two-dimensional motion, these regions can be considered regions of trapped liquid. They are located along the jump line $r = R_0$ and abut on each other at their ends, forming a closed annular figure. The maximum width of these regions (their radial size) reaches 6–7 cm. Two of the four points noted above are essentially on the jump line, at the corotation circle, and the liquid around them circulates within vortices (in view of this, we call these points centers, although, according to their topological properties and for the corresponding three-dimensional motion, they may be more similar to foci). The two other points are shifted somewhat toward the periphery and are saddles common to the boundaries (separatrices) of the abutting regions. The centers in the vortices are shifted in the direction of the overall rotation, so that the considered regions turn out to be az-

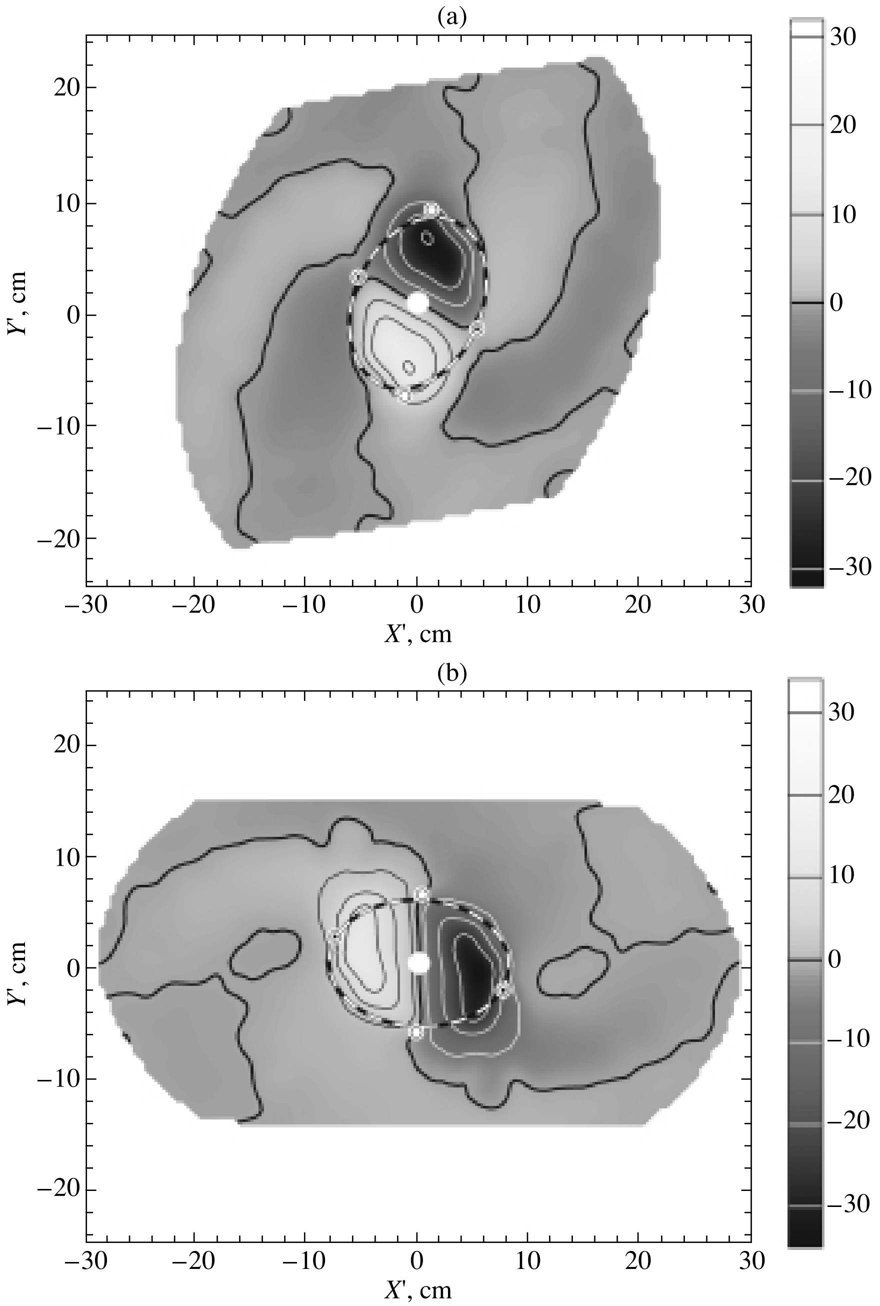

Fig. 10. Field of the line-of-sight component of the velocity of the shallow water (in cm/s) in the laboratory frame for a fixed inclination of the line of sight to the surface of the motionless liquid layer and various positioning of this inclination in the pattern of the spiral vortical structure. The intersection of the layer surface with the plane containing the line of sight and the rotational axis of the system passes (a) through the centers (circled dots) inside the vortices, (b) through the saddles (hollow circles) between vortices, and along the bisectrices of the angles between the first two directions in the (c) front and (d) rear parts of the regions of trapped liquid. The dotted line shows the core–periphery interface, the coordinates X' and Y' measure distances in the plane normal to the line of sight, and the angle between the line of sight and the positive angular-velocity axis is 135°.

imuthally asymmetric: their front, through which the spiral arms pass, are shorter than their rear parts.

The vortices can be considered anticyclones in the sense that the liquid within them circulates counter to the overall rotation of the system. Accordingly, a ridge of anticyclonic (positive) values of the absolute vorticity (i.e., the vorticity calculated from the full velocity in the laboratory frame) runs through these vortices (along their longitudinal axes), forming a closed oval strip. The peaks of this ridge are at the

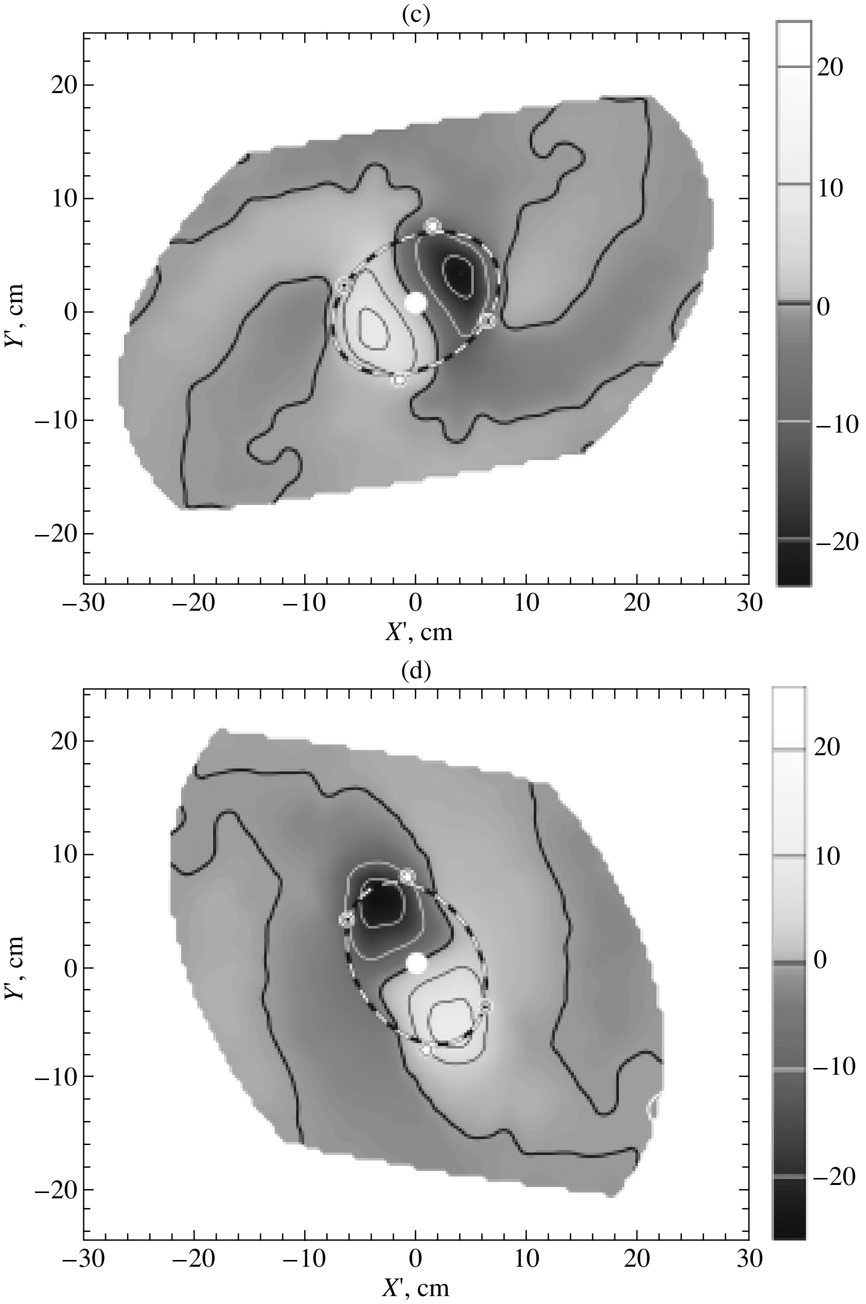

Fig. 10. (Contd.)

centers in the anticyclones (the maximum vorticy in the layer is about 11 s^{-1}), and the lowest points are near the saddles (where the absolute vorticity is about 5 s^{-1}). A more detailed analysis shows that the azimuthal velocity in this zone only partially determines the absolute vorticity, maintaining no more than its anticyclonic "background," which varies very little along the ridge. The vorticity variations along the ridge are mainly due to spatial variations in the radial velocity: the sharp changes in the direction of the vorticity near the centers and saddles form anticyclonic (positive) and cyclonic (negative) local additions to the background vorticity, respectively.

The smallness of $|2\Omega_p|$ compared to the absolute vorticity means that the "global" rotation of the frame in which the anticyclones are at rest is slower than the local rotation of the liquid within the anticyclones. In this situation, the Coriolis force only weakly affects the dynamics of the anticyclones, and thus the thickness of the liquid layer, which is proportional to the pressure, decreases toward the centers of these anticyclones; this contrasts with the case of slowly rotating, "traditional" anticyclones, such as the large-scale geostrophic vortices that are widely studied in geophysics and the anticyclonic vortical Rossby solitons (with layer thickness increasing toward their centers) that are investigated in model experiments [7, 8, 19].

To conclude this subsection, we note that the vortical structure studied, which consists of two anticyclones, and the central cyclone, which occupies most of the core, can, in principle, be regarded as a unified vortical system. Such systems are sometimes called tripolar vortices (see, e.g., [22]). If we use this term in the case of our two-arm spiral-wave structure, then, according to the same algorithm, a three-arm structure with three anticyclones between arms should be regarded as a unified quadrupole, a four-arm structure with four anticyclones as a pentapole, and so on, proceeding to more and more exotic "multipoles" (structures with up to ten arms were observed in the experiments [1–9]). This terminology seems artificial to say the least. In view of the astrophysical orientation of our laboratory modeling, the relationship between the chain of anticyclones and the spiral density-wave pattern seems more important. They constitute a unified spiral vortical structure, and precisely their mutual agreement and, most importantly, their strictly defined spatial correlation within this structure provide a basis for identifying the presence of the modeled phenomenon in real galaxies.

4.4. The Field of the Line-of-sight Velocity

In this subsection, we present the experimental results of our velocity measurements in such a way as to model additionally the following "nonphysical" objective fact, which plays a considerable role in astronomical observations. In reality, galactic disks are inclined at some angle to the line of sight, and only the line-of-sight velocity can be directly measured. The figures presented below demonstrate the spiral vortical structure studied in an "astronomical format," as a line-of-sight velocity field in a layer of shallow water viewed at some angle, and the dependence of this field on the angle of the line of sight relative to the pattern. In Fig. 10, the rotational axis projected onto the plane normal to the line of sight coincides with the minor axis of the image and passes through the centers (Fig. 10a), saddles (Fig. 10b), and in two intermediate directions (Figs. 10c, 10d).

Obviously, if we needed to determine the position and parameters of the vortices in the structure based solely on a line-of-sight velocity field similar to the fields in Fig. 10, which differ widely from one another, this would be a challenging task. It would be no simpler to resolve the general problem of recovering the original total-velocity field. For galaxies, where the situation is also strongly complicated by numerous objective factors (first of all by the irregularity of the structures), we must develop specialized techniques for processing the observational data in order to recover the total-velocity field with the vortical perturbations adequately resolved (see [14–18] devoted to the development and very fruitful employment of such techniques). In view of this, the experimental arrangement considered here could provide not only a model for studies of hydrodynamical phenomena in the gaseous disks of some types of galaxies but also a "laboratory test bench" by means of which astronomical methods for recovering the distribution of the local velocity in such disks can be verified on a real physical system that is much more accessible and controllable than its astrophysical analogues.

5. CONCLUSIONS

We have studied here only one of the two basic field characteristics of the spiral vortical structure considered. We plan to investigate the other—the perturbed surface density—in a future study. A combined quantitative analysis of the two fields corresponding to the same experimental conditions could make it possible to obtain detailed information on their relative distributions within the structure (which is important for astrophysical applications) and to elucidate the origin of some features that are important in experimental shallow-water hydrodynamics, such as the role of local vertical flows, which are difficult to measure directly in a thin liquid layer.

ACKNOWLEDGMENTS

We are grateful to G.P. Chernikov for useful discussions. This work was supported by the Ministry of Industry, Science, and Technologies of the Russian Federation under State Contracts nos. 108-38(00)-P and 40.020.1.1.1167.

REFERENCES

1. A. G. Morozov, M. V. Nezlin, E. N. Snezhkin, and A. M. Fridman, Pis'ma Zh. Éksp. Teor. Fiz. **39**, 504 (1984) [JETP Lett. **39**, 613 (1984)].
2. A. M. Fridman, A. G. Morozov, M. V. Nezlin, and E. N. Snezhkin, Phys. Lett. A **109A**, 228 (1985).
3. A. G. Morozov, M. V. Nezlin, E. N. Snezhkin, and A. M. Fridman, Usp. Fiz. Nauk **145**, 160 (1985) [Sov. Phys. Usp. **28**, 101 (1985)].
4. M. V. Nezlin, V. L. Polyachenko, E. N. Snezhkin, *et al.,* Pis'ma Astron. Zh. **12**, 504 (1986) [Sov. Astron. Lett. **12**, 213 (1986)].
5. M. V. Nezlin, A. Yu. Rylov, E. N. Snezhkin, and A. S. Trubnikov, Zh. Éksp. Teor. Fiz. **92**, 3 (1987) [Sov. Phys. JETP **65**, 1 (1987)].

6. M. V. Nezlin and E. N. Snezhkin, *Rossby Vortices and Spiral Structures* (Nauka, Moscow, 1990), p. 237 [in Russian].
7. M. V. Nezlin and E. N. Snezhkin, *Rossby Vortices and Spiral Structures (Astrophysics and Plasma Physics in Shallow Water Experiments)* (Nauka, Moscow, 1990).
8. M. V. Nezlin and E. N. Snezhkin, *Rossby Vortices, Spiral Structures, Solitons. Astrophysics and Plasma Physics in Shallow Water Experiments* (Springer-Verlag, Berlin, Heidelberg, New York, 1993).
9. E. N. Snezhkin and J. Sommeria, *Generation of Vortex Patterns and Spiral Waves in a Shallow Water Annular Shear,* Ann. Geophys. **16** (4), 1136 (1998).
10. A. G. Morozov, Pis'ma Astron. Zh. **3**, 195 (1977) [Sov. Astron. Lett. **3**, 103 (1977)].
11. A. M. Fridman, Usp. Fiz. Nauk **125**, 352 (1978) [Sov. Phys. Usp. **21**, 536 (1978)].
12. A. G. Morozov, Astron. Zh. **56**, 498 (1979).
13. V. L. Afanas'ev and A. M. Fridman, Pis'ma Astron. Zh. **19**, 784 (1993) [Astron. Lett. **19**, 319 (1993)].
14. A. M. Fridman, O. V. Khoruzhii, E. V. Polyachenko, *et al.,* Phys. Lett. A **264**, 85 (1999).
15. A. M. Fridman, O. V. Khoruzhii, V. V. Lyakhovich, *et al.,* Astron. Astrophys. **371**, 538 (2001).
16. A. M. Fridman, O. V. Khoruzhii, E. V. Polyachenko, *et al.,* Mon. Not. R. Astron. Soc. **323**, 651 (2001).
17. V. V. Lyakhovich, A. M. Fridman, O. V. Khoruzhii, and A. I. Pavlov, Astron. Zh. **74**, 509 (1997) [Astron. Rep. **41**, 447 (1997)].
18. A. M. Fridman, O. V. Khoruzhii, V. V. Lyakhovich, *et al.,* Astrophys. Space Sci. **252**, 115 (1997).
19. S. M. Antipov, M. V. Nezlin, E. N. Snezhkin, and A. S. Trubnikov, Zh. Éksp. Teor. Fiz. **82**, 145 (1982) [Sov. Phys. JETP **55**, 85 (1982)].
20. S. V. Alekseenko and A. A. Cherep, Dokl. Akad. Nauk **327**, 306 (1992) [Sov. Phys. Dokl. **37**, 537 (1992)].
21. E. J. Hopfinger and G. J. F. van Heist, Ann. Rev. Fluid Mech. **25**, 241 (1993).
22. G. J. F. van Heijst, R. C. Kloosterziel, and C. W. M. Williams, J. Fluid Mech. **225**, 301 (1991).

Translated by A. Getling

Astronomy Reports, Vol. 48, No. 4, 2004, pp. 288–300. Translated from Astronomicheskiĭ Zhurnal, Vol. 81, No. 4, 2004, pp. 319–332.
Original Russian Text Copyright © 2004 by Klochkova, Panchuk, Yushkin, Miroshnichenko.

Polarimetry of the Protoplanetary Nebula AFGL 2688

V. G. Klochkova[1], V. E. Panchuk[1], M. V. Yushkin[1], and A. S. Miroshnichenko[2,3]

[1]*Special Astrophysical Observatory, Russian Academy of Sciences, Nizhniĭ Arkhyz, Karachaĭ-Cherkessian Republic, 357147 Russia*

[2]*Main Astronomical Observatory, Russian Academy of Sciences, Pulkovskoe sh. 65, St. Petersburg, 196140 Russia*

[3]*Ritter Observatory, University of Toledo, Toledo, OH 43606–3390, USA*

Received September 10, 2003; in final form, November 10, 2003

Abstract—Our spectroscopic (with resolution $R = 75\,000$) and spectropolarimetric ($R = 15\,000$) observations with the 6-m telescope of the Special Astrophysical Observatory have enabled us to distinguish photospheric and circumstellar features in the optical spectrum of the bipolar protoplanetary nebula AFGL 2688 for the first time. The linear polarization of the radiation was measured at 5000–6600 Å. The emission in the lines of the sodium doublet and the Swan bands is formed in the envelope, and the mechanism exciting the transitions is resonance fluorescence. We conclude that the circumstellar envelope has a low density. Features of the structure of the nebula are discussed based on published high-angular-resolution photometric and polarimetric (HST NICMOS) data. *© 2004 MAIK "Nauka/Interperiodica".*

1. INTRODUCTION

Mass loss on and after the asymptotic giant branch (the AGB and post-AGB stages) is accompanied by the formation of a gas and dust envelope. The angular size of this envelope can be below the resolution limit for ground-based telescopes. In this case, asymmetry of the envelope can be detected from the presence of radiation polarized by scattering on the envelope's dust component. The degree of polarization depends on the scattering conditions and the extent to which the star providing the unpolarized light is obscured. The protoplanetary nebula AFGL 2688 is one of three bipolar post-AGB structures resolved by ground-based telescopes [1, 2]. Thirty years ago, the optical image of the source was thought to represent a pair of compact blue galaxies, IV Zw 67, at a distance of 30 Mpc [3]. During the flights of the AFCRL rockets in 1975, a source that was unusually bright at 10 and 20 μm and was not present in the 2.2 μm catalog of Neugebauer and Leighton [4] was detected. The nebula's optical image consists of two elliptical lobes with different brightnesses elongated approximately north–south. The central object illuminating the lobes is hidden from the observer by a dark bridge, thought to be a dust disk or torus. High-angular-resolution HST observations [5] have increased the number of objects similar to AFGL 2688 to nine. The parameters and atmospheric chemical composition of the central star were determined in [6]. Here, we discuss published polarimetric data and present the results of new high-angular-resolution polarimetric observations aimed at distinguishing the radiation of the central star from that of the circumstellar envelope of AFGL 2688. We selected this object, known (from broadband polarimetry) for its high degree of polarization, for the development of our method.

2. OBSERVATIONS AND REDUCTION

Since these are the first high-spectral-resolution spectropolarimetric observations of a post-AGB object, the observational method requires some discussion. Medium resolution is preferable for most spectropolarimetric observations, with the exception of studies of magnetic main-sequence stars, when measurement of the four Stokes parameters within the profiles of magnetically sensitive lines makes it possible to map the stellar magnetic fields [7, 8]. In other cases, the spectral resolution is chosen based on the fact that, since the polarization of spectral features is low, it is necessary to obtain signal-to-noise ratios for such features appreciably higher than the values characteristic of spectrophotometric measurements of unpolarized light. Within the possibilities provided by a single telescope, this can usually be achieved by reducing the spectral resolution, which is often done without taking into consideration the ratio of the line's width to the detector's resolution. A more detailed consideration shows that the problem cannot be solved so trivially; as an example, we consider the estimation of the uncertainties of equivalent widths, W.

1063-7729/04/4804-0288$26.00 © 2004 MAIK "Nauka/Interperiodica"

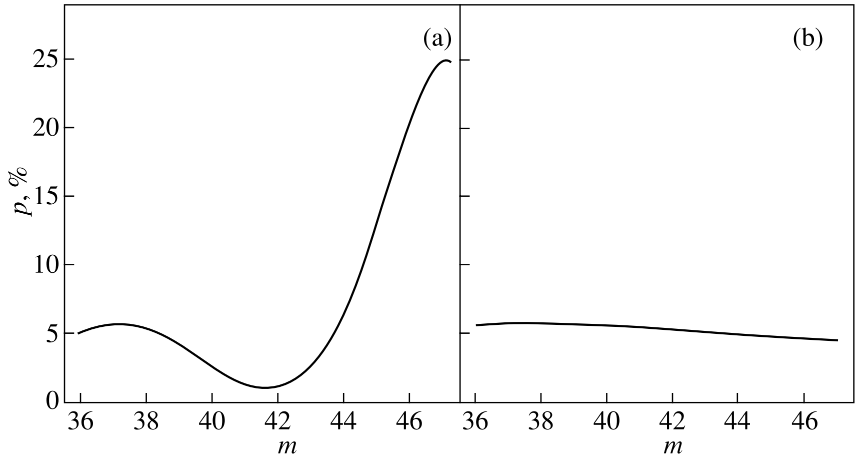

Fig. 1. (a) Instrumental polarization, p, measured from spectra of the zero-polarization standard ζ Peg in the center of each order with number m [11]. (b) Polarization as a function of m from spectral measurements of the polarization standard HD 204827. The instrumental polarization has been subtracted.

For equal numbers of counts, N, detected during an exposure per unit wavelength (Ångstrom), the uncertainty in the equivalent width is inversely proportional to the square root of the spectral resolution, R, when the light detector's pixel width, s, is larger than the line's width, l [9]. Thus, if $s > l$, it is advantageous to increase the spectral resolution, R, and not N, if the latter must be achieved by increasing the total exposure time. This statement is correct if the readout noise is negligible (as is true for spectrophotometric observations). Thus, the most "economical" spectral resolution (for measurements of W) is the R value providing a linear resolution equal to the spectral line width ($s = l$).

Post-AGB stars are surrounded by cool envelopes with narrow lines, and the condition $s < l$ is satisfied only if $R > 60\,000$. For this reason, it is desirable to approach such resolutions if one wishes to use spectropolarimetric observations to separate the light emitted by the star and envelope. Below, we show that increasing the spectral resolution by more than an order of magnitude (from $R < 1000$ to $R = 15\,000$) made it possible to obtain new spectrophotometric information and enabled us to improve the model of AFGL 2688. However, it is more useful to study the wavelength dependence of the polarization detected for a number of post-AGB objects over a wide spectral range [10] using medium-resolution spectra, since such spectra can also be used to detect (but not measure) polarization effects in individual spectral features.

Our high-spectral-resolution ($R = 15\,000$) linear-polarization measurements were obtained at the prime focus of the 6-m telescope of the Special Astrophysical Observatory (SAO) with the PFES echelle spectrograph [9] converted into a spectropolarimeter [11]. Observing at the prime focus makes it possible to avoid the effects of instrumental polarization produced at the third (flat) mirror of the 6-m telescope. We simultaneously recorded wavelengths of 4950–6630 Å. The width of a pixel of the light detector (a CCD chip with 1160 × 1040 elements) corresponded to a radial-velocity interval of 7.7 km/s. A broadband (600–700 nm) image of the nebula is shown in Fig. 1 of [1]. We observed the nebula's northern lobe, with the slit center placed on the main axis of the nebula (the line connecting the centers of the optical lobes), $5''$ from the nebula's center, which is hidden by a dark bridge. The effective magnitude of the part of the image that fit into the slit was 15.5^m. During each of the exposures, we rotated the spectrograph to compensate for the rotation of the field that is characteristic of telescopes with altitude–azimuth mounts. During the spectropolarimetric observations, we kept the projection of the slit perpendicular to the nebula's main axis during one exposure, and turned it counterclockwise by 45° relative to the first position during the next exposure. Examples of the resulting spectropolarimetric echelle images are shown in Fig. 7 of [11]. In addition to the target object, we observed standard stars for which photometric data indicated either high polarization (several percent) or no polarization (zero-polarization standards). The position of the crystal optical axes of the analyzer relative to the spectrograph's elements was always the same.

We reduced the echelle spectrophotometric images with the ECHELLE software package of the MIDAS system using original algorithms tested for the reduction of observations of polarization standards [11, 12]. In particular, these algorithms make

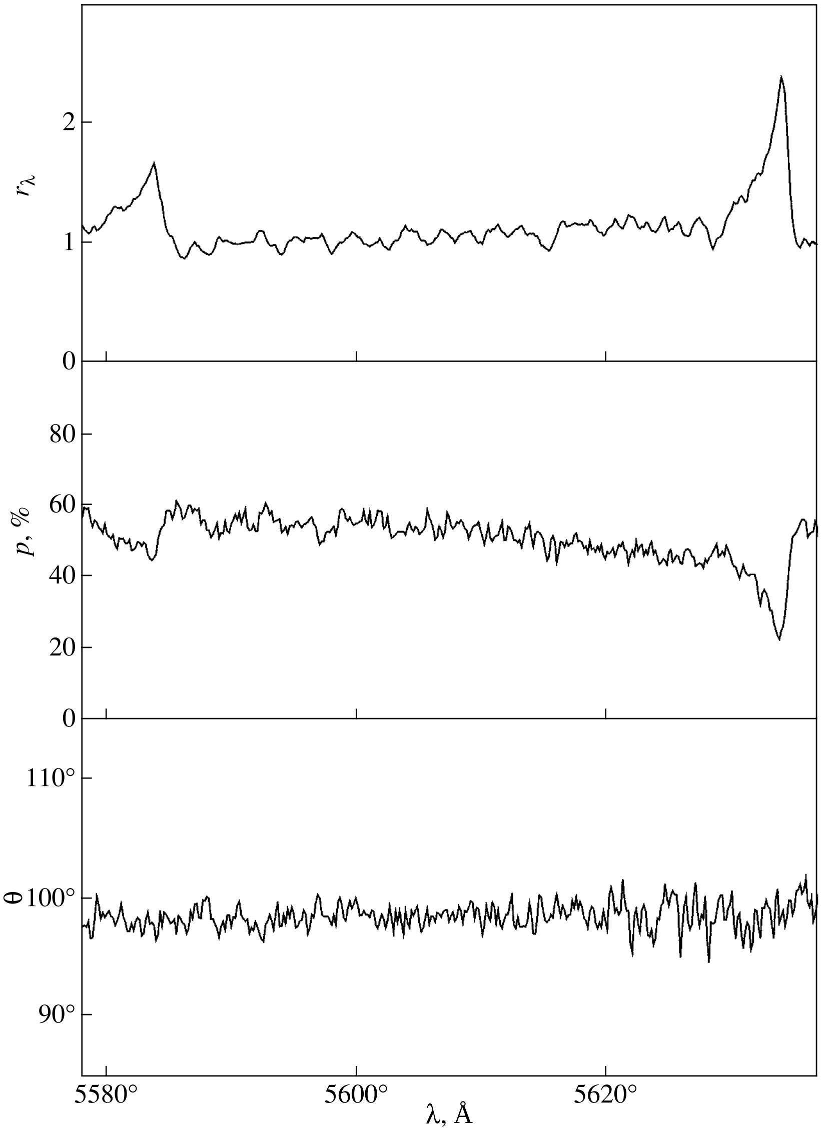

Fig. 2. Fragment of the spectrum ($R = 15\,000$) of the central part of the northern lobe of the AFGL 2688 nebula near the C_2 (1; 2) 5585.2 Å and (0; 1) 5635.5 Å Swan bands and graphs of the linear polarization and polarization position angle.

it possible to remove effects due to the fact that the spectrograph is not rigid, which appear when the projected position angle of the slit is changed by 45°, i.e., during rapid repositioning of the spectrograph. A characteristic feature of spectropolarimetric observations with an echelle spectrograph is the complex relation between the instrumental polarization and the wavelength, which is determined mainly by the mutual position of the diffraction gratings operated in a cross-dispersion mode. For this reason, the planes corresponding to the largest polarization effects from the gratings likewise do not coincide. Together with the wavelength dependence of the polarization, which is different for different gratings, and also because of polarization effects in the antireflection coating of the lens components of the spectrograph optics, this leads to a complex wavelength dependence for the instrumental polarization. Figure 1a shows the instrumental polarization measured for the centers of the echelle orders during observations of zero-polarization standards. An example of correction for this relation is presented in Fig. 1b, which shows the variation of the polarization with wavelength for the standard HD 204827, whose polarization is known from broadband photometry to be 5.4% in the V band [13].

Figure 2 shows part of the spectrum of AFGL 2688 near the (0; 1) band of the C_2 Swan system, along with the calculated parameters of the linear polarization. Note that the scatter in the polarization angle is due to the poor statistics of the signal, but the mean angle Θ is close to the value 99° ± 6°, known from broadband polarimetric observations [1]. When comparing the accuracy of our spectropolarimetric measurements with the broadband polarimetric results, we must keep in mind that the width of each of our spectropolarimetric channels is more than three orders of magnitude smaller than in the case of broadband polarimetric observations. On the other hand, these channels are not sufficiently narrow to enable detailed measurements of the polarization within individual emission features in the spectrum. For example, the residual polarization in the core of the emission components of the sodium doublet (Fig. 3) is partially due to the effects of convolving the object's spectrum with the instrumental function of the PFES spectropolarimeter.

In our analysis, we also use a spectrum of AFGL 2688 taken with the NES quartz echelle spectrograph [14], equipped with an Uppsala CCD chip [15]. The spectrum was acquired with an image slicer [16], providing a resolution of $R = 75\,000$. Fragments of this spectrum were presented in [17], which also gives the systemic radial velocity (~ −34 km/s), the radial velocity measured from photospheric spectral lines (~ −15 km/s), and the radial velocities measured from the envelope's spectrum (~ −55 km/s). The results of our analysis of the star's radial-velocity variations and estimation of the atmospheric line parameters will be presented elsewhere.

3. DISCUSSION OF THE RESULTS

We have analyzed the results of our high-spectral-resolution spectropolarimetry combined with published photometric, broadband polarimetric, and medium-resolution spectropolarimetric data.

3.1. Broadband Polarimetry

Ney *et al.* [1] present the collected results of the first Johnson *BVRIHKN* polarimetric measurements. On average, the polarization was about 40% in the *BVRI* bands; 31% in the *H* band, possibly underestimated due to insufficient sensitivity of the analyzer; 20 ± 7% in the *K* band; and less than 1% in the *N* band. The wavelength dependence of the polarization was studied in [18–20]. The linear polarization of the source as a whole at 3700–8800 Å increases linearly with wavelength (from 40 to 50%), independent of the size of the entrance diaphragm (in photometric observations of the nebula as a whole, the contribution from the northern lobe dominates). No changes in the polarization were detected in five months of observations.

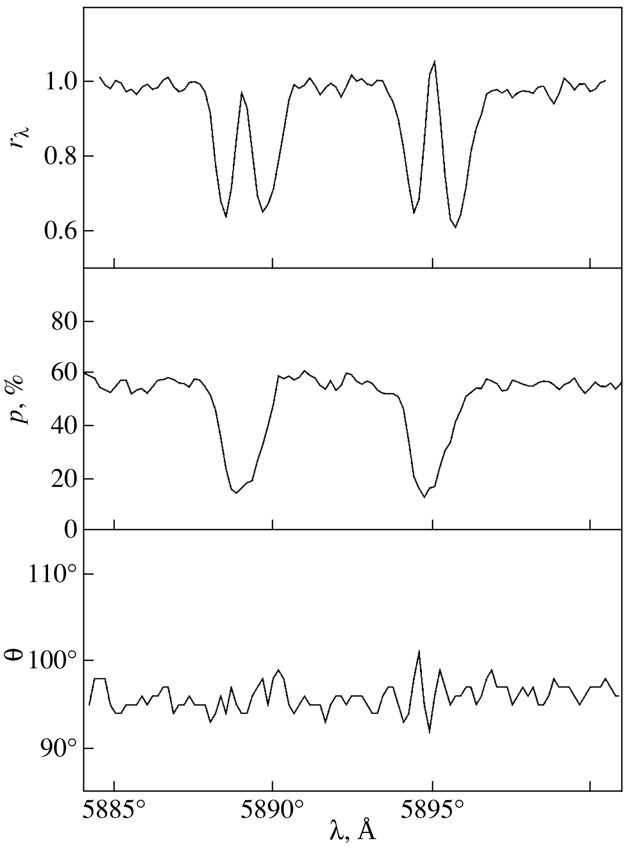

Fig. 3. Same as Fig. 2 for the region of the resonance sodium doublet.

The observations were then compared to a model for polarization induced by interstellar clouds [20] for various ratios of the cloud's depth and length (size in the plane of sky), assuming that the direct light from the star is completely blocked. It was concluded that the observed polarization corresponded to a ratio of the cloud's depth to its length less than 1/10 and that the wavelength dependence of the polarization agreed with the expectations for graphite grains better than those for silicate grains [20]. Measurements at 1.2 and 2.2 μm demonstrated that the polarization decreased with wavelength beyond 1 μm, which can be explained by an increasing contribution from unpolarized thermal emission from the dust envelope [21].

Circular polarization of −0.67% that was constant at 3800–7700 Å was detected in [18, 19]. This circular polarization could be due to the effects of scattering in the nebula or to the polarizing action of the interstellar medium (ISM). It was demonstrated in a model for scattering by cylinders of infinite length [22] that the wavelength dependences of the circular polarization are very different for different indices of refraction *m*. The modeling demonstrated that, in addition to strong wavelength gradients of the circular polarization, a change of the sign of the circular polarization should be observed in the optical. If linearly polarized light passes through an ISM containing aligned anisotropic grains, and if the polarization angle of the light entering the ISM does not coincide with the positions of either of the optical axes of the ISM grains, then a circular-polarization component will be formed. This idea was the basis of the classic study [23], in which the ISM was probed by the passage through it of synchrotron radiation from the Crab nebula [23]. The Crab nebula's intrinsic degree of polarization is the same at different wavelengths, and only the polarization angle is different in different parts of the nebula. The wavelength at which the sign change of the circular polarization in the ISM occurs depends on this angle.

The circular polarization of AFGL 2688 remains the same over a wide wavelength range, so the hypothesis that the circular polarization has an interstellar origin can be rejected. The unusually high linear polarization and the "favorable" orientation of the bipolar structure (the main axis is nearly in the plane of the sky) lead to thoughts of single scattering on nonspherical (elongated) grains that are smaller than the wavelength and are aligned along the nebula's main axis. In this case, the dynamic interaction of the grains with the outflowing gas could provide the alignment mechanism [24]. The predominance of single scattering on small grains contradicts the formation of the circular polarization via repeated scatterings on grains whose size is comparable to the wavelength. Elliptically polarized light can also result from single scattering of unpolarized light on dielectric (with a real index of refraction), nonspherical grains [25]. This problem was considered as a way to explain the elliptic polarization of the zodiacal light (for which the highest degree of circular polarization is 0.86% [26]), where the multiple-scattering mechanism is also ruled out due to the low concentration of the grains. In this case, the circular polarization will be zero if the symmetry axes of all the grains are perpendicular to the direction of the entering beam and/or are in the scattering plane. If the main axis of the AFGL 2688 nebula is in the plane of the sky, there should be no circular polarization of light scattered on the lobes if the grains are aligned perpendicular to or along the entering beam.

3.2. Photometry and Polarimetry of Images

(a) Panoramic optical polarimetry. Broadband polarimetric mapping of the nebula was undertaken at 4500–7000 Å [27]. The linear polarization of the weak southern lobe (60%) was significantly different from that of the bright northern lobe (50%). For the bipolar nebula M 1-92, the polarization of the weak southeastern lobe is 40%, while that of the bright northwestern lobe is 10% [27], with the relative brightness of the lobes differing more strongly than for AFGL 2688. Comparing the lobe polarizations and surface brightnesses suggests that there is a relation between the lobe brightness and the fraction of light that is singly scattered. The polarization is higher where the fraction of single scatterings (relative to all scatterings) is higher, so that the total number of scatterings, and also the surface brightness, is lower (compared to the opposite lobe with lower polarization, where the contribution from multiple scatterings is higher). An important conclusion follows: the difference in the brightnesses of the lobes of a bipolar nebula demonstrating considerable polarization could be due not to different illumination by the central source but to different numbers of scattering grains, with this effect being more pronounced when the optical depth of the lobes to scattering is low. In this case, the peripheral parts of lobes with lower surface brightness should exhibit higher polarization, as is observed [27]. The lobes' low optical depth to scattering agrees with their low surface brightness: a supergiant with an absolute magnitude of -6.7^m [6] at a distance of 1 kpc has an apparent magnitude of 3^m, whereas the nebula's integrated V magnitude is only 12.2^m [1]; this drastic difference cannot be explained by interstellar absorption or radiation-dilution effects in the nebula's volume. We can assume that most of the light from the central star passes through the volume of the lobes without hindrance.

(b) Panoramic IR polarimetry. Narrowband, high-angular-resolution HST NICMOS polarimetric measurements were made at 1.99 μm to determine the position of the central star illuminating the nebula's lobes [28]. The polarization of the lobes in the near-IR is nearly 10% higher than in the optical, and the polarization-angle map also demonstrated point symmetry. The source of optical light detected in this way is too far from the compact IR source for them to be considered a close binary that is determining the character of the mass loss of the post-AGB star.

Thus, we can summarize the results of optical and near-IR polarimetry as follows. The grains, thought to be graphite, are small (not larger than 0.1 μm), aspherical, and should be aligned in a direction consistent with the linear- and circular-polarization parameters. The role of interstellar polarization is negligible. Absorption in the lobes can also be neglected. The high polarization at 2 μm testifies to an insignificant contribution in the near IR from the dusty component of the lobes themselves.

3.3. Optical and IR Morphology

The first models of the nebula explained the brightness difference for the northern and southern lobes of

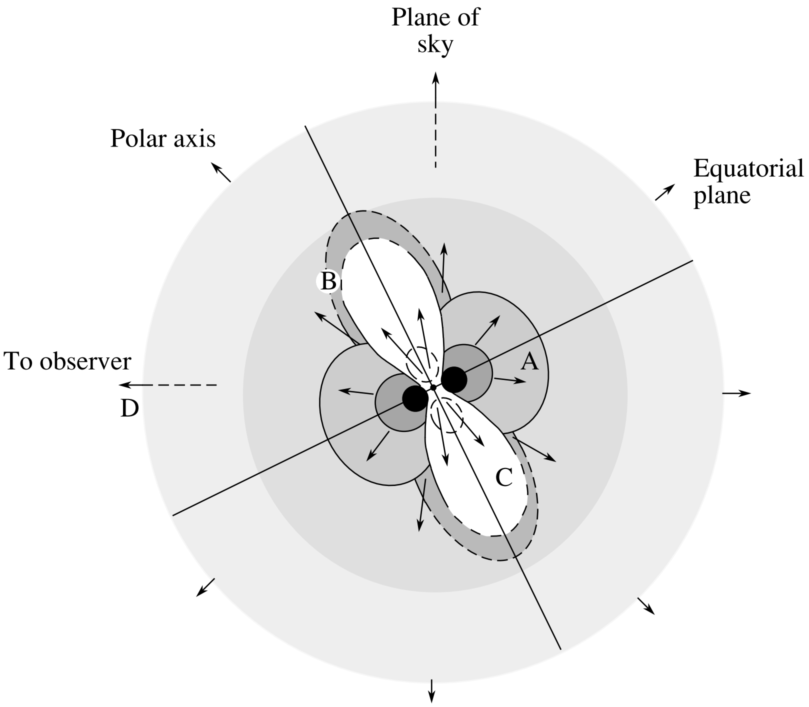

Fig. 4. Classic schematic of the AFGL 2688 [32] nebula. Shown are the disk expanding in the equatorial plane (A), shells expanding in the polar directions (B), wind cavities in these shells (C), and the cold, slowly expanding envelope (D).

AFGL 2688 in the optical as an effect of extinction of the radiation from the southern lobe in the peripheral zone of an extended equatorial dust disk. This interpretation is not consistent with the broadband polarimetric observations (the southern lobe is more strongly polarized); in addition, the small inclination of the disk's axis to the plane of the sky implies a very large size (more than 3000 AU), and such a disk should have a large mass and angular momentum.

Images of the nebula taken with ground-based instruments show a gradual change in the intensity along the axes of the elliptical lobes, which was interpreted in a model with an axially symmetric, monotonic distribution of the density of the dust component, which is concentrated toward the equator [29]. The slight deviations of the lobes from an elliptical shape—the so-called "horns" (cf., for instance, Fig. 1 in [1])—were modeled by appropriately choosing the gradient for the decrease in the grain density. Such a model, based on multiple scatterings on dust grains, does not explain the high polarization of the lobes of the AFGL 2688 nebula, which was known already after the first broadband photometric observations. A model based on multiple scatterings in the dust envelope assuming a constant scattering optical depth at 0.8–2.2 μm [30] remained the main model considered nearly until the HST observations of AFGL 2688 revealed fine structure of the lobes, which were resolved into a complex system of arcs and rays [31]. The horns, for which modeling results were used to identify the inclination of the nebula's axis, are not present in the high-resolution images.

Figure 4 shows a schematic of the nebula taken from [32]. Here, A is the disk expanding in the equatorial plane; B, shells expanding in the polar directions; C, wind cavities in these shells; and D, the cold, slowly expanding envelope. The high polarization of the optical lobes is explained as an effect of reflections from the inner walls of the cavities [32].

The inclination of the nebula's optical axis to the plane of the sky ($5^\circ-15^\circ$), which was used to interpret the spectroscopic measurements in the IR and radio, was obtained in an isotropic scattering model consistent with the flux ratios in the infrared bands and the intensity distribution along the lobes [33]. Additional evidence that this angle is small follows from the "natural" assumption that the nebula's main axis and the plane of the dust disk, which is observed nearly edge-on, are orthogonal.

The high polarization of AFGL 2688 in the optical and IR requires that the dust grains be small, $0.04 \leq a_0 \leq 0.08$ μm in size [34]. However, larger grains are needed to explain the centimeter-wavelength radiation from the dust disk detected by the VLA [35]: the spectrum at centimeter and millimeter wavelengths can be modeled by a power-law size distribution for the grains, with an index of 3.5 and the largest diameter of the grains being $a_C > 0.5$ cm. It is thought that the small grains are concentrated in the nebula's reflecting lobes, whereas the large grains are concentrated in a dense dust disk lying in position angle 53° [35].

The dust envelope of AFGL 2688 was modeled in [36] using the refined multiple-scattering mechanism of [30]. It was concluded that the broadband spectrum and the nebula's shape in the optical and IR could not be explained without the presence of larger grains (with radii of at least 5 μm). The spectrum in the optical and up to 3 μm is described by "gray" extinction; i.e., this likewise requires that the grains be large. The bipolar structure is clearly visible up to 5 μm; i.e., the scattering occurs on grains whose size is comparable to the wavelength. The mass of the envelope grains is $4.4 \times 10^{-8} d^2 M_\odot$ or, for a distance of $d = 1000$ pc, $4.4 \times 10^{-2} M_\odot$. For the gas-to-dust ratio that is usually adopted for the interstellar medium (158 ± 13), the envelope's total mass, estimated without taking into account the matter leaving the nebula volume, is $7 M_\odot$.

3.4. Spectropolarimetry

The first attempt to obtain spectropolarimetric observations with 7-Å resolution was undertaken with a 1.8-m telescope [37]. No difference was found in spectra taken at 5400–6800 Å for two orthogonal positions of the polaroid. Observations with a 3-m telescope revealed interesting wavelength dependences of the polarization [38]. At 4200–6700 Å with 7-Å resolution, high polarization was recorded in the continuum and in strong absorption features (50 and 60%, respectively, for the nebula's northern and southern lobes), whereas the polarization in the (0; 0), (0; 1), (1; 2) C_2 Swan emission bands was lower (by 10–15%).

Our observations with the 6-m telescope and spectral resolution more than an order of magnitude higher than in [38] ($R < 1000$) have made it possible to improve the relative contrast of the spectral features, i.e., to reliably separate the spectra formed in the F supergiant's atmosphere and in the extended gas and dust envelope illuminated by the central star.

First, the lobe spectrum demonstrates numerous absorption lines of the supergiant's atmosphere that disappear when the polarization is calculated; i.e., the polarization is the same in the lines and in continuum. This means that the main polarization mechanism acts outside the supergiant's atmosphere. Our observations show that, on average, the polarization in the continuum and photospheric lines of the northern lobe is 52% in the wavelength range studied.

Second, we find numerous emission bands formed in the circumstellar gas and dust envelope, with polarization minima observed at the positions of these bands (Fig. 2); i.e., the polarization of the emission bands is negligible compared to that of the photospheric light. Thus, the main polarization mechanism acts between the supergiant's photosphere and the formation region of the emission bands (or in that region). Assuming that the emission in the C_2 bands is not polarized, we used the energy distributions and polarizations for the most reliably measured bands—(0; 0), (1; 2), and (0; 1)—to calculate the spectrum of the polarized light. This yielded the continuum level of the photospheric spectrum under the emission bands in the polarized light. Consequently, we can take the characteristics of the photospheric spectrum to be those of the radiation exciting the corresponding molecular transitions when determining whether resonance fluorescence is likely to be acting [6, 39].

Third, other details of the wavelength distribution of the polarization were revealed: emission and absorption lines of the sodium resonance doublet, with the polarization near these lines being quite low (Fig. 3). Our analysis taking into account the higher-resolution spectrum ($R = 75\,000$) demonstrated that these emission lines, which also form in the gas and dust lobe of the nebula, were the doublet's unpolarized component. The continuum polarization is 57%, while the polarization in the doublet line cores is about 13%. Given the observed ratio of the fluxes in the emission and absorption components, these values are consistent with the hypothesis that the emission is unpolarized and that the absorption cores of the doublet's photospheric spectrum has a polarization similar to that of the continuum. We observed sodium line emission at least to distances of 10″ from the center of the northern lobe in the direction of the slit along an east–west line. This means that the lobe width in the sodium emission lines is at least twice the width in the continuum.

Let us discuss the influence of the spectral resolution on the interpretation of the spectrophotometric data, based on a comparison of our data with those of Cohen and Kuhi [38]. Our first comment refers to the C_2 bands. Spectrophotometry with medium resolution ($R < 1000$ with subsequent smoothing over five channels, yielding an effective $R < 300$ [38, Fig. 3]) showed that Swan absorption bands were observed in the polarized radiation. This suggested that these bands were formed before the light was scattered on grains, on the way from the star to the lobe region of the observed nebula. In addition, these absorptions overlap with unpolarized emission formed directly in the lobe. The resulting spectrum consisted of three components: the polarized photospheric spectrum, the envelope's molecular absorption spectrum, and the unpolarized spectrum formed in the lobes. We conclude from our observations ($R = 15\,000$) that the spectrum in the region of the Swan bands has only two components: the F supergiant's photospheric spectrum polarized on the dust component and the unpolarized emission bands. When separating the polarized and unpolarized components, the absorption bands do not stand out in the polarized light, and hence there is no need to place an additional cool molecular envelope between the photosphere and the nebula's lobe. We believe that the appearance of the absorption band in the polarized light is due to the slight (11%) excess of the emission band's head over the continuum level in [38]. This excess in the high-resolution spectrum is 140% ($R = 15\,000$), and our NES observations demonstrate that the excess is preserved when the spectral resolution is further increased (to $R = 75\,000$), so that the PFES spectropolarimetry of the Swan bands is already free of the effects of insufficient resolution.

Our second comment deals with the sodium resonance doublet. Strong absorption in the blend of the sodium doublet was revealed in [38] in the spectra of both lobes when observed in polarized light, whereas the spectrum of the northern lobe in unpolarized light shows weak absorption, and the spectrum of the southern lobe, weak emission. Our spectra resolve the doublet, and it is evident that the emission components are at least twice as narrow as the absorption components in the polarized light. The atmospheric absorption lines already demonstrate an asymmetry at $R = 15\,000$. The envelope's emission component provides the unpolarized part of the complex profile. The unpolarized absorption components, which could be formed at the edge of the nebula's lobes as well as in the ISM, equally attenuate the polarized and unpolarized components and, thus, cannot be isolated by means of spectropolarimetry. The contribution from the unpolarized emission component can be identified when the spectrum (Fig. 3a) is compared with the distribution of the polarization (Fig. 3b).

Our third comment concerns the Hα profile. The spectra presented in [38] demonstrate no statistically significant variations of the polarization in the region of Hα. Our high-spectral-resolution spectropolarimetry revealed a decrease of the polarization in the absorption core of the Hα line. It is apparent from Fig. 5 that the polarization in the line core is considerably lower, by approximately 15%. The polarization angle does not vary along the Hα profile within the uncertainties.

The profile of the Hα line consists of an absorption component with a narrow core and broad wings and an emission component, which presumably has several parts [6, Fig. 1]. The position of the core corresponds to a radial velocity of -17 ± 1 km/s. The reason for the slight blue shift relative to the velocity system of the photospheric absorption spectrum could be the influence of the Hα line's envelope component, formed on the way from the star's photosphere to the nebula's lobe. Figure 5 shows the profile of the Hα line and the degree and angle of the polarization. We can see that the polarization changes from 50% in the continuum to 35% within the line profile; the position of the polarization minimum is nearly coincident with the line's core and is shifted from it only slightly, by 8 ± 5 km/s toward longer wavelengths; and the polarization angle is constant within the errors. The presence of a slight emission component distorting the red wing of the Hα line [6] is not reflected in the polarization variations, providing evidence that the emission has a circumstellar origin; i.e., it originates in the region between the star and the nebula's scattering lobes. The decreased polarization may be due to a higher contribution from unpolarized light, as well as to an increased optical depth that leads to multiple scatterings of the radiation and possible depolarization. There are three possible origins for the polarization minimum in the core of the Hα line: the presence of (i) a narrow unpolarized emission component formed in the core, (ii) an unpolarized emission component whose width exceeds that of the Hα absorption profile, or an unpolarized continuum without lines (for example, due to the envelope's intrinsic thermal emission), or (iii) an absorption component formed after scattering on the grains in the nebula's lobe. Let us consider these three possibilities in more detail.

(1) The narrow unpolarized emission should be formed directly in the nebula's lobe or in outer regions (relative to the lobe), and the matter responsible for the Hα emission should have a line-of-sight projected velocity of ~ 40 km/s away from the observer relative to the system's center of mass. We can estimate the intensity of the hypothetical emission component based on the decrease in the polarization, from 50% in the continuum to 35% in the line core, with the residual intensity in the core being 0.45, resulting in a value of (10–15)% of the continuum intensity near the Hα line.

(2) In the presence of a broad emission base whose width exceeds that of the Hα absorption wings or in the case of a lineless continuum, the decrease of the polarization follows from the lower contribution of the polarized light in the core of the Hα line compared to the continuum. Consequently, the position of the polarization minimum should coincide with the line core independent of the velocity of the matter forming the unpolarized radiation. We can estimate the intensity of the unpolarized light from the absorption line's depth and the change in the polarization, which is (20–25)% of the continuum level at the Hα line, while the polarization of the photospheric spectrum should

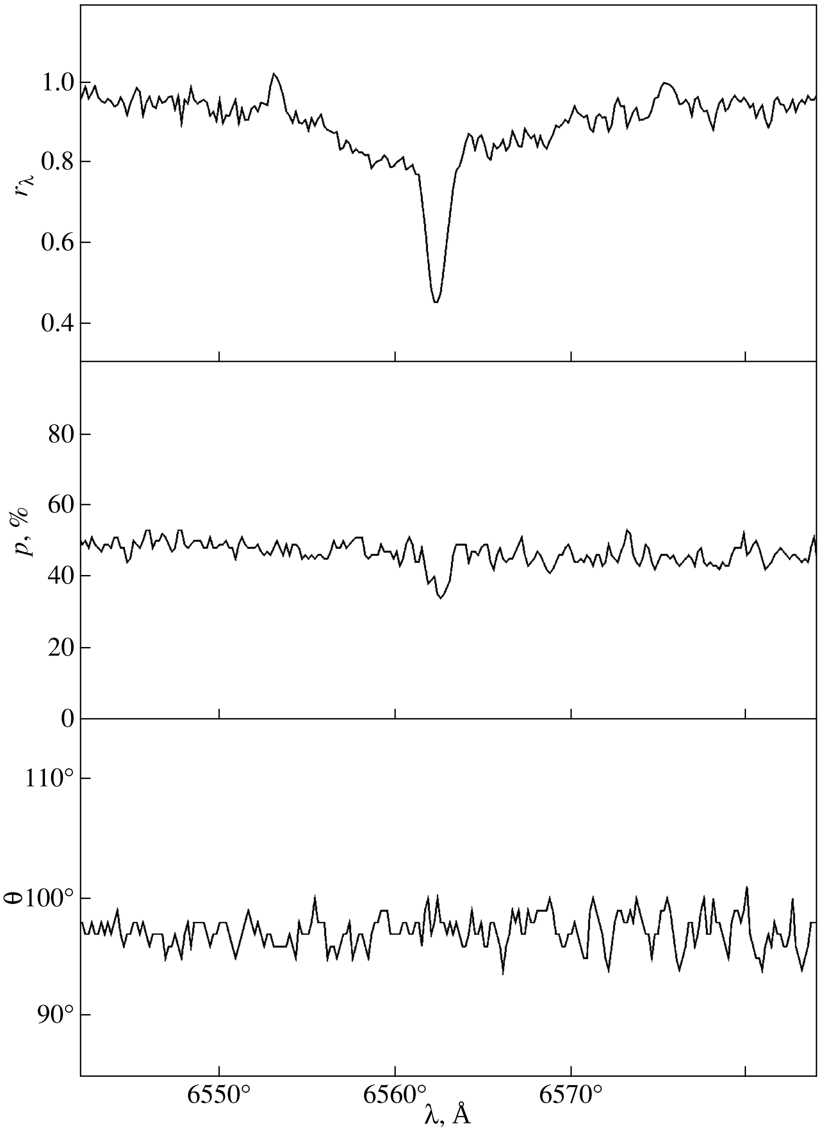

Fig. 5. Same as Fig. 2 for the region of the Hα hydrogen line.

be ∼60%. The envelope's intrinsic thermal emission cannot provide this unpolarized radiation, because an even higher continuum polarization is observed in the near-IR. In addition, a broad emission base in the Hα line due to high-velocity motions should have been detected via radio spectroscopic observations. Thus, we reject this interpretation of the polarization minimum in the Hα core.

(3) The polarization in the core of an absorption line formed in the nebula's lobe can also decrease on its way to the observer. The depolarizing factor is resonance scattering of photons on hydrogen atoms. In this case, as in the first possibility, the line-of-sight velocity of the absorbing matter should be ∼40 km/s away from the observer, relative to the systemic velocity.

Spectropolarimetry of post-AGB stars with spectral resolutions of about $R = 1000$ [10] has suggested a division into four types of objects. Based on our observations, AFGL 2688 is a type Ic star: an object whose emission lines and continuum display different polarizations. This effect can arise if the direct light from the star is completely or partially obscured, so that we observe a considerable contribution from the star's scattered polarized light combined with unpolarized radiation from the envelope; alternatively, it is possible that both the star and the emission region are obscured but the polarizations of these components are different due to dilution of the radiation. Our high-resolution spectra, which are the highest quality spectropolarimetric data for a post-AGB star available to date, demonstrate that the emission of AFGL 2688 is essentially unpolarized.

Thus, our high-spectral-resolution spectrophotometric observations have enabled us to separate the components of the optical radiation formed in the central star's atmosphere and in the bipolar nebula's lobes. Analyzed together with high-angular-resolution images acquired with the HST, this suggests a new interpretation for the AFGL 2688 phenomenon.

3.5. Resonance Fluorescence of the C_2 Molecules

(a) The vibrational spectrum of C_2. Crampton *et al.* [37] detected the C_2 5162 Å (0; 0) and 5631 Å (0; 1) emission bands but not the 4737 Å (1; 0) band, although their blue spectrograms had a resolution of $R = 3000$ (1.5 Å), a factor of three higher than their red spectrograms ($R = 1000$, 7 Å). Eight emission bands belonging to the $\Delta_v = -1$ and $\Delta_v = -2$ sequences as well as to the diagonal sequence ($\Delta_v = 0$), but no bands of the $\Delta_v = +1$ sequence, were detected in [6] in a spectrum with $R = 15\,000$. Using our spectrum with $R = 75\,000$ (4653–6080 Å), we measured the intensities (in units of the continuum) for the heads of seven emission bands (see the table). We found no trace of the 4737.1 Å (1; 0), 4715.2 Å (2; 1), 4697.6 Å (3; 2), 4684.8 Å (4; 3), 6004.9 Å (3; 5), or 6059.7 Å (2; 4) bands in the spectrum.

Taking into account the nebula's continuum energy distribution [37], we determined the flux ratios for the heads of the (1; 0), (0; 0), and (0; 1) bands to be 1.2 : 3.2 : 5.6 (the continuum fluxes read from Fig. 2 in [37] indicate the flux ratios 1.2 : 1.6 : 2.5). Calculations of the molecular-band absorption coefficients in a Boltzmann approximation for the level populations ($T = 2500$ K) using the hypothesis of overlapping lines [40] show that the opacities near the heads of the (1; 0), (0; 0), and (0; 1) bands have the ratios 1.6 : 4.0 : 0.4 (the cross sections per grain on a logarithmic scale have the ratios −16.8 : −16.4 : −17.4). For these bands, the ratios of the Franck–Condon factors, $q(v', v'')$, are 0.25 : 0.72 : 0.22 [41]. Thus, when the populations of the vibrational levels are in equilibrium, the emission intensity in the (1; 0) band should be intermediate between those in the (0; 0) and (0; 1) bands. We conclude that the vibrational levels of C_2 have non-Boltzmann populations and that the intensity behavior of the vibrational–rotational bands repeats the energy distribution in the supergiant's spectrum. This provides evidence for the action of resonance fluorescence.

Note that the resonance-fluorescence hypothesis removes the difficulties encountered by Cohen and Kuhi [42] when explaining the emission-band intensities by invoking the effect of circumstellar reddening.

Relative intensities of the heads of the C_2 Swan bands in units of the continuum intensity

λ, Å	(v', v'')	q	I/I_c
5097.7	(2; 2)	0.117	1.078
5129.4	(1; 1)	0.330	1.370
5165.2	(0; 0)	0.724	1.988
5501.9	(3; 4)	0.202	1.072
5540.7	(2; 3)	0.265	1.164
5585.2	(1; 2)	0.286	1.723
5635.5	(0; 1)	0.220	2.235

They estimated the extinction in the nebula to be 8.1^m and 11.5^m in the directions from the star to the northern and southern lobes, respectively. These estimates do not agree with the extinction derived from the interstellar component of the sodium doublet (4^m) [42], which we believe to be severely overestimated due to an order-of-magnitude error in the use of the equivalent widths of [42] (see [6] for details).

(b) The rotational spectrum of C_2. The possible action of resonance fluorescence is also supported by the presence of photospheric absorption lines overlaid by the molecular emission spectrum. For example, the CaI 5581.98 Å line, with a photospheric radial velocity of −14.8 km/s, is confidently observed near the head of the (1; 2) 5585.5 Å band, but there is no rotational C_2 spectrum near this line. If a different mechanism were exciting the C_2 spectrum, this CaI line should have been overlaid by the $P_1(21)$ rotational emission line. The FeI 5159.06 Å line is observed near the head of the (0; 0) 5165.2 Å band, whereas the blend of the $P_1(27) + P_2(28)$ rotational lines is not seen (although neighboring, weaker lines of the C_2 spectrum can be reliably identified).

Our observations with $R = 75\,000$ showed that the mean radial velocity for the heads of four emission bands (−55 km/s) is in good agreement with the radial velocity from the emission components of the sodium doublet (−54 km/s). This indicates that the kinematic characteristics of the corresponding formation regions are similar; i.e., the regions in which the C_2 lines with low rotational quantum numbers, J, and the sodium-doublet emission are generated are similar.

The optical spectra of AFGL 2688 can be used to determine if fluorescent equilibrium has been established at the rotational levels of C_2. For this purpose, we will make an analogy with the behavior of the C_2 rotational lines in the spectra of comets. The C_2 molecules in cometary atmospheres are produced by the dissociation of C_2H_2 molecules, with the formation of C_2H as an intermediate step; further, the C_2 molecules are also photodissociated by the solar radiation. The distance from the region in which the C_2 molecules formed to the zone where the statistical equilibrium for C_2 is reached is determined by the time scale for achieving equilibrium (10 min) and the outflow velocity (1 km/s). Adding the distances to the formation zones of the C_2H_2 and C_2H molecules, it is possible to estimate the distance of the maximum C_2 concentration from the cometary nucleus. The rotational structure of the C_2 (0; 0) Swan band in the spectrum of Halley's comet was analyzed in [43]. Two values of the rotational temperature were obtained in a Boltzmann approximation: about 3000 K for levels with $J > 15$ and 190 K for levels with $J < 15$. It was concluded that fluorescence could successfully describe the levels with large J quantum numbers, while the newly formed molecules with low J values had not yet achieved fluorescence equilibrium. If collisional processes are as efficient as fluorescence, the lines have a low rotational temperature, reflecting the kinetic temperature of the gas. It was shown in [44] that a balance between collisional and radiative processes in cometary atmospheres was reached at particle densities of about 10^{10} cm^{-3}; at lower densities, fluorescence equilibrium is achieved. The conditions in the envelopes of protoplanetary nebulas differ from those in cometary heads in the following aspects. First, there are two sources of photodissociation: the central star's light and external UV radiation from the ISM. Second, the outflow velocities are an order of magnitude higher, although the role of this factor is negligible because of the large distance to the object (the distance covered by the newly formed molecules before they reach the zone of statistical equilibrium is within the projected width of the spectrograph's slit). If the fraction of newly formed C_2 molecules is high for the observed part of the lobe and collisional processes are significant, the low-J levels should have their Boltzmann populations for a temperature that is close to the gas temperature. The low-J rotational lines whose positions coincide with the photospheric absorptions (with the Doppler shift taken into account) should have Boltzmann intensities, i.e., emission lines that are positionally coincident with photospheric absorption lines should not be weakened, since the fluorescence processes are predominant. Near the heads of the C_2 bands in the spectrum of AFGL 2688, we observe deviations of the rotational-line intensities from a Boltzmann distribution due to photospheric absorption, i.e., to a deficiency of illumination. This suggests that fluorescent equilibrium has been achieved and that the gas in the lobe has a low density (below 10^{10} cm^{-3}).

Thus, the ratio of the intensities of the vibrational and rotational bands in the C_2 spectrum provides further evidence for a low gas density in the lobe. This density can be made considerably lower if we estimate the mass of gas in the nebula's envelope. Let us suppose that only stars with main-sequence masses not exceeding 8 $M_\odot$ can reach the post-AGB stage. We can calculate the nebula volume from the angular size assuming a distance of 1 kpc. If all the "excess" mass was ejected but did not leave the volume, we obtain a maximum density that is at least five orders of magnitude lower than 10^{10} cm^{-3}. This represents additional evidence for the action of resonance fluorescence and for a high transparency of the lobes.

3.6. Character of the Matter Distribution

What determines the shape of the optical lobes—the character of the nebula's illumination or the distribution of the scattering material? High-angular-resolution images reveal quasi-concentric luminous arches reaching as far as the plane of the dark bridge [31]. This suggests that the solid angle within which the nebula material is illuminated is large ($\sim 170°$, projected onto the plane of the sky). The arches apparently reflect the nonmonotonic character of the envelope's ejection during the AGB stage, and we can accordingly assume that the light from the arches is due to gas-dynamical effects and not to scattering of the illuminating radiation. However, the quasi-concentric arches do not show the ellipticity (1.6–1.3) that follows from models for the latitude variations of the gas density and of the drift velocity of the dust grains [29, 30]. Similar arches have been found for objects with larger inclinations for their main axes [45].

The optical lobes glow predominantly in the continuum (the contribution from C_2 and NaI emission is negligible). Thus, the lobe region contains continuum-scattering material, and since the scatterings are single, it is natural to assume that there is virtually no scattering material outside the lobes. The lobes consist of numerous radial rays that can be traced, like the regions of shadow between them, to distances of tens of arcseconds [31], confirming that the star's light undergoes single scattering on the dust component of the envelope (the contrast of the rays would be lower in the case of multiple scatterings). The polarization plane is perpendicular to the rays [27, 28], indicating that the polarizing (scattering) agent is related to the rays. This possibility is also supported by the higher contrast of the rays in the southern lobe [31], where the polarization is higher [27]. The lobes are the brightest in regions with a higher density of rays. The polarization in regions between the rays is lower than in the rays (cf. the image of the inner part of the southern lobe, Fig. 1 in [28]).

The presence of long, narrow, high-contrast rays is inconsistent with multiple-scattering models. A fairly exotic "searchlight" scheme was suggested to explain the existence of such narrow rays ($\sim 0.1''$): the star is in a cocoon with near-polar windows that form annular holes that let the narrow beams escape [31]. In this picture, the brightnesses of the lobes differ because the cocoon with near-polar windows surrounding the star has a larger optical depth in the direction of the southern lobe than in the direction of the northern lobe. When interpreting the HST images, it was supposed [31] that the existence of the dark inter-ray space did not prove the absence of scattering material there, since the first millimeter observations in CO lines showed a spherically symmetric, uniform distribution of matter in the nebula volume. However, high-angular-resolution interferometric observations have since been obtained and provide evidence that the nebula volume is filled nonuniformly with CO molecules [46]. In our opinion, the weak point in the searchlight scheme is the assumption that the volumes occupied by the luminous rays contain matter identical to that in the dark inter-ray space. The alternative possibility that scattering material is present in the region of the luminous rays and absent from the dark regions is equally plausible. In any case, precisely this picture is observed just beyond the outer boundaries of the lobes (the resonance sodium-doublet emission is observed in a much larger volume than the scattering of the photospheric spectrum). In a scheme in which the scattering material is restricted to the radial rays and concentric arches, there is no need to look for a mechanism operating near the central star that collimates the beams of light.

Our proposed picture, in which both hemispheres of the nebula are nearly completely illuminated by the central star (with the exception of the plane of the dark bridge), differs from models with wide, partially shaded cones [47] or a certain latitude dust distribution [29, 30, 36]. For this reason, estimates of the envelope mass based on the dust component's mass can be lowered.

4. CONCLUSIONS

We have carried out optical spectropolarimetry of AFGL 2688 with a resolution a factor of 50 better than those of previously published data. This has enabled us to distinguish the spectra of the central star and of the circumstellar envelope. The absorption lines in the spectrum of the central star have the same degree polarization as the photospheric continuum. Seven C_2 Swan emission bands, emission components of the NaI resonance doublet, and a narrow Hα component were identified in the envelope's spectrum. We have demonstrated that resonance fluorescence could excite the C_2 spectrum and conclude that the density of the nebula's lobes is low. Based on the results of polarimetric, high-spectral-resolution spectropolarimetric, and high-angular-resolution photometric and polarimetric observations, we have suggested a new picture for the nebula's structure.

When successfully applied, high-spectral-resolution polarimetric observations can be used to reveal gas and dust envelopes around protoplanetary nebulas observed from the ground with relatively low angular resolution.

ACKNOWLEDGMENTS

This study was supported by the Russian Foundation for Basic Research (project code 02-02-16085), the Federal Program "Astronomy," and the basic research program of the Physical Sciences Department of the Russian Academy of Sciences "Extended Objects in the Universe" (subproject "Spectroscopy of Extended Envelopes of Evolved Stars"). V.G.K. and M.V.Yu. were also supported by a grant from the President of Russia for young scientists (MK-874.2004.2).

REFERENCES

1. E. P. Ney, K. M. Merrill, E. E. Becklin, *et al.*, Astrophys. J. **198**, L129 (1975).
2. S. Kwok, B. J. Hrivnak, C. Y. Zhang, and P. P. Langill, Astrophys. J. **472**, 287 (1996).
3. N. Carozzi, P. Chamaraux, and R. Duflot, Astron. Astrophys. **33**, 113 (1974).
4. G. Neugebauer and R. B. Leighton, *Two-Micron Sky Survey. A Preliminary Catalog* (NASA, Washington, 1996), p. 309.
5. K. Y. L. Su, B. J. Hrivnak, and S. Kwok, Astron. J. **122**, 1525 (2001).
6. V. G. Klochkova, R. Szczerba, and V. E. Panchuk, Pis'ma Astron. Zh. **26**, 510 (2000) [Astron. Lett. **26**, 88 (2000)].
7. N. E. Piskunov, in *Magnetic Fields of Chemically Peculiar and Related Stars,* Ed. by Yu. V. Glagolevskij and I. I. Romanyuk (Moscow, 2000), p. 96.
8. O. P. Kochukhov, in *Magnetic Fields of Chemically Peculiar and Related Stars,* Ed. by Yu. V. Glagolevskij and I. I. Romanyuk (Moscow, 2000), p. 106.
9. V. E. Panchuk, I. D. Najdenov, V. G. Klochkova, *et al.*, Bull. Spec. Astrophys. Observ. **44**, 127 (1998).
10. S. R. Trammel, H. L. Dinerstein, and R. W. Goodrich, Astron. J. **108**, 984 (1994).
11. V. E. Panchuk, V. G. Klochkova, M. V. Yushkin, *et al.*, SAO Preprint No. 159 (Special Astrophysical Observatory, 2001).

12. M. V. Yushkin, Candidate's Dissertation in Physics and Mathematics (Spets. Astrofiz. Obs. Ross. Akad. Nauk, Nizhniĭ Arkhyz, 2002), p. 182.
13. D. A. Turnshek, R. C. Bohlin, R. L. Williamson II, *et al.*, Astron. J. **99**, 1243 (1990).
14. V. E. Panchuk, V. G. Klochkova, and I. D. Naĭdenov, SAO Preprint No. 135 (Special Astrophysical Observatory, 1999).
15. V. E. Panchuk, N. E, Piskunov, V. G. Klochkova, *et al.*, SAO Preprint No. 169 (Special Astrophysical Observatory, 2002).
16. V. E. Panchuk, M. V. Yushkin, and I. D. Naĭdenov, SAO Preprint No. 179 (Special Astrophysical Observatory, 2003).
17. V. G. Klochkova, V. E. Panchuk, and M. V. Yushkin, SAO Preprint No. 168 (Special Astrophysical Observatory, 2002).
18. J. J. Michalsky, R. A. Stokes, and P. A. Ekstrom, Astrophys. J. **203**, L43 (1976).
19. J. J. Michalsky, R. A. Stokes, and P. A. Ekstrom, Astrophys. J. **206**, L73 (1976).
20. S. J. Shawl and M. Tarenghi, Astrophys. J. **204**, L25 (1976).
21. T. L. Jones and H. M. Dyck, Astrophys. J. **220**, 159 (1978).
22. P. G. Martin, Mon. Not. R. Astron. Soc. **159**, 179 (1972).
23. P. G. Martin, R. Illing, and J. R. P. Angel, Mon. Not. R. Astron. Soc. **159**, 191 (1972).
24. T. Gold, Mon. Not. R. Astron. Soc. **112**, 215 (1952).
25. L. W. Bandermann and J. C. Kemp, Mon. Not. R. Astron. Soc. **162**, 367 (1973).
26. R. D. Wolstenkroft and J. C. Kemp, Astrophys. J. **177**, L137 (1972).
27. G. D. Schmidt, J. R. P. Angel, and E. A. Beaver, Astrophys. J. **219**, 477 (1978).
28. D. A. Weintraub, J. H. Kastner, D. C. Hines, and R. Sahai, Astrophys. J. **531**, 401 (2000).
29. M. Morris, Astrophys. J. **249**, 572 (1981).
30. F. Yusef-Zadeh, M. Morris, and R. L. White, Astrophys. J. **278**, 186 (1984).
31. R. Sahai, J. T. Trauger, A. M. Watson, *et al.*, Astrophys. J. **493**, 301 (1998).
32. R. Kawabe, M. Ishiguro, T. Kasuga, *et al.*, Astrophys. J. **314**, 322 (1987).
33. W. B. Latter, J. L. Hora, D. M. Kelly, *et al.*, Astron. J. **106**, 260 (1993).
34. M. Jura, S. P. Balm, and C. Kahane, Astrophys. J. **453**, 721 (1995).
35. M. Jura, J. L. Turner, S. Van Dyk, and G. R. Knapp, Astrophys. J. **528**, L105 (2000).
36. B. Lopez and J.-M. Perrin, Astron. Astrophys. **354**, 657 (2000).
37. D. Crampton, A. P. Cowley, and R. M. Humphreys, Astrophys. J. **198**, L135 (1975).
38. M. Cohen and L. V. Kuhi, Astrophys. J. **213**, 79 (1977).
39. V. G. Klochkova, V. E. Panchuk, R. Szczerba, and K. Volk, Astron. Astrophys. **345**, 905 (1999).
40. V. E. Panchuk, Candidate's Dissertation in Physics and Mathematics (Spets. Astrofiz. Obs. Ross. Akad. Nauk, Nizhniĭ Arkhyz, 1978), p. 167.
41. J. C. McCallum, W. R. Jarmain, and R. W. Nicholls, *CRESS Spectroscopic Report: Franck-Condon Factors and Related Quantities for Diatomic Molecular Band Systems,* No. 1, March 1970, York Univ.
42. M. Cohen and L. V. Kuhi, Publs Astron. Soc. Pac. **92**, 736 (1980).
43. D. L. Lambert, Y. Sheffer, A. C. Danks, *et al.*, Astrophys. J. **353**, 640 (1990).
44. R. Gredel, E. F. van Dishoeck, and J. H. Black, Astrophys. J. **338**, 1047 (1989).
45. B. J. Hrivnak, S. Kwok, and K. Y. L. Su, Astron. J. **121**, 2775 (2001).
46. P. Cox, R. Lucas, P. J. Huggins, *et al.*, Astron. Astrophys. **353**, L25 (2000).
47. C. J. Skinner, M. Meixner, M. J. Barlow, *et al.*, Astron. Astrophys. **328**, 290 (1997).

Translated by N. Samus'

Astronomy Reports, Vol. 48, No. 4, 2004, pp. 301–314. Translated from Astronomicheskiĭ Zhurnal, Vol. 81, No. 4, 2004, pp. 333–347.
Original Russian Text Copyright © 2004 by Klochkova, Chentsov.

Kinematics of the Envelope of the Post-AGB Star V510 Pup—Nucleus of a Future Planetary Nebula

V. G. Klochkova and E. L. Chentsov

Special Astrophysical Observatory, Nizhniĭ Arkhyz, Russia

Received September 10, 2003; in final form, November 10, 2003

Abstract—We have carried out a detailed identification of lines in the optical spectrum of the post-AGB star V510 Pup associated with the infrared source IRAS 08005−2356 based on observations with high spectral resolution. Absorption lines of the ions FeII, TiII, CrII, and YII are present at wavelengths from 4549 to 8546 Å. The absorption by YII and other s-process elements is anomalously strong, and the absorption is also strong in the circumstellar C_2 Swan bands. The profiles of most of the lines (of hydrogen and metals) display P Cygni absorption–emission profiles. All the absorption lines are shifted toward the blue, suggesting an outflow of stellar material. The expansion velocity of the envelope derived from the Swan bands arising there is $V_{exp} = 42$ km/s. The highest wind velocity determined from the absorption wings of the FeII(42) P Cygni profiles reaches 240 km/s. Based on the star's kinematic characteristics and the amount of interstellar absorption, it is at a distance of $d \approx 3$–4 kpc, which corresponds to an absolute magnitude of $M_v \approx -6^m$. *© 2004 MAIK "Nauka/Interperiodica".*

1. INTRODUCTION

The infrared source IRAS 08005−2356 (which we will call IRAS 08005) is situated near the Galactic plane, at Galactic latitude $b = 3.6°$. Iyenger and Parthasathy [1] identified IRAS 08005 with the peculiar variable star V510 Pup ($B = 13.07^m$, $V = 11.52^m$). The fluxes of IRAS 08005 indicate that this is very likely a member of the relatively small group of protoplanetary nebulas (PPNs) [2]. In the IR Veen–Habing diagram [3], IRAS 08005 lies in region IV, inhabited by protoplanetary nebulas with optically thick oxygen-enriched envelopes. The high optical depth indicates a very high mass-loss rate. The same part of the diagram contains IRAS 17436+5003, identified with the well-studied high-luminosity star HD 161796. In particular, based on their determination of the detailed chemical composition of the atmosphere of HD 161796, Klochkova *et al.* [4] suggested that there was an oxygen excess in the atmosphere and also detected an increase in the effective temperature of the star at a rate of roughly 50 K/yr.

The circumstellar envelopes of evolved stars are sources of maser radiation. Envelopes radiating in the OH 18 cm band are enriched with oxygen. Based on observations of a sample of IRAS sources in the OH 1612 MHz maser line, Likkel [5] classified IRAS 08005 as a member of a small group of sources identified with peculiar evolved stars with nonspherical envelopes. The OH profile in IRAS 08005 displays several peaks from $V_{lsr} = 0$ to $V_{lsr} = 100$ km/s, the systemic velocity is $V_{lsr} = 47 \pm 5$ km/s, and the heliocentric velocity is $V_{sys} = 61 \pm 5$ km/s [6]. IRAS 08005 has not been detected in CO [7], providing further evidence that its envelope is O-rich. No SiO maser radiation was detected from IRAS 08005, suggesting that the mass loss from the star has been terminated [8] (on the other hand, however, the P Cygni profiles observed in the optical spectrum suggest that the mass loss is ongoing). Parameters of the radio radiation in combination with the IR colors are consistent with the evolutionary phase following the asymptotic giant branch (post-AGB) stage. According to the chronological sequence derived by Lewis [9], the detection of OH emission at both 1612 and 1667 MHz in the absence of SiO and H_2O masers indicate the object is close to the planetary-nebula stage.

Ueta *et al.* [10] used the HST to survey reflection nebulas with low surface brightnesses that are candidate protoplanetary nebulas. The studied objects were divided into two types. IRAS 08005 was classified as a "duplex" object, with a pronounced asymmetrical or bipolar nebula. The image of IRAS 08005 displays two horseshoe-like lobes of unequal brightness. Previously, a bipolar structure for the envelope of IRAS 08005 was suggested based on the circular polarization of the OH radiation [7] and the linear polarization of the optical emission (up to 10% at wavelengths around 4000 Å) [10]. Ueta *et al.* [10] concluded that the observed morphology of the PPN is probably due to its mass and specific features of the

1063-7729/04/4804-0301$26.00 © 2004 MAIK "Nauka/Interperiodica"

system's evolution rather than to geometrical factors (the inclination of the axis of symmetry to the line of sight). In duplex objects, the radiation of the central star is substantially reduced, making it inaccessible for detailed studies. Duplex objects display high optical depths at both optical and IR wavelengths. Bipolar nebulas are concentrated in the plane of the Galaxy: for example, the latitude of the well-known bipolar nebula AFGL 2688 in Cygnus is $b = -6.5°$. The collected parameters of bipolar nebulas suggest that they originate from relatively high-mass stars. For instance, Klochkova *et al.* [12] showed that the initial mass of AFGL 2688 was about $8\,M_{\odot}$, which is close to the upper limit for the initial mass for stars that can undergo the PPN stage.

Here, we present the first results of optical spectroscopy of V510 Pup with the 6-m telescope of the Special Astrophysical Observatory. Previously, low-resolution spectral data were published by Slijkhuis *et al.* [13], who spectrally classified the star as an F supergiant (F5 Iae); it was noted that variations of the lines of metals in V510 Pup resemble those in ρ Cas and 89 Her. Slijkhuis *et al.* [13] also observed P Cygni profiles of Hα, Hβ, and the Na D sodium doublet. They derived $V_{lsr} = 47 \pm 5$ km/s from the observed emission lines. It was stressed that observations of the object with higher spectral resolution were needed.

2. OBSERVATIONS AND DATA REDUCTION

We observed V510 Pup with the 6-m telescope of the Special Astrophysical Observatory. Our first spectrum was obtained on November 23, 1997 ($\mathrm{UT} = 3^{\mathrm{h}}$), with the PFES prime-focus echelle spectrograph [14], which has a spectral resolution of $R = 15\,000$. In combination with the 1000×1000 CCD array, the spectrum covered the wavelength interval $\lambda\lambda$ 4680–8590 Å. The object was also observed multiple times at the Nasmyth focus of the 6-m telescope with the NES echelle spectrograph on November 19, 2002 ($\mathrm{UT} = 2^{\mathrm{h}}$) [15]. An image slicer [16] made it possible to achieve a spectral resolution of $R = 60\,000$. Due to the use of a large-format 2048×2048 CCD array, we were able to record the wavelength interval $\lambda\lambda$ 4515–5996 Å. The data were extracted from the two-dimensional echelle spectra using the ECHELLE context in the MIDAS package. Tracks of cosmic rays were removed via median averaging of two successive spectra. The wavelength calibration was performed using a ThAr hollow-cathode lamp spectrum. The further processing, including photometric and position measurements, was carried out using the DECH20 code [17]. This code makes it possible to determine the positions of individual spectral features that bring into coincidence the direct and mirror images of their profiles. Instrumental shifts of both the stellar and lamp spectra were checked and corrected using O_2 and H_2O telluric lines. The laboratory wavelengths of most of the lines were taken from the tables for the solar spectrum of Pierce and Breckinridge [18] (with corrections for gravitational redshifts), as well as from the tables of Johansson [19] (FeII) and Striganov and Odyntsova [20].

3. DISCUSSION AND RESULTS

3.1. Peculiarities of the Optical Spectrum of V510 Pup

Table 1 presents identifications of the spectral lines and the residual line intensities r. The absorption lines are distorted by emission, making a quantitative spectral classification of V510 Pup difficult. Therefore, we compared the spectra with those of three supergiants with similar temperatures: HD 17378 (A5Ia), 89 Her (F2Ia), and α Per (F5Ib). Figure 1 presents fragments of the spectra of V510 Pup and 89 Her. The comparison confirms the similarity of these spectra noted by Slijkhuis *et al.* [13]. The main distinction is that the spectrum of V510 Pup displays strong absorption in the C_2 Swan molecular bands: Fig. 1 clearly shows the λ 5165 Å band, which is absent in the spectrum of 89 Her. Note also that the spectral type F5, which was derived by Slijkhuis *et al.* [13] from the ratio of the SrII and Hδ line intensities, may be inaccurate due to possible distortion of the Hδ profile by emission and the influence of the enhanced Sr abundance on W_{λ}(SrII). A Sr excess is probable given the detection by Slijkhuis *et al.* [13] of a substantial enhancement of lines of the other s-process element YII. We also underscore the enhancement of lines of s-process elements, primarily YII, in the spectrum of V510 Pup. In Fig. 1, this effect is illustrated by the YII λ 5200 Å line.

Bakker *et al.* [21] estimated the effective temperature $T_{eff} = 6900$ K for epoch 1992. They indicate that the effective temperature varies at a rate of about $\Delta T_{eff} = 70$ K/yr, so that we expect $T_{eff} \approx 7300$ K for the spectrum obtained in 1997.

The peculiarities of the optical spectrum of V510 Pup that distinguish it from the spectrum of an ordinary F5I supergiant are as follows. First, the neutral-hydrogen lines (in the available spectral interval, Hα and Hβ) display anomalous P Cygni profiles with a strong emission component (Fig. 2). Second, as we already noted, the spectrum of V510 Pup contains essentially no pure absorption features. Most metal-line profiles, including the D1,2 NaI doublet (Fig. 3) and infrared CaII triplet (Fig. 4),

Table 1. Spectral features of V510 Pup and the residual intensity r and radial velocity $V_{\odot}$ derived from various features (see text for details)

Identification	λ, Å	r	$V_{\odot}$, km/s	Identification	λ, Å	r	$V_{\odot}$, km/s
1	2	3	4	1	2	3	4
FeII(38), TiII(82)	4549.54	0.52:		YII(22)	4854.86	0.61	55
BaII(1)	4554.03	0.54:		Hβ	4861.33	0.62/1.90	59/108
FeII(37)	4555.89	0.54:		CrII(30)	4864.32	0.90:	49:
CrII(44)	4558.64	0.62:		TiII(29)	4865.61	0.90:/1.13	48:/79:
TiII(50)	4563.76	0.50:		FeI(318)	4871.32	0.95:/1.07	42:/75:
TiII(82)	4571.97	0.48:		FeI(318)	4872.14		
FeII(38)	4576.34	0.82:		TiII(114)	4874.02	0.82/1.04:	48:/84:
FeII(37)	4582.83	0.72:		CrII(30)	4876.40	0.80	47
FeII(38)	4583.84	0.60:	42:	FeI(318)	4878.21	0.98:/1.05:	–/77:
CrII(44)	4588.20	0.70:	42:	YII(22)	4883.68	0.53	58
TiII(50)	4589.94	0.71:	48:	CrII(30)	4884.60		
CrII(44)	4592.05	0.82:	44:	FeI(318)	4890.75		
CrII(44)	4616.62	0.82:	44:	FeI(318)	4891.49	0.96:/1.05:	44:/70:
CrII(44)	4618.82	0.76:	52:	FeII(36)	4893.81	0.92:/1.08:	50:/88:
FeII(38)	4620.51	0.85:	41:	YII(22)	4900.12	0.52	56
FeII(37)	4629.33	0.73:	40:	TiII(114)	4911.19	0.78	49
CrII(44)	4634.07	0.80:		FeI(318)	4918.99	0.94:/1.05:	50:/78:
FeII(186)	4635.31	0.90:		FeI(318)	4920.50		50:/75:
TiII(59)	4657.20	0.80:	44:	FeII(42)	4923.92	0.61/1.18	52/102:
FeII(37)	4666.75	0.90:	50:	BaII(1)	4934.08	0.60	55:
FeII(25)	4670.18	0.80:		FeI(318)	4957.30		
ScII(24)	4670.40			FeI(318)	4957.58	0.90/1.15	–/76
MgI(11)	4702.98	0.85:		SrI(4)	4962.28	0.98:/1.07	–/73
TiII(49)	4708.66	0.87:		FeII(36)	4993.35	0.92:/1.16:	43:/75:
TiII(59)	4719.51	0.90:		FeI(16)	4994.13	–/1.13:	
FeII(43)	4731.47	0.80:		TiII(71)	5005.16	0.90:	46:
TiII(92)	4779.98	0.76:	41:	TiII(113)	5010.21	0.82:	42:
NiI(98)	4786.54	0.85:		FeI(16)	5012.07	0.88:/1.10:	40:/73:
YII(22)	4686.58			TiII(71)	5013.69	0.81/1.04:	40/78:
TiII(17)	4798.53	0.79:	37:	FeII(42)	5018.44	0.60/1.21	53/95
TiII(92)	4805.09	0.66	54:	ScII(23)	5031.02	0.70/1.06:	49/100:
YII(22)	4823.31	0.68		FeI(16)	5041.07	0.92/1.08	45:/78:
CrII(30)	4824.14			FeI(36)	5041.75	–/1.12	–/77
CrII(30)	4836.24	0.87:	48:	FeI(318)	5044.21	1.10	75:
CrII(30)	4848.25	0.77:	39:	FeI(114)	5049.82	0.97:/1.12	44:/78:

Table 1. (Contd.)

1	2	3	4	1	2	3	4
FeI(16)	5051.63	−/1.15	−/75	FeI(36)	5194.94	0.93/1.10	48/75
FeI(383)	5068.76	0.90:		YII(28)	5196.43	0.85	53:
TiII(113)	5072.29	0.81	50	FeII(49)	5197.58	0.81/1.22	46:/80
FeI(66)	5079.22	0.96:/1.15:	45:/82:	FeI(66)	5198.71	−/1.20:	−/84
FeI(16)	5079.73	−/1.20:	−/81:	YII(20)	5200.41	0.75/1.09	53/90
FeI(16)	5083.34	0.98:/1.20	50:/70	FeI(66)	5202.33	−/1.21	−/78
YII(20)	5087.42	0.62/1.03:	56/95:	CrI(7)	5204.51	0.94:/1.04	46:/73
NdII(48)	5092.80	0.99:/1.07:	50:/75:	YII(20)	5205.73	0.63/1.12	55/90
FeII(205)	5093.49	−/1.10:	−/71:	CrI(7)	5208.43	0.95/1.04	
FeI(66)	5098.69	0.97:/1.12	44:/73	FeI(553)	5208.59		
FeII(35,185)	5100.70	−/1.15:	−/80:	TiI(4)	5210.38	0.97:/1.02:	−/74:
CrI(2)	5105.54	0.95:/1.07	35:/72	TiII(103)	5211.54	0.92/1.10	48/85:
FeI(16,36)	5107.60	0.96:/1.18	40:/72	NdII(44)	5212.37		
FeI(1)	5110.41	−/1.07:	−/84:	FeI(36)	5216.27	−/1.19	−/72
ZrII(95)	5112.27	0.85:/1.05:	49:/80:	TiII(70)	5226.54	0.62/−	51/−
YII(20)	5119.12	0.87:/1.05:	50:/74:	FeI(383)	5226.87		
YII(21)	5123.21	0.74	53	FeI(37)	5227.18	−/1.17	−/72
FeI(16)	5123.72	−/1.20	−/73	CrII(43)	5232.49		
FeI(16)	5127.36		38:/72:	FeI(383)	5232.94	0.88/1.06	−/76
TiII(86)	5129.16	0.78:/1.07:	43:/−	FeII(49)	5234.62	0.81/1.16	44/82
FeII(35)	5132.66	−/1.13:	−/73	CrII(43)	5237.32	0.83/1.04:	43/90:
FeII(35)	5136.79	0.95:/1.08:	40:/78	ScII(26)	5239.82	0.82/1.03:	51/81:
FeI(318)	5139.40	: 0.95:/1.20:	40:/80:	FeII(843)	5242.49	0.97:/1.04:	43:/75:
FeI(16)	5142.92	0.95:/1.20:	49:/84:	CrII(23)	5246.77	0.95:/1.02:	50:/78:
FeI(16)	5150.84	−/1.15:	−/80:	CrII(23)	5249.43	0.95/1.04	54:/80:
MgI(2)	5167.33	0.71	42:	NdII(75)	5249.58		
FeII(42)	5169.03	0.56/1.21	54/92	FeI(66)	5250.65	0.97/1.18	50/77
FeI(36)	5171.59	−/1.08:	−/75:	FeII(49)	5254.93	0.95/1.11	45/76
MgI(2)	5172.69	0.84/1.22	41/84	NdII(43)	5255.51	−/1.14	−/71
TiI(4)	5173.74	1.10	80:	FeII(41)	5256.93	0.96/1.10	45/84
MgI(2)	5183.61	0.71/1.19	38/84	PrII(35)	5259.73	1.12	73
TiII(86)	5185.90	0.75/1.05	52/88:	TiII(70)	5262.10	−/1.09	−/81:
TiII(70)	5188.68	0.61/1.09	52/92	FeII(48)	5264.80	0.93/1.13	46/80
NdII(45)	5191.45			CrI(18)	5265.72		
FeI(383)	5191.46	0.81/1.07:	55/85	FeI(383)	5266.55	−/1.20	−/74
FeI(383)	5192.35	−/1.14:	−/83	TiII(103)	5268.63	0.96:/1.06:	48:/65
NdII(75)	5192.60						

Table 1. (Contd.)

1	2	3	4	1	2	3	4
FeI(15)	5269.54	0.90/1.19	46/75	CrI(18)	5348.31	0.98/1.03	
FeI(37)	5270.36	–/1.22	–/72	ZrII(115)	5350.20:	0.94/1.10	46/80
FeII(185)	5272.39	–/1.05	–/77:	CeII(15)	5353.53	–/1.10	–/73
FeI(553)	5273.16	0.94:/1.08:		ScII(30)	5357.18	–/1.12:	–/66:
CrII(43)	5274.98			NdII(74)	5361.47	0.97:/1.04:	48:/72:
FeII(49)	5276.00	0.80/1.15	45:/85:	FeII(48)	5362.86	0.84/1.23	42/82
CrII(43)	5279.87	0.92:	48:	FeI(1146)	5364.87		
FeI(383)	5281.79	0.95:/1.04:	45:/77:	FeI(786)	5365.39	–/1.05:	–/68:
FeI(553)	5283.62	0.90/–	46/–	CrII(29)	5369.35	0.97/1.05:	36:/80:
FeII(41)	5284.10	–/1.20	–/78	FeI(1146)	5369.96	–/1.03:	
YII(20)	5289.82	0.96:/1.08:	45:/77:	FeI(15)	5371.49	0.92/1.23	40/77
NdII(75)	5293.16	1.08	73	TiII(69)	5381.02	0.83/1.25	49/82
CrI(18)	5298.27	0.98:/1.05	48:/71:	FeI(553)	5393.17	–/1.17	
FeI(553)	5302.30	1.14	68	CeII(24)	5393.38		
FeII(225)	5303.39	0.98:/1.08:	40:/77:	MnI(1)	5394.67	1.05:	75:
CrII(24)	5305.86	0.93/1.07	50/74	TiII(80)	5396.30	0.98:/1.07	42:/73
FeI(36)	5307.36	0.98/1.05	52:/76:	FeI(15)	5397.12	–/1.26	–/72
CrII(43)	5308.42	0.96:/1.04	52:/80:	YII(35)	5402.78	0.82	57
CrII(43)	5310.69			FeI(1145)	5404.13	–/1.02:	73:
HfII(37)	5311.63	0.98:/1.07	–/65:	FeI(15)	5405.77	0.96/1.23	45/75
CrII(43)	5313.58	0.92/1.03:	48:/76:	CrII(23)	5407.61	0.97/1.08	43/80
FeII(49,48)	5316.65	0.71/1.20	40/90	CrII(29)	5409.28		
NdII(75)	5319.82	0.97/1.05	48:/76:	CrI(18)	5409.78	0.96:/1.12	–/73:
YII(20)	5320.78	0.97:/1.06	56:/77:	CrII(29)	5410.39		
FeI(553)	5324.18	0.92/1.05	48/73	FeII(48)	5414.07	0.97/1.09	–/75
FeII(49)	5325.55	0.91/1.11	46/77	FeI(1165)	5415.20		
FeI(15)	5328.04	0.90/1.25	45/78	TiII(69)	5418.79	0.91/1.14	52/75
FeI(37)	5328.53			CrII(23)	5420.93	0.98/1.08	40:/78
FeI(35)	5332.90	0.97/1.07		TiII(80)	5422.47	–/1.10	–/86
CrII(43)	5334.86	0.90/1.03	50:/80:	FeII(49)	5425.25	–/1.17	–/77
TiII(69)	5336.79	0.78/1.15	47/84:	FeII	5427.80	1.05	67:
FeII(48)	5337.73	–/1.10	–/73	FeI(15)	5429.70	0.95/1.28	47/75
FeI(553)	5339.93	0.98:/1.03:	35:/80:	NdII(80)	5431.58	–/1.07	–/74
FeI(37)	5341.02	0.95/1.08	46/72	FeII(55)	5432.98	0.98:/1.11	37:/76
CrI(18)	5345.80	0.97/1.08	42/80:	FeI(15)	5434.52	0.96/1.16	42/73
CrII(24)	5346.07			FeI(15)	5446.91	0.97:/1.24	45:/73
CrII(23)	5346.54			TiII(68)	5454.05	–/1.05:	–/76:

Table 1. (Contd.)

1	2	3	4
FeI(15)	5455.61	0.95:/1.28	40:/73
YII(12)	5466.46	0.97:/1.05:	46:/76:
CeII(24)	5472.30	0.98:/1.07:	40:/78:
NiI(59)	5476.91	0.97:/1.16	−/72
CrII(50)	5478.37	−/1.06	
YII(27)	5480.75	0.91/1.02:	48/78:
CoI(39)	5483.35	−/1.15	−/74
NdII(79)	5485.70	−/1.08:	−/75:
TiII(68)	5490.68	−/1.10:	−/77:
TiII(68)	5492.82	0.97/1.10	42:/77
YII(27)	5497.42	0.80/−	53/−
FeI(15)	5497.51	−/1.10	
FeI(15)	5501.46	0.96/1.11	46:/74
CrII(50)	5502.08		
CrII(50)	5503.22		
FeI(15)	5506.78	−/1.12	−/74
YII(19)	5509.90	0.85/1.12	55/80
CeII(24)	5512.04	0.97:/1.08	47:/83
TiII(106)	5514.50:	1.09	73:
YII(27)	5521.56	0.95:/1.05	52/77
FeII(56)	5525.11	0.97:/1.03:	40:/70
ScII(31)	5526.81	0.68/1.08	50/90
MgI(9)	5528.40		
FeII(55)	5534.84	0.87/1.17	47/81
YII(27)	5544.61	0.92/−	57/−
YII(27)	5546.00	0.96:/1.05:	54:/80:
ScII(25)	5552.22	0.97:/1.03:	−/77:
FeI(686)	5569.62	−/1.06:	−/77:
FeI(686)	5572.84	−/1.08:	−/72:
FeI(686)	5586.75	−/1.08:	−/78:
NiI(70)	5587.86	−/1.08:	−/75
NiI(69)	5592.26	−/1.13	−/78:
CaI(21)	5594.46	−/1.04:	−/79:
CaI(21)	5598.48	−/1.05	
YII(19)	5610.36	1.08	75
FeI(686)	5615.64	1.13	70
FeI(686)	5624.54	1.08:	74:
FeII(57)	5627.49	1.08:	
ScII(29)	5640.98	0.87/1.06:	49/82:
ScII(29)	5657.87	0.77/−	51/−
ScII(29)	5658.34		
FeI(686)	5658.82	−/1.08	
YII(38)	5662.95	0.69/1.08	51/92
ScII(29)	5667.15	0.95/1.08	47/−
ScII(29)	5669.03	0.93/1.14	49/75
ScI(12)	5671.82	1.05:	73:
NaI(6)	5682.64		
ScII(29)	5684.19	0.86/1.04	45:/79
ScI(12)	5686.83	1.04:	76:
NdII(79)	5688.53		72:
SiI(10)	5708.40	−/1.03:	−/73:
FeI(686),NiI(46)	5709.50	0.97/1.17	44:/76:
FeI(1087)	5711.88	1.15	74
NiI(231)	5715.09	1.05:	80:
YII(34)	5728.91	0.95/1.07	49/76
NiI(68)	5754.66	−/1.05	−/76
CeII(32)	5768.90	−/1.12	−/84:
NdII(79)	5804.02	1.07	75
BaII(2)	5853.68	0.96/1.07	48/74
NaI(1)	5889.95	0.03/1.32	42/92
NaI(1)	5895.92	0.06/1.28	42/92
FeI(552)	5909.97	−/1.08	−/77
FeII(46)	5991.37	−/1.36	−/77
	Nov. 23, 1997	PFES	
FeI(207)	6065.49	−/1.11	−/67:
FeII(46)	6084.10	0.98/1.13	−/73
ZrII(93)	6100.04	−/1.09	−/77
CaI(3)	6102.73	0.96	38:
ZrII(106,137)	6106.47	0.99:/1.08	29:/70
NiI(45)	6108.12	1.14	74
FeII(46)	6113.32	0.98:/1.06	−/73
ZrII(93)	6114.78	1.12	74
CaI(3)	6122.22	0.96	
TiII(69)	6126.22	1.05	72

Table 1. (Contd.)

1	2	3	4	1	2	3	4
FeII(46)	6129.67	–/1.10	–/67	LaII(33)	6390.48	1.07	63
FeI(169)	6136.62	0.96/1.08	30:/75:	FeI(168)	6393.61	1.18	64
FeI(207)	6137.69		68:	FeI(816)	6400.00	1.22	
BaII(2)	6141.72	0.73/1.12	43/86	FeI(13)	6400.32		
FeII(74)	6147.74	0.93/1.13	28:/72	FeII(74)	6407.25		
FeII(74)	6149.24	–/1.20	–/80:	FeI(816)	6408.02	1.04	
FeII(163)	6179.38	–/1.03	–/86	FeII(74)	6416.93	0.94/1.15	20/71
NiI(45)	6191.18			FeI(111)	6421.35	0.98/1.09	17/67:
FeI(169)	6191.56	1.29		FeI(62)	6430.85	0.98/1.14	20:/69
FeI(62)	6213.43	1.05	67	FeII(40)	6432.69	1.30	70
ZnII(1)	6214.58			FeII(199)	6446.40	1.02	70:
FeI(62)	6219.28	1.08	77	FeII(74)	6456.38	0.85/1.20	23/80
FeI(207)	6230.73	1.14	68	FeI(168)	6462.72	1.04	72
FeII(74)	6238.39	0.92/1.12:	18/78:	TiII(91)	6491.57	0.94/1.09	21/59:
FeII(74)	6239.94			FeI(168)	6494.99	0.97/1.07	16:/72:
ScII(28)	6245.62	0.87	34	BaII(2)	6496.90	0.72	36:
FeI(816)	6246.32			FeI(13)	6498.94	1.13	
FeII(74)	6247.55	0.93/1.18	26/81	FeII(40)	6516.08	0.91/1.33	20:/72
FeI(169)	6252.56	0.98:/1.10	22:/71	FeI(268)	6546.25	1.14	61
FeI(111)	6254.26	1.03	68:	Hα	6562.81	0.76/3.10	26/108
FeI(169)	6256.36	0.98/1.05:	30:/71	FeI(268)	6592.92	0.99/1.09:	–/67
TiI(104)	6258.50	0.97/1.03	25:/80:	FeI(168)	6593.87	1.06:	64:
TiI(104)	6261.10	0.98:/1.02	33:/65	ScII(19)	6604.59	0.94:/1.12:	25/72
LaII(33)	6262.30	1.04	72	TiII(91)	6606.95	1.05	67
FeI(62)	6265.14	0.98:/1.04:	–/72	FeI(206)	6609.12	–/1.03	–/68
FeI(342)	6270.23	0.93:/1.06:	16:/63:	YII(26)	6613.74	0.88:/1.01:	35/–
[OI] 1F	6300.30	1.18	72	NiI(43)	6643.64	0.99/1.10	20:/68
NiI(67)	6314.67	1.05:	65:	Eu(8)	6645.11	1.06	63:
FeI(168)	6318.02	1.05:	68	FeI(268)	6677.99	–/1.18	–/60:
FeI(62)	6335.33	1.10:	63:	CaI(32)	6717.68	0.99/1.06	
SiII(2)	6347.10	0.85	18	TiII(112)	6717.91		
FeI(342)	6355.03	1.02:	62:	TiI(48)	6743.12	0.98/1.05	19:/65
FeI(13)	6358.69	1.10:	64:	FeI(111)	6750.16	1.04	60:
[OI]1F	6363.78	1.07	65	NiI(57)	6767.78	1.09	65
FeII(40)	6369.46	–/1.10	–/64	YII(26)	6795.42	0.97/1.04	30:/73:
SiII(2)	6371.36	0.88:		FeI(111)	6978.86	1.03	65:
NdII(85)	6385.20	1.05	65	TiII(101)	7214.73	1.07:	57:

Table 1. (Contd.)

1	2	3	4
FeII(73)	7224.48	1.12:	67
[CaII]1F	7291.46	1.40	66
FeII(73)	7320.70		
[CaII]1F	7323.88	1.50	70
NiI(84)	7385.25	1.07:	58:
MgI(30)	7387.69	1.04:	60:
FeII(73)	7449.33	0.97:/1.12	–/62:
YII(25)	7450.32		
FeII(73)	7462.39	0.98:/1.22	14:/68
FeII(72)	7479.70	1.10:	64
FeI(1077)	7511.03	0.98/1.04	15:/71
FeII(73)	7515.83	0.99:/1.14	17:/68:
FeI(402)	7583.79	0.98/1.06	16:/65:
KI(1)	7698.97	0.49/1.09	24/82
FeII(73)	7711.72	–/1.28	–/65
NiI(62)	7714.32	1.09:	65:
FeI(402)	7748.28	1.12	65
FeII(72)	7841.37	1.05	67:
FeI(12)	7912.87	1.12:	62:
FeI(12)	8075.16	1.08:	72:
P22	8359.00		20:
P21	8374.48	0.75:	15:
FeI(60)	8387.77	1.25:	65
P20	8392.40	0.78	18:
TiI(33)	8412.37		
P19	8413.32	0.75	15:
TiI(33)	8434.97		
TiI(33)	8435.66	0.80:	20:
P18	8437.96	0.74	
OI(4)	8446.40	0.63/–	25:/–
P17	8467.25	0.79	
FeI(60)	8468.41	1.12	66:
CaII(2)	8498.04	0.36/1.80	32/93
P16	8502.48		
FeI(60)	8514.08	1.17	67:
CaII(2)	8542.12	0.24/2.00	33/102
P15	8545.38		

contain both absorption and emission components. Low-excitation CaI, NiI, FeI, and ScII lines are seen in emission. The presence of broad emission components in the lines of the sodium doublet suggests we should include V510 Pup—the optical component of IRAS 08005—in the small group of post-AGB stars with this spectral peculiarity [22], inherent to R CrB stars. In particular, broad emission lines have been detected [22] in the spectrum of QY Sge, associated with IRAS 20056+1834.

While there are considerable similarities, the spectra of QY Sge and V510 Pup also display substantial differences, apparently due to differences in their circumstellar structure. First, the spectrum of QY Sge displays extremely intense D NaI emission, appreciably exceeding the continuum level. Second, spectropolarimetric observations of [11] show that the degree of polarization in the region of the sodium doublet in the spectrum of QY Sge decreases to the interstellar level; in the transition from the energy distribution to the distribution of the degree of polarization, emission turns into absorption. This inversion indicates that the NaI emission in QY Sge is formed in the dust envelope, which polarizes the photospheric radiation. No such inversion in the NaI lines is seen in V510 Pup, at least in low-resolution polarization spectra [11]. It is concluded in [11] that the Balmer emission lines in the spectrum of V510 Pup form close to the star due to scattering on the dust component. Since the velocities for V510 Pup derived from the NaI emission lines and hydrogen lines coincide (Table 2), this conclusion is also valid for the NaI emission. High-resolution spectropolarimetric observations of both objects are needed to draw firmer conclusions. When testing the prime-focus spectropolarimeter of the 6-m telescope [25], R CrB was observed in a state close to minimum brightness with a resolution of $R = 15\,000$. In Fig. 9 from [25], both the broad and narrow components of the NaI resonance doublet disappear in the wavelength distribution of the degree of polarization, while the degree of polarization ((1.5–2)%) in the region of the doublet remains the same as in the other parts of the spectrum. Thus, the spectropolarimetric characteristics of V510 Pup are closer to those of R CrB than to those of QY Sge.

Both of the main distinguishing features of the spectrum of V510 Pup were first detected in 1989

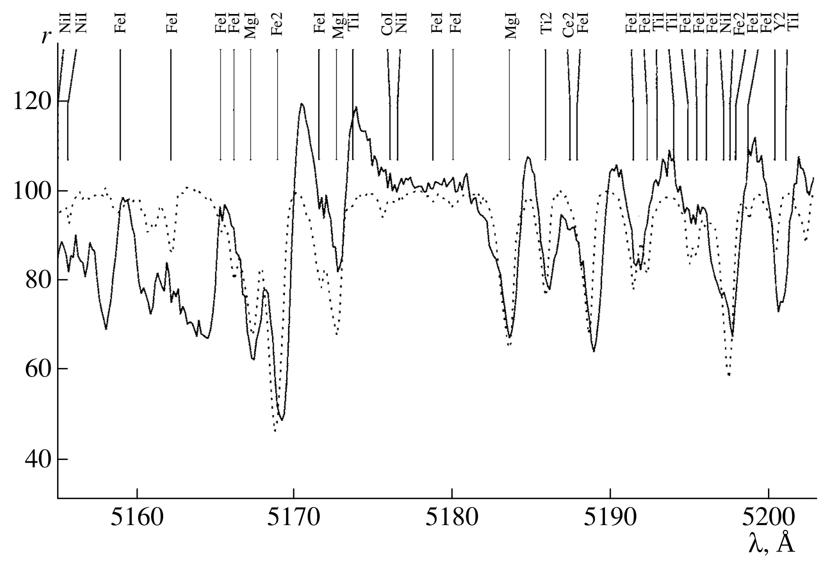

Fig. 1. Comparison of fragments of the spectra of V510 Pup (solid) and 89 Her (dotted) in the wavelength interval containing the YII λ 5200 Å line and the head of the C_2 λ 5165 Å Swan molecular band. For ease of viewing, the spectra are slightly shifted in wavelength relative to one another. Here and in the subsequent figures, the adopted continuum level is 100.

in observations with low spectral resolution [13]. A comparison of the Hα profile presented in [13] with our data for November 1997 shows that the profile had changed: even taking into account the difference in spectral resolution, it is obvious that the absorption component became stronger, with its core extending below the continuum level. In 1990, however, Zijlstra (private communication in [13]) observed the same kind of difference from the data by Slijkhuis *et al.* [13]. The Hα line is formed in upper layers of the extended atmosphere of the star. Its broad emission wings probably originate due to scattering on free electrons. The absorption features result from absorption in front of the star; they indicate the velocity $V_\odot =$ 26 km/s, which differs from the systemic velocity by -35 km/s, providing evidence for expansion of the region where this absorption feature is formed.

In high-resolution spectra, the absorption cores of the NaI doublet (Fig. 3) break up into several absorption components with velocities of $V_\odot = 9$, 38, and 51 km/s. The components with $V_\odot = 9$ and 51 km/s are interstellar, while the component with $V_\odot = 38$ km/s is formed in the stellar atmosphere. Interstellar lines are observed in the Galaxy in the general direction of V510 Pup, whose positions correspond to velocities of $V_\odot = 10$–45 km/s [24]. Both lines of the NaI doublet also display emission components that clearly exceed the continuum level (Fig. 3). The position of the emission components in the spectrum leads to $V_\odot \approx 100$ km/s, which is close to the velocity derived from the emission component of the Hα profile (Table 2). These emission lines originate in the extended gaseous circumstellar envelope.

Note also that we see none of the doubling of the metal lines described by Bakker *et al.* [21] in our spectra, even in the spectrum obtained in 2002 with a resolution of $R = 60\,000$. In this connection, Slijkhuis *et al.* [13] also note that, in contrast to ρCas, neither doubling of the low-excitation absorption lines nor a clear correlation between the shift of an absorption line and its excitation potential are observed in the spectrum of V510 Pup. However, we do not confirm the tendency noted in [13] for the velocity derived from the lines to be more negative at shorter

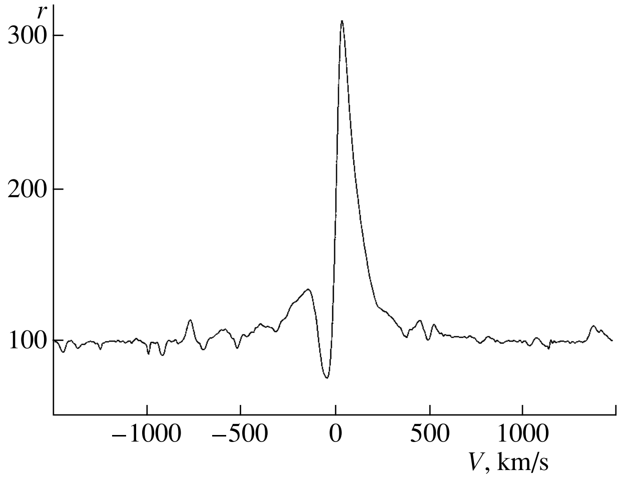

Fig. 2. Hα profiles in the spectrum of V510 Pup. Telluric features have not been removed.

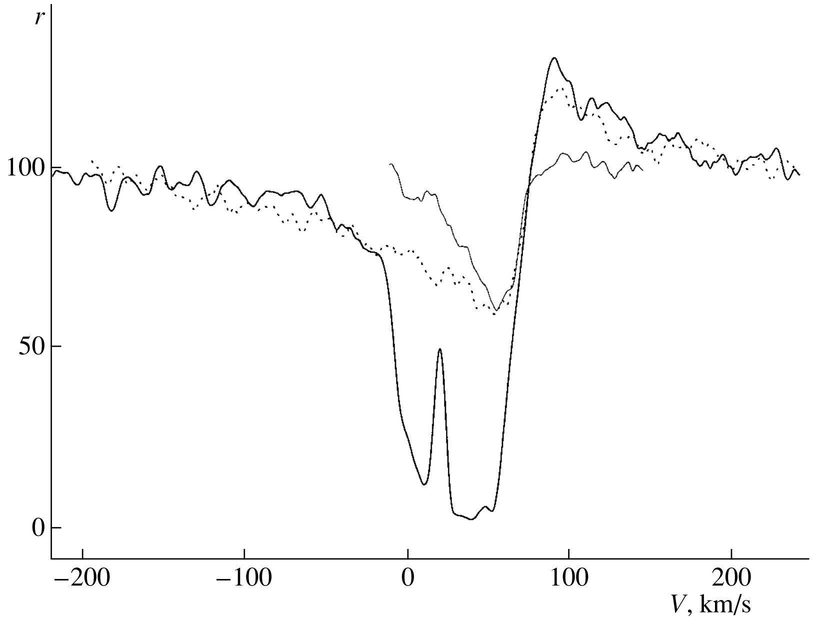

Fig. 3. Profiles of selected lines in the spectrum of V510 Pup. The thick solid profile shows the D1 NaI λ 5889 Å line; the thin solid profile, the YII λ 5087 Å line; and the dotted profile, the FeII λ 5018 Å line.

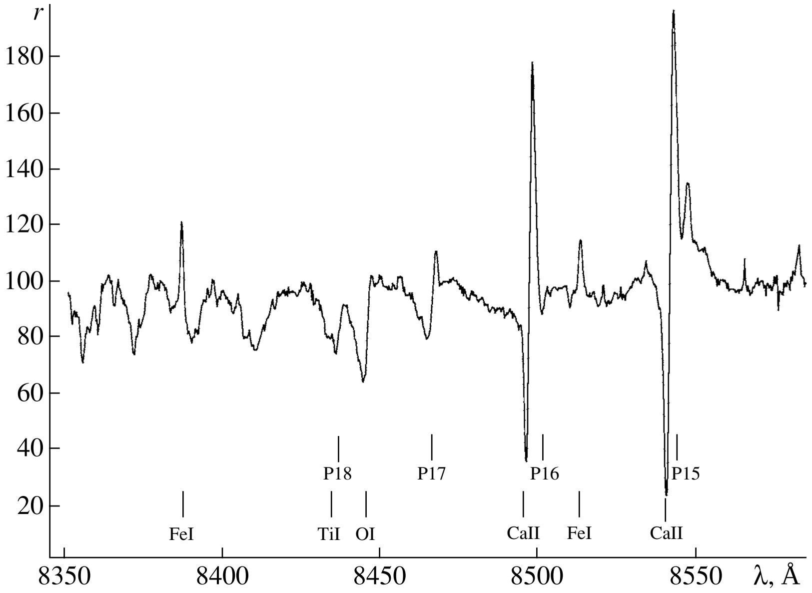

Fig. 4. Fragment of the spectrum of V510 Pup in the wavelength interval containing the CaII and Paschen lines.

wavelengths. Table 2 shows the opposite trend: absorption lines with $\lambda < 6000$ Å display more positive velocities than lines with $\lambda > 6000$ Å. Modeling of radiation transfer in an expanding dust envelope [26] indicates that, in addition to the general redward shift of the absorption lines, scattering on dust particles can also result in a second-order effect: a decrease of the redward shift with increasing wavelength.

The spectrum of V510 Pup in Fig. 1 clearly displays an intense C_2 λ 5165 Å Swan molecular absorption band. Molecular bands of C_2 (and, possibly, C_3) were first detected in the spectrum of this star by Hrivnak [27] in moderate-resolution optical spectra. All the F–G supergiants studied by Hrivnak [27] are candidate PPNs with carbon-enriched envelopes; their spectra contain molecular bands of C_2 and C_3, as well as enhanced lines of heavy metals. It is important that the C_2 molecular bands indicate a carbon excess in the extended atmosphere of V510 Pup, while the radio observations of [23] indicate that the object's envelope (containing previously lost matter) is not carbon-enriched. The bipolar PPN AFGL 2688 displays the opposite pattern: after being a carbon star in the AGB stage, it turned into an F supergiant with enhanced nitrogen and oxygen abundances in the post-AGB stage [12].

Unfortunately, the available observational data do not permit the measurement of diffuse interstellar bands. In the 1997 spectrum, these bands are blended with metal lines. This is also true of the λ 6613 Å band, which is usually the least blended but is blended by a strong YII line in the spectrum of V510 Pup. In the high-resolution spectrum obtained in 2002, spectral intervals containing the strongest diffuse interstellar bands were beyond the echelle frame.

3.2. Radial Velocities

Table 1 presents identifications of lines in the spectrum of V510 Pup, the measured residual intensities r, and the heliocentric radial velocities $V_\odot$ for the absorption cores and emission peaks of lines. In total, about 400 lines are identified at $\lambda\lambda$ 4540–8550 Å; more than half display pronounced P Cygni profiles. The r and $V_\odot$ values for the absorption and emission components of such profiles are separated by a slash. Table 1 presents the data at $\lambda < 6000$ Å obtained on November 19, 2002, with the NES spectrograph; the data at longer wavelengths was obtained on November 23, 1997, with the PFES spectrograph. The line identifications and measurements of the spectrum of V510 Pup are complicated by the presence of numerous molecular lines, both telluric (O_2 and H_2O) and circumstellar (C_2, CN, and others); Table 1 does not contain these lines.

The circumstellar envelope of a supergiant is manifest in the optical spectrum, in particular, by the shapes of molecular bands of C_2 and CN. Bakker *et al.* [21] studied the molecular component of the spectrum of V510 Pup based on high-resolution spectra. They used the absorption lines of the C_2 Swan molecular band and the CN red-system band to derive the radial velocities $V_\odot = 17.4$ and 22.3 km/s, which yield an average expansion velocity for the molecular envelope of roughly $V_{exp} = 43$ km/s. Our value $V_\odot = 19.1$ km/s derived from absorption lines of the C_2 Swan molecular band is in good agreement with the data of [21]. Note also that the velocities measured from the C_2 Swan molecular band and the SiII λ 6347 Å line, which is one of the few "pure" absorption lines undistorted by emission, coincide. The velocity derived from the FeII(42) absorption components is also close to this value.

Table 2. Average heliocentric radial velocities for groups of lines and some individual lines (the last column presents previously published measurements)

Wavelength interval, Å Individual line	$V_\odot$, km/s		
	November 23, 1997	November 19, 2002	Data of other authors
Groups of lines			
$r \to 1$			
Emission lines and components			
$\lambda < 6000$	73 ± 3	72 ± 2	
$\lambda > 6000$	65 ± 2		61 [13]
Absorption lines and components			
$\lambda < 6000$	37 ± 3	46 ± 2	38 [13]
$\lambda > 6000$	23 ± 3		
$r \approx 0.6$			
Emission components			
$\lambda < 6000$	115:	95 ± 3	
Absorption components			
$\lambda < 6000$	48 ± 3	55 ± 3	
FeII(42)	30/110	52/95	
Individual lines			
Hα	26/108		
Hβ	28/130	59/108	
NaI(1)	33:/108	42/92	
C_2		19 ± 1	17.4 [21]
OH			61.1 [23]
NaI (interstellar)	11:	10, 51	10–45 [24]

Table 2 presents general data on the radial velocities. It contains the average $V_\odot$ derived from both of our spectra for several groups of lines or components of their P Cygni profiles and also for the Hα, Hβ, and NaI individual lines and the C_2 band. For comparison, the last column presents radial velocities from the literature (in the lowest line of Table 2, they refer to stars located no more than to 10° from V510 Pup rather than to the object itself). It is clear that our estimates are consistent with those obtained by other authors. Figure 5 presents general data on the radial velocities in graphical form. The variations for both emission and absorption components are plotted as a function of the residual intensity of the absorption components (Fig. 5 cannot be used to judge the

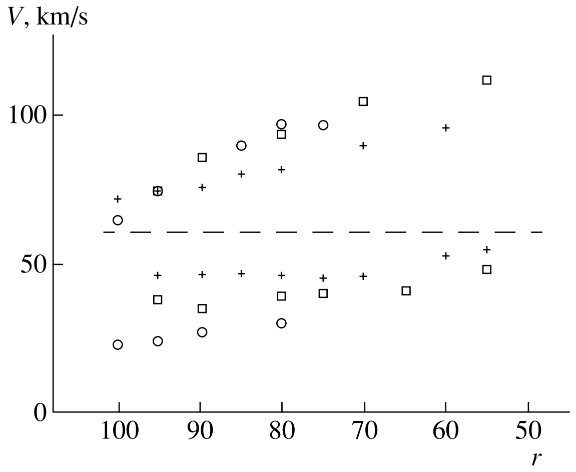

Fig. 5. Radial velocity as a function of residual intensity r of an absorption line or component in the spectra of V510 Pup obtained on November 23, 1997 (the squares shows the data for $\lambda < 6000$ Å, and the circles, data for $\lambda > 6000$ Å), and November 19, 2002 (crosses). Each symbol corresponds to the average $V_\odot$ for several lines. The error in the mean velocity is $\sigma_V \approx 2$ km/s for the NES spectrometer and 4 km/s for the PFES spectrometer. The dashed straight line indicates the level $V_{sys} = 61$ km/s; emission lines and emission components with P Cygni profiles lie above, while absorption lines and components lie below.

intensity of emission features; pure emission corresponds to $r = 1$ (100 in Fig. 5)).

We can see in Table 2 and Fig. 5 that the differences between the velocities reach 100 km/s within a single spectrum, primarily due to shifts of emission and absorption components relative to each other but also as a result of systematic variations of the velocity as a function of the intensity and wavelength of the lines. The large differential shifts of the lines and their components provide clear evidence for a velocity gradient in the layers of the atmosphere of V510 Pup where these lines originate, while the numerous P Cygni profiles indicate expansion of the atmosphere. However, to analyze the obtained set of velocities, we must introduce a zero point—the velocity of the center of mass of the star (the systemic velocity V_{sys}). We used $V_{sys} = +61$ km/s—the average heliocentric velocity of the group of OH masers surrounding the star [23]. In Fig. 5, V_{sys} is marked by the horizontal dashed line. Let us now compare the deviations from V_{sys} for velocities derived from some spectral features with the geometrical and kinematic features of the envelope of V510 Pup noted above.

Assuming that the emission lines originate in the periphery of the gaseous spheroid or torus that gives rise to the bipolar outflow [6, 10], the velocities derived from these lines should not deviate significantly from V_{sys}. Indeed, the minimum deviations are seen for the emission-line velocities, particularly those for lines at long wavelengths. There are few pure emission lines in the spectrum of V510 Pup, since their profiles generally display dips in the blue wings (the absorption components of P Cygni profiles); as a result, the peak of the profile is shifted toward the red. Therefore, we are dealing with the limit to which $V_\odot$ tends as it decreases with the decay of the absorption component. The symbols corresponding to emission lines in Fig. 5 approach V_{sys} as r increases but remain higher than this even for $r = 1$ (100 in Fig. 5).

On the contrary, of all the symbols in Fig. 5 lying below V_{sys} and representing absorption-line velocities, the closest to V_{sys} are those corresponding to the deepest ($r \approx 0.5$–0.6) lines—YII, FeII, and others. Less deep absorption lines yield smaller $V_\odot$; i.e., they indicate higher expansion velocities. The minimum radial velocity (19 km/s) was derived from the C_2 molecular lines. Its deviation from V_{sys} is close to the maximum expansion velocity determined from the OH maser radiation.

This pattern is consistent with the presence of a powerful stellar wind in V510 Pup. Recall that the radial velocities were measured using the absorption cores and emission peaks of P Cygni profiles, which are associated with winds. Moreover, the specific shape of the profiles of strong lines appears to reflect a lack of spherical symmetry of the wind. Compare, for example, the profiles of the YII(20) λ 5087 Å and FeII(42) λ 5018 Å lines in the spectrum obtained on November 19, 2002 (Fig. 3). The enhancement of the emission in the latter line compared to the former line is not accompanied by a deepening of the absorption core and a shift of the core toward the blue (which is expected if the wind is spherically symmetric); the blue wing of the absorption, however, becomes flatter and more extended. The absorption component of the FeII(42) λ 5018 Å line can be followed to $V_\odot = -180$ km/s, which corresponds to the expansion velocity $V_{exp} = 240$ km/s, whereas the same velocity estimated from the red limit of the emission yields only $V_{exp} = 140$ km/s. It is also possible that, in addition to the axial symmetry and bipolar expansion of the envelope, the profile shape is affected by the presence of dust. The effect of dust is clearly illustrated by the HST image presented by Ueta *et al.* [10]. The circumstellar dust weakens the optical radiation from different parts of the axisymmetrical envelope of V510 Pup to different degrees: we primarily detect the radiation from the frontal part, which is moving toward us. In addition, a substantial fraction of this radiation is seen after it is scattered on dust that is also taking part in the expansion of the envelope. Since the outflow of the scattering material occurs at some angle to the line of sight, the scattered radiation should be redshifted, and the addition of the scattered radiation to the direct radiation of the object may distort the observed profile.

The above estimate for the highest velocity of the wind in V510 Pup can be derived from both FeII(42) and other strong lines. In the spectrum obtained on November 19, 2002, these include Hβ and the NaI(1) doublet. As we can see in Fig. 3, the upper parts of the profiles of FeII λ 5018 Å and NaI λ 5889 Å are similar: the blue wings of the absorption and emission components have roughly the same extents and intensities. However, the lower parts of the profiles differ dramatically—the core of the NaI absorption component is much deeper than the absorption core of the FeII line. The deepenings at radial velocities of -5 to $+20$ km/s and $+25$ to $+60$ km/s are particularly strong. Both can be either interstellar or circumstellar in origin; the interstellar component dominates in the former case, although its contribution in the latter case may also be substantial.

Note also that the high resolution of the November 19, 2002, spectrum enables us to see weak and narrow dips with velocities of -2, $+6$, $+12$, $+31$, $+40$, and $+54$ km/s recurring in the cores of both lines of the NaI doublet. The last three velocities also correspond to the deepenings in the cores of the FeII(42) lines. What is the origin of these dips? How stable are they—in particular, do their positions vary like those of the wind absorption components, or are they stationary like the circumstellar molecular lines? Which of them are interstellar? Subsequent spectral observations of V510 Pup should answer these questions.

3.3. Distance and Luminosity

It is unlikely that IRAS 08005 is closer to the Earth than 3–4 kpc. This is demonstrated by variations of the interstellar absorption along the line of sight. According to Neckel and Klare [28], interstellar space is fairly transparent in the direction toward IRAS 08005 ($l = 242°$, $b = 3.6°$), at least to a distance of 2 kpc, when the interstellar absorption A_v jumps to 2^m from 0.3–0.5. The standard estimate for A_v for V510 Pup is substantially higher: $A_v = 3.7–4.0^m$. Naturally, some fraction of this absorption may be circumstellar. According to Dame *et al.* [29], the CO radio emission is appreciably weakened in the interval $230° < l < 250°$ (which corresponds to the space between Cygnus–Orion and Perseus arms) and is observed in two nonoverlapping intervals $V_\odot = 25–45$ and 65–85 km/s. Note also that, according to [30], the radial velocities for stars in the direction of V510 Pup are $V_\odot = 10–75$ km/s. Since the velocity increases with distance in this direction in the Galaxy, the interval $V_\odot = 25–45$ km/s refers to a less distant layer of molecular clouds, while the second, $V_\odot = 65–85$ km/s, corresponds to a more distant layer; V510 Pup may be close to the latter both kinematically and spatially. The kinematic distance estimated using the diagram of Brand and Blitz [31] for $V_\odot = 61$ km/s ($V_{lsr} = 47$ km/s) and $l = 242°$ is $d = 4.0$ kpc, which corresponds to the absolute magnitude $M_v = -5.3^m$. Unfortunately, the spectral interval containing the OI(1) 7773 Å triplet, which serves as a good luminosity indicator for A–F stars, falls outside our November 23, 1997, spectrum. However, our estimate of the equivalent width of the triplet based on Fig. 1 of [21] and using Ferro and Mendoza's calibration [32], $W = 1.8$ Å, yields $M_v = -6.5^m$. Thus, both estimates suggest V510 Pup should be classified as an Ib–Iab supergiant.

4. CONCLUSIONS

The post-AGB star V510 Pup, which is associated with the infrared source IRAS 08005–2356, has been observed with high spectral resolution for the first time. In total, about 400 lines were identified in the wavelength interval 4540–8550 Å, including absorption lines of the ions FeII, TiII, CrII, and YII. More than half of the lines display distinct P Cygni profiles. Compared with supergiants with similar parameters, the spectra display anomalously strong absorption lines of YII and other s-process elements. One distinguishing feature of the spectrum is the presence of circumstellar C_2 Swan absorption bands.

Most hydrogen and metal lines display P Cygni absorption–emission profiles. We detected a large velocity gradient in the atmosphere: $\Delta V_r \approx 100$ km/s. All absorption components are shifted toward the blue, indicating an outflow of stellar material. We have used the Swan bands, which are formed in the envelope, to determine the expansion velocity of the envelope, $V_{exp} = 42$ km/s. The highest wind velocity measured from the absorption wings of the FeII(42) P Cygni profiles reaches 240 km/s. The mass-loss pattern provides evidence for deviations from spherical symmetry. The available observational data do not enable us to draw firm conclusions about the behavior of the radial-velocity pattern as a function of time. Tentatively, from the comparison of our results with the data obtained by Slijkhuis *et al.* [13], we find no substantial temporal variations of the velocity measured using the absorption and emission components of weak lines forming in the stellar photosphere.

A comparison of our data and the data of [21] suggests that the expansion velocity determined from the C_2 Swan molecular bands is constant.

Based on the kinematic parameters and interstellar absorption, we have determined the distance to V510 Pup to be $d \approx 4$ kpc, which corresponds to an absolute magnitude of $M_v \approx -6^m$.

ACKNOWLEDGMENTS

The authors thank V.E. Panchuk for useful discussions and M.V. Yushkin for his assistance in the observations and preprocessing of the spectral data. This work was supported by the Russian Foundation for Basic Research (project codes 02-02-16085 and 02-07-90245) and the State Science and Technology Project "Astronomy." The study was also supported by CRDF grant № RP1-2264.

REFERENCES

1. K. V. K. Iyenger and M. Parthasathy, Astron. Astrophys., Suppl. Ser. **121**, 45 (1997).
2. P. García-Lario, A. Manchado, and S. R. Pottash, Astron. Astrophys., Suppl. Ser. **82**, 497 (1990).
3. S. R. Van der Veen and H. J. Habing, Astron. Astrophys. **194**, 125 (1998).
4. V. G. Klochkova, V. E. Panchuk, and N. S. Tavolzhskaya, Pis'ma Astron. Zh. **28**, 49 (2002) [Astron. Lett. **28**, 49 (2002)].
5. L. Likkel, Astrophys. J. **344**, 350 (1989).
6. A. A. Zijlstra, J. M. Chapman, P. L. Hekkert, *et al.*, Mon. Not. R. Astron. Soc. **322**, 280 (2001).
7. L. Likkel, T. Forveille, A. Omont, and M. Morris, Astron. Astrophys. **246**, 153 (1991).
8. L.-Å. Nyman, P. J. Hall, and H. Olofsson, Astron. Astrophys., Suppl. Ser. **127**, 185 (1998).
9. B. M. Lewis, Astrophys. J. **338**, 234 (1989).
10. T. Ueta and M. Meixner, Astrophys. J. **528**, 861 (2000).
11. S. Trammell, H. L. Dinerstein, and R. W. Goodrich, Astron. J. **108**, 984 (1994).
12. V. G. Klochkova, V. E. Panchuk, and M. V. Yushkin, Astron. Rep. **48**, 288 (2004).
13. S. Slijkhuis, T. de Jong, and J. Y. Hu, Astron. Astrophys. **248**, 547 (1991).
14. V. E. Panchuk, I. D. Najdenov, V. G. Klochkova, *et al.*, Bull. Spec. Astrophys. Observ. **44**, 127 (1998).
15. V. E. Panchuk, N. E. Piskunov, V. G. Klochkova, *et al.*, Preprint No. 169, SAO (Special Astrophysical Observatory, 2002).
16. V. E. Panchuk, M. V. Yushkin, and I. D. Najdenov, Preprint No. 179, SAO (Special Astrophysical Observatory, 2003).
17. G. A. Galazutdinov, Preprint No. 92, SAO (Special Astrophysical Observatory, 1992).
18. A. K. Pierce and J. B. Breckinridge, Contrib. Kitt Peak Nat. Obs., No. 559 (1973).
19. S. Johansson, Phys. Scripta **18**, 78 (1978).
20. A. R. Striganov and G. A. Odintsova, *Tables of Spectral Lines of Atoms and Ions* (Énergoizdat, Moscow, 1982) [in Russian].
21. E. J. Bakker, E. F. van Dishoeck, L. B. F. M. Waters, and T. Schoenmaker, Astron. Astrophys. **323**, 469 (1997).
22. N. Rao Kameswara, A. Goswami, and D. L. Lambert, Mon. Not. R. Astron. Soc. **334**, 129 (2002).
23. P. Te Lintel Hekkert, J. L. Caswell, H. J. Habing, *et al.*, Astron. Astrophys., Suppl. Ser. **90**, 327 (1991).
24. L. M. Hobbs, Astrophys. J. Suppl. Ser. **38**, 129 (1978).
25. V. E. Panchuk, V. G. Klochkova, M. V. Yushkin, *et al.*, Preprint No. 159, SAO (Special Astrophysical Observatory, 2001).
26. J. D. Fix, Astrophys. J. **248**, 542 (1981).
27. B. Hrivnak, Astrophys. J. **438**, 341 (1995).
28. Th. Neckel and G. Klare, Astron. Astrophys., Suppl. Ser. **42**, 251 (1980).
29. T. M. Dame, D. Hartman, and P. Thaddeus, Astrophys. J. **547**, 792 (2001).
30. Y. P. Georgelin and Y. M. Georgelin, Astron. Astrophys. **6**, 349 (1970).
31. J. Brand and L. Blitz, Astron. Astrophys. **275**, 67 (1993).
32. A. Arellano Ferro and V. E. E. Mendoza, Astron. J. **106**, 2516 (1993).

Translated by K. Maslennikov

Astronomy Reports, Vol. 48, No. 4, 2004, pp. 315–326. Translated from Astronomicheskiĭ Zhurnal, Vol. 81, No. 4, 2004, pp. 348–359.
Original Russian Text Copyright © 2004 by Pavlyuchenkov, Shustov.

A Method for Molecular-Line Radiative-Transfer Computations and Its Application to a Two-Dimensional Model for the Starless Core L1544

Ya. N. Pavlyuchenkov and B. M. Shustov

Institute of Astronomy, Moscow, Russia

Received August 25, 2003; in final form, November 10, 2003

Abstract—We present a numerical method and the URAN(IA) computer code for two-dimensional, axially symmetric radiative-transfer computations in molecular lines and spectral modeling. The algorithm is based on Monte Carlo computations of the mean radiation intensity and Accelerated Λ Iterations (ALI) to provide self-consistency between the radiation field and molecular excitation. The code is applied to the structure and kinematic properties of the starless core L1544, which is often considered to be the collapsing core of a molecular cloud. This object has been well studied, but none of the one-dimensional models obtained earlier has been able to provide a self-consistent picture of its structure and kinematics. We show that the spectral features of L1544 can be reproduced in a two-dimensional model in which the cloud has an axial ratio of 2 : 1, a mean velocity of contraction (collapse) of $V_r \sim 50$ m/s, and a rotational velocity of up to $V_\phi \sim 200$ m/s. We construct the model of L1544 based on a continuous transition from an initially homogeneous cloud to the observed configuration. The velocity of the contraction is appreciably lower than is predicted by one-dimensional dynamical models. We discuss the problems of interpreting observed molecular-line profiles and prospects for developing self-consistent models for the chemical and dynamical evolution of molecular clouds. *© 2004 MAIK "Nauka/Interperiodica".*

1. INTRODUCTION

One of the most topical problems associated with the creation of a complete theory of star formation is elucidating the conditions for the transition of a molecular cloud into a collapse regime and the early stages of its subsequent evolution. It appears that the most primitive structures that can directly evolve into stars are dense fragments (cores) of molecular clouds. It is usually assumed that a core begins to collapse as soon as the conditions for gravitational instability are satisfied, forming a single or multiple star. Both this evolutionary stage and the core are sometimes referred to as "protostellar." However, it is quite possible that not all cores of molecular clouds become stars, even if they contract. For this reason, the cold nuclei of molecular clouds that do not show signs of compact internal energy sources have come to be considered as a separate group of objects—"starless cores" [1].

Direct evidence for the existence of contracting cores is provided by the presence of characteristic features associated with collapse in the molecular emission spectra. The direct observation of a collapse is difficult, since the early stages of the collapse (with the longest time scales) proceed with low (subsonic or close to sonic) velocities. The detection of such velocities under the conditions characteristic of the cores of molecular clouds requires sensitive radio telescopes with high angular and frequency resolutions. In the last decade, a number of radio telescopes with the necessary parameters have become operational and a considerable amount of observational data has been collected. A series of systematic radio surveys of the sky aimed at identifying starless cores and detecting protostellar-core candidates have been carried out (see, e.g., [2]). Several objects (B68, B335, L1544, and others) have been studied in relatively more detail and serve as test grounds for theoretical models [3]–5].

However, the interpretation of the collected data often leads to ambiguous conclusions, even within a single approach in which the structure and kinematics of an object are described by a specified set of model parameters that are "fitted" to the observational data. This is a consequence of attempting to solve this inverse problem via fitting, although additional constraints are necessary to obtain a more definite result. The use of *a priori* information, most crucially the distribution of the molecular density over the cloud, can be mostly easily justified if it is derived from self-consistent (chemical—dynamical) models for the clouds. Another problem is the absence of reliable methods for interpreting emission lines of objects with complex structures. One way to resolve this problem is to develop methods for computing the radiative transfer in molecular lines.

Methods for computing the radiative transfer in molecular lines have been applied to astrophysical problems for a relatively short time, since 1978 [6]. Several effective one-dimensional methods and associated numerical codes for the radiative-transfer computations have been developed [7]. These methods give results in good consistency with each other for one-dimensional models. However, one-dimensional modeling is not sufficient for real objects. Pavlyuchenkov *et al.* [8] considered radiative transfer in lines of the $C^{18}O$, HCO^+, and CS molecules for a spherically-symmetric, chemical–dynamical model of the starless core L1544. Their results show that, while the chemical–dynamical model can describe the main structural features of L1544 (e.g., the deficit of CCS molecules at the center), it is too crude to enable a comparison between the model and observed line profiles. The one-dimensional model of L1544 was not able to reproduce the kinematic parameters of this cloud. We believe the reason for this is the unsuitability of one-dimensional models for L1544.

Recently, the first two-dimensional algorithms for modeling radiative transfer in molecular lines have been developed (see, e.g., [9, 10]). However, in contrast to the one-dimensional numerical codes, the two-dimensional codes are not freely available. Not the least reason for this is the fact that such complicated codes for radiative-transfer computations can be used most effectively by the authors of the codes themselves.

All these circumstances led us to develop our own algorithm for multidimensional radiative-transfer computations, realized in the URAN(IA) program package, which is designed for modeling of two-dimensional axially-symmetric problems. We describe the method and the characteristics of the URAN(IA) numerical code in Section 1. Section 2 presents a two-dimensional phenomenological model for the starless core L1544. In the first part of this section, we describe the algorithm used to construct the model, and in the second part, the modeling of the radiative transfer in HCO^+ lines carried out using the URAN(IA) code. We consider the distribution of the excitation temperatures for HCO^+ transitions and compare the model and observed spectra of the $HCO^+(3–2)$ line. Section 3 briefly summarizes the results of our study and considers problems related to the construction of self-consistent models for starless cores.

2. METHOD FOR COMPUTING RADIATIVE TRANSFER IN MOLECULAR LINES

The task of modeling radiative transfer in molecular lines involves the calculation of synthetic line profiles for given distributions of the density, temperature, velocity, and other physical parameters. This requires the solution of a system of equations describing the radiative transfer. This system includes the radiative-transfer equation itself,

$$\frac{dI_\nu}{ds} = -\alpha_\nu I_\nu + j_\nu, \tag{1}$$

and a balance equation for the energy-level populations,

$$\begin{aligned} n_u \left[\sum_{l<u} A_{ul} + \sum_{l\neq u}(B_{ul}\overline{J}_{ul} + C_{ul})\right] \\ = \sum_{l>u} n_l A_{lu} + \sum_{l\neq u} n_l(B_{lu}\overline{J}_{ul} + C_{lu}), \end{aligned} \tag{2}$$

where I_ν is the spectral intensity of the radiation and n_k are the level populations. Equations (1) and (2) are related by the emission and absorption coefficients,

$$j_\nu^{ul} = \frac{h\nu_{ul}}{4\pi} n_u A_{ul}\phi_{ul}(\nu), \tag{3}$$

$$\alpha_\nu^{ul} = \frac{h\nu_{ul}}{4\pi}(n_l B_{lu} - n_u B_{ul})\phi_{ul}(\nu), \tag{4}$$

and by the mean intensity of the radiation $\overline{J}_{ul}$, which is defined by the expression

$$\overline{J}_{ul} = \frac{1}{4\pi}\int\limits_{4\pi} d\Omega \int\limits_0^\infty I_\nu \phi_{ul}(\nu)d\nu. \tag{5}$$

In these formulas, A_{ik} and B_{ik} are the Einstein coefficients; C_{ik}, the coefficients for collisional excitation; ul, indices specifying the transition $u \to l$; and $\phi_{ul}(\nu)$, the line profile function, which is defined in the approximation of total redistribution over frequency and a Maxwellian turbulence spectrum as

$$\begin{aligned} \phi_{ul}(\nu) = \frac{c}{b\nu_{ul}\sqrt{\pi}} \\ \times \exp\left(-\frac{c^2(\nu - \nu_{ul} - (\mathbf{v}\cdot\mathbf{n})\nu_{ul}/c^2)}{\nu_{ul}^2 b^2}\right). \end{aligned} \tag{6}$$

Here, ν_{ul} is the central frequency of the transition $u \to l$; $\mathbf{v}$, the regular velocity; $\mathbf{n}$, a unit vector in the direction of the photon's propagation; and b, a parameter that is related to the kinetic temperature T_k and the most probable value of the microturbulent velocity V_t by the expression

$$b^2 = \sqrt{\frac{2kT_k}{m_{mol}} + V_t^2}. \tag{7}$$

When deriving the method for solving the system of radiative-transfer equations, we used the main ideas behind the Accelerated Monte Carlo (AMC)

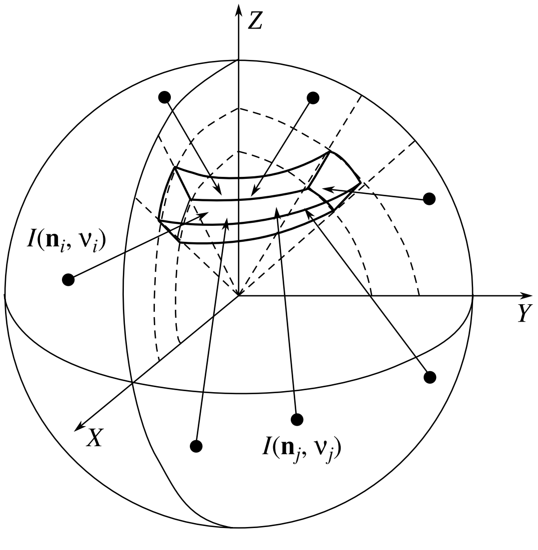

Fig. 1. Schematic of the computation of the mean radiation intensity (in a spherical coordinate system). The bold lines show the borders of an elementary cell. The rays show random directions for the integration of the transfer equation (1) for the given cell. The initial points for the integration (arrows) are randomly distributed inside the cell. The integration along each ray is continued to the boundary of the cloud. The mean radiation intensity is defined as the average of $\{I_i\}$.

method of [10] and the modified Monte Carlo method of [11]. At the basis of the algorithm lies a hierarchical sequence of inter-related methods, which we describe below.

The computational domain is split into cells. All physical quantities are constant within a cell, except for the velocity, which can vary. The essence of the method is to solve system (1), (2) iteratively; i.e., the level populations from (2) are used to solve (1) to derive the radiation intensity. In the next step of the iterations, the resulting mean radiation intensity is used to solve the population-balance equations. This algorithm is often called the Λ-iteration method.

The mean radiation intensity $\overline{J}_{ul}$ was computed using Monte Carlo simulations (Fig. 1). In each cell of the computational grid, a random set of points where the intensity is defined is chosen. Each point is assigned a random direction of propagation $\mathbf{n}_i$ and a random frequency ν_i (within the profile of the given molecular line). This set of quantities defines the radiation intensity incident on each cell, $I(\mathbf{r}_i, \mathbf{n}_i, \nu_i)$. Each $I(\mathbf{r}_i, \mathbf{n}_i, \nu_i)$ is found via direct integration of the transfer equation (1). The resulting mean intensity in the cell, $\overline{J}_{ul}$, is computed by averaging the derived intensities I_i over direction and frequency. The set of parameters $\{\mathbf{r}_i, \mathbf{n}_i, \nu_i\}$ for each cell is random but is fixed during the computations.

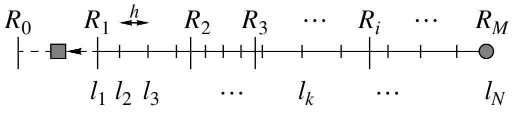

Fig. 2. Schematic of the integration of the radiative-transfer equation (1). One of the rays along which the integration is carried out is shown. $R_1, R_2, \ldots, R_M$ are the boundaries of cells that are traversed by the ray as it propagates. The cell for which the computation is made is shown at the left (R_0, R_1). The coordinate origin for the integration is shown by the square, and the outer boundary of the cloud, by a circle. The total integration path is split into intervals $l_1, l_2, \ldots, l_N$ with steps that depend on the parameters of the cell in which the integration interval is situated.

Figure 2 shows a schematic outline of the integration of the radiative-transfer equation for $I(\mathbf{r}_i, \mathbf{n}_i, \nu_i)$. The total integration path is split into intervals $l_1, l_2, \ldots$ with a step h that is smaller than the cell size. Quantities are kept constant within an interval and are determined by the values in the cell containing the interval; the velocity is also determined by the spatial coordinates of the interval. The integration is carried out from the position of the "death" of the photon inside the given cell to the edge of the cloud using the following recurrence relations:

$$I^{(1)} = S_1(1 - e^{-d\tau_1}),$$
$$I^{(2)} = I^{(1)} + S_2(1 - e^{-d\tau_2})e^{-d\tau_1},$$
$$I^{(3)} = I^{(2)} + S_3(1 - e^{-d\tau_3})e^{-(d\tau_1 + d\tau_2)},$$
$$\ldots$$
$$I^{(N)} = I^{(N-1)} + S_N(1 - e^{-d\tau_N})e^{-\tau} + I_{bg}e^{-\tau},$$
$$I = I^{(N)},$$

where S_i is the source function; $d\tau_i$, the optical depth of the ith interval; and I_{bg}, the intensity of the background radiation incident on the cloud. This procedure for integrating (1) is quite convenient for computations in curvilinear coordinates and is simple to realize.

Ideally, the integration step h and the partitioning of the computational domain into cells should be chosen based on the scale for variations of physical parameters and the optical depth of the lines. For example, the partitioning into cells must trace well the gradients of the level excitation temperature. However, the excitation temperature is itself a solution of the radiation-transfer problem. Thus, the derivation of a general criterion for the partitioning and the choice of h is a separate and complex problem. In practice, it is convenient to use an empirical approach and to test the accuracy of the results via computations with alternative grids. In our computations, the choice of the step h depended on the dimensions of the cell reached during the calculations and, as a rule, was ∼1/10 of the size of the cell. Such steps h make it possible to trace gradients of velocity within a cell and to pass relatively continuously from cell to cell during the integration.

A special method was used to accelerate the convergence of the Λ iterations, based on the fact that the radiation in the cell can be split into external and internal radiation, with the latter being generated by the gas inside the cell; i.e., $J = J_{in} + J_{ext}$. As a result of this division, an additional iteration process is introduced for each cell to bring the level populations n_k and the internal radiation field J_{in} into agreement: each new J_{in} changes the total intensity J that is used in the solution of the system of balance equations (2). The level populations found by solving (2) lead to corrections to J_{in}. When this local iteration converges, the global iteration over the whole grid is continued. Thus, the complete iteration procedure can be represented by the scheme

○ beginning of global iterations (over l) for whole grid

  $>$ $n_k^{(l)} \rightarrow$ **solution of the radiative-transfer equation** $\Rightarrow J_{ext}^{(l+1)}$

  $>$ beginning of local iterations (over m) for a cell

    $\gg$ $n_k^{(l),(m)} \rightarrow J_{in}^{(l),(m)} \Rightarrow J^{(l),(m)} = J_{ext}^{(l+1)} + J_{in}^{(l),(m)}$

    $\gg$ $J^{(l),(m)} \rightarrow$ **solution of the balance equations** $\Rightarrow n_k^{(l),(m+1)}$

  $>$ end of local iterations, $n_k^{(l+1)} = n_k^{(l),(m+1)}$

○ end of global iterations

The system of linear balance equations (2) is solved using a standard LU decomposition method. The iterations are continued until the level populations in each cell obtained in successive iterations differ by less than $\epsilon = 10^{-3}$.

After the solution of (1), (2) is found, the error associated with the Monte Carlo computations of J is estimated. An alternative random set of $\{\mathbf{r}_i, \mathbf{n}_i, \nu_i\}$ is generated for each cell and the radiative transfer is again solved. The maximum error in the level populations is defined by the difference between the solutions obtained in the two computations. If statistical information about the accuracy of the Monte Carlo modeling is desired, additional computations with different sets of $\{\mathbf{r}_i, \mathbf{n}_i, \nu_i\}$ can be carried out for this purpose.

This method is fairly universal and may be applied to problems with any number of dimensions and in any coordinate system. We realized the method via the URAN two-dimensional numerical code, designed for axially symmetric radiative-transfer computations. The code uses a spherical coordinate system, which provides flexibility that enables the solution of one-dimensional spherically symmetric problems.

We constructed theoretical emission spectra based on the self-consistent level populations obtained with the URAN code using our URANIA program. This program enables the construction of spectra in a format consistent with the features of the observed spectra. This program is also used to analyze the modeling results, for example, for visualization of the distributions of the level excitation temperature. It is convenient to separate the computation of the theoretical spectra into two stages—modeling of the radiative transfer and construction of the spectra.

The URAN+URANIA program package was carefully tested by solving several one- and two-dimensional problems. In the one-dimensional regime, the code fully satisfied all tests formulated from the results of a conference on molecular radiative transfer (Leiden University, 1999, http://www.strw.leidenuniv.nl/∼radtrans). For tests in the two-dimensional regime, we used several simple problems with theoretically predictable solutions (a cloud with rigid-body rotation, an ellipsoidal cloud, etc.). In addition, together with the developer of the well-known two-dimensional RATRAN code [10], M Hogerheijde, we compared the results obtained using both codes for a model accretion disk. The corresponding results were identical within acceptable errors.

3. TWO-DIMENSIONAL MODEL OF L1544

3.1. Computational Method and Model Parameters

The most promising method for modeling the evolution of starless cores is the construction of coupled, chemical—dynamical evolutionary models. However, two-dimensional models of this kind are not yet available. As a first approximation, it is useful to have a simple model that can be used to estimate the influence of the most important factors related to the two-dimensional structure of the clouds. We constructed a two-dimensional model for L1544 using a "phenomenological" approach, in which the model is described by a simple set of observational parameters (that determine the shape, density distribution, etc.) and a number of natural physical assumptions.

Let us consider a spherically symmetrical cloud with the following density distribution for its H_2 molecules:

$$n(\mathrm{H}_2) = \frac{n_0}{1 + (r/r_0)^{\beta}}, \tag{8}$$

where n_0 is the central density; r_0, the size of an inner part of the cloud with nearly uniform density; and β, the index for the power law describing the density decrease in the outer parts of the cloud. Expression (8) is often used to describe the structure of observed interstellar clouds [12]. However, the spherically symmetric distribution (8) is not sufficient to describe L1544, since the interferometric observations of [13, 14] have shown that this core is elongated, making a spherically symmetric approximation for its shape crude. To take into account the deviation from spherical symmetry, we stretched the nonuniform cloud described by (8) axially symmetrically along the equatorial plane by a factor α. We will use the nonuniform ellipsoidal cloud obtained in this way as a model for the starless core. Mathematically, this structure is described by the expression

$$n(\mathrm{H}_2) = \frac{n_0^*}{1 + \left(\sqrt{(R^2/\alpha^2 + z^2)}/r_0\right)^{\beta}}, \tag{9}$$

where R is the distance to the symmetry axis and z is the distance to the equatorial plane. For convenience, we label the nonuniform cloud described by (9) with the letter E and the spherically symmetric cloud described by (8) with the letter S.

To define the components of the regular velocity in the cloud, we will make several assumptions. We assume that the ellipsoidal cloud E *evolves* from a spherically symmetric cloud U with the same mass and with the initial density n_u (Fig. 3). Physically, this assumption reflects the fact that, due to the influence of magnetic fields and rotation, the contraction proceeds nonuniformly in the course of the assumed collapse: it will be faster in the polar regions and slower in the equatorial plane. We select in the initial cloud U a volume element dV_{U} that is toroidal in shape, has a small cross section, and is centered on the symmetry axis Z. Assuming a continuous transformation of the configuration U into configuration E, it is possible to determine the coordinates of the volume element in the cloud E. To do this, consider two consecutive transformations:

(1) a spherically symmetric contraction of U that forms the cloud S;

(2) an axially symmetric stretching of S that forms the cloud E.

For spherically symmetric contraction, the conservation of mass can be used to find a unique correspondence between the volume elements of clouds U and S, dV_{U} and dV_{S}. In the case of linear stretching, there is also a unique correspondence between dV_{S} and dV_{E}. Thus, there is likewise a correspondence between dV_{U} and dV_{E}, which enables us to define the velocity field. Axially symmetric stretching along the equatorial plane increases the volume of each element by a factor of α^2; i.e., with such a transformation, it is necessary to reduce the density of each element by a factor α^2 to preserve the mass of the cloud.

Let t be the time scale for the evolution of the system, i.e., the time for the transformation of configuration U into configuration E. We define the vector in the meridional plane $\mathbf{R}_{\mathrm{UE}}$ connecting each pair of corresponding elements (tori) dV_{U} and dV_{E}. The vector $\mathbf{R}_{\mathrm{UE}}$ describes the displacement of the volume element in the meridional cross section plane during the contraction of the core. We determine the velocity using t and $\mathbf{R}_{\mathrm{UE}}$:

$$\mathbf{V}_{\mathrm{E}} = \frac{\mathbf{R}_{\mathrm{UE}}}{t}. \tag{10}$$

The vector $\mathbf{V}_{\mathrm{E}}$ characterizes the mean velocity of the element dV in the meridional plane over the time t. We will assume that this velocity is approximately equal to the instantaneous velocity of the element in cloud E. Then, the components V_r and V_θ of the regular velocity in the spherically symmetric coordinate system can be approximately determined as projections of the velocity vector $\mathbf{V}_{\mathrm{E}}$ onto the vectors of the local basis of the spherical coordinate system constructed for dV_{E}.

To determine the azimuthal velocity component, we consider the conservation of momentum. We will assume that the initial cloud U rotates rigidly with angular velocity Ω and that the momentum of each element (torus) is conserved; i.e., the momentum is not redistributed during the contraction. The azimuthal velocity V_ϕ will then be

$$V_\phi = \frac{\Omega R^2(\mathrm{U})}{R(\mathrm{E})}, \tag{11}$$

where $R(\mathrm{U})$ and $R(\mathrm{E})$ are the radii of the elements' orbits measured from the symmetry axes in clouds U and E.

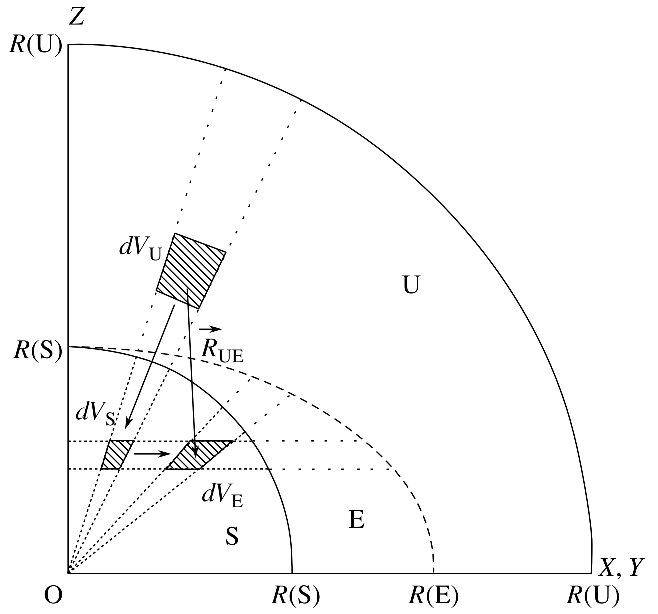

Fig. 3. Scheme for constructing the model of the starless core L1544. R(U) is the radius of the initial uniform spherical cloud U. R(S) is the radius of the nonuniform spherical cloud S, obtained via the contraction of U. R(E) defines the boundary of the nonuniform elliptical cloud that is obtained by linearly stretching S. The radius R(S) coincides with the boundary of the computational grid. We show the upper right quadrant of the meridional cross section.

The density and regular-velocity distributions for the model of L1544 obtained using the algorithm described above are shown in Fig. 4. The parameters used to derive these distributions are listed in the table. We should comment on the choice of the parameters n_0^*, r_0, β. In [12], the values $\tilde{n}_0 = 1.4 \times 10^6$ cm^{-3}, $\tilde{r}_0 = 3000$ AU, and $\tilde{\beta} = 2.5$ were used for a spherically symmetric model of L1544; these values were obtained by averaging the structural parameters of the real cloud over the angular coordinate. It is easy to estimate the mass of L1544 using these values: $\tilde{M} = 14M_\odot$. For cloud S, we will use these values of $\tilde{r}_0$ and $\tilde{\beta}$ for r_0 and β but choose the value of n_0 to be $n_0 = 2\tilde{n}_0$, so that we have $M = 2\tilde{M}$ for the mass of the model cloud and $n_0^* = 0.5\tilde{n}_0$ for the central density in cloud E, in accordance with our choice of the contraction coefficient $\alpha = 2$. The boundary of the computational grid is chosen so that the density of cloud E at its boundary is $n(H_2) = 10^3$ cm^{-3}, i.e., lower than the critical density for collisional excitation of HCO$^+$. The kinetic temperature T_k, microturbulence velocity V_{turb}, and relative abundance ξ(HCO$^+$) are fixed over the entire volume of the cloud. These assumptions are quite plausible for T_k and V_{turb} [12]. At the same time, it has been reliably established that the abundances of many molecules are reduced at the center of the L1544 cloud [13]. However, earlier computations found that the relative abundance of HCO$^+$ molecules does not decrease strongly toward the center [15]. The use of a constant abundance of HCO$^+$ is also justified by the high optical depth of the lines we are modeling. In this case, the influence of the nonuniformity of the HCO$^+$ abundance does not change the characteristic line profiles very much.

The parameters that were varied are the evolutionary timescale t and the initial angular velocity Ω. The limits for t and Ω were based on estimates of possible time scales for the (chemical and dynamical) evolution and the characteristic angular momenta of clouds.

We followed two guidelines when constructing the models. On the one hand, in our phenomenological approach, the continuous structure of the clouds must be described by a small number of parameters. On the other hand, the model distributions must be as physically justified and consistent as possible. The algorithm presented here enables us to solve this problem to some extent, despite the fact that a number of disputable assumptions lie at its basis. We stress that our model is aimed at estimating factors related to the two-dimensional structure of the clouds only and is intended to have a largely illustrative nature. A more realistic analysis will require hydrodynamical computations.

3.2. Comparison and Interpretation of Observed and Computed Spectra of L1544

We chose the HCO$^+$ molecule for the radiative-transfer computations and comparison with observations. This choice was based on the fact that detailed

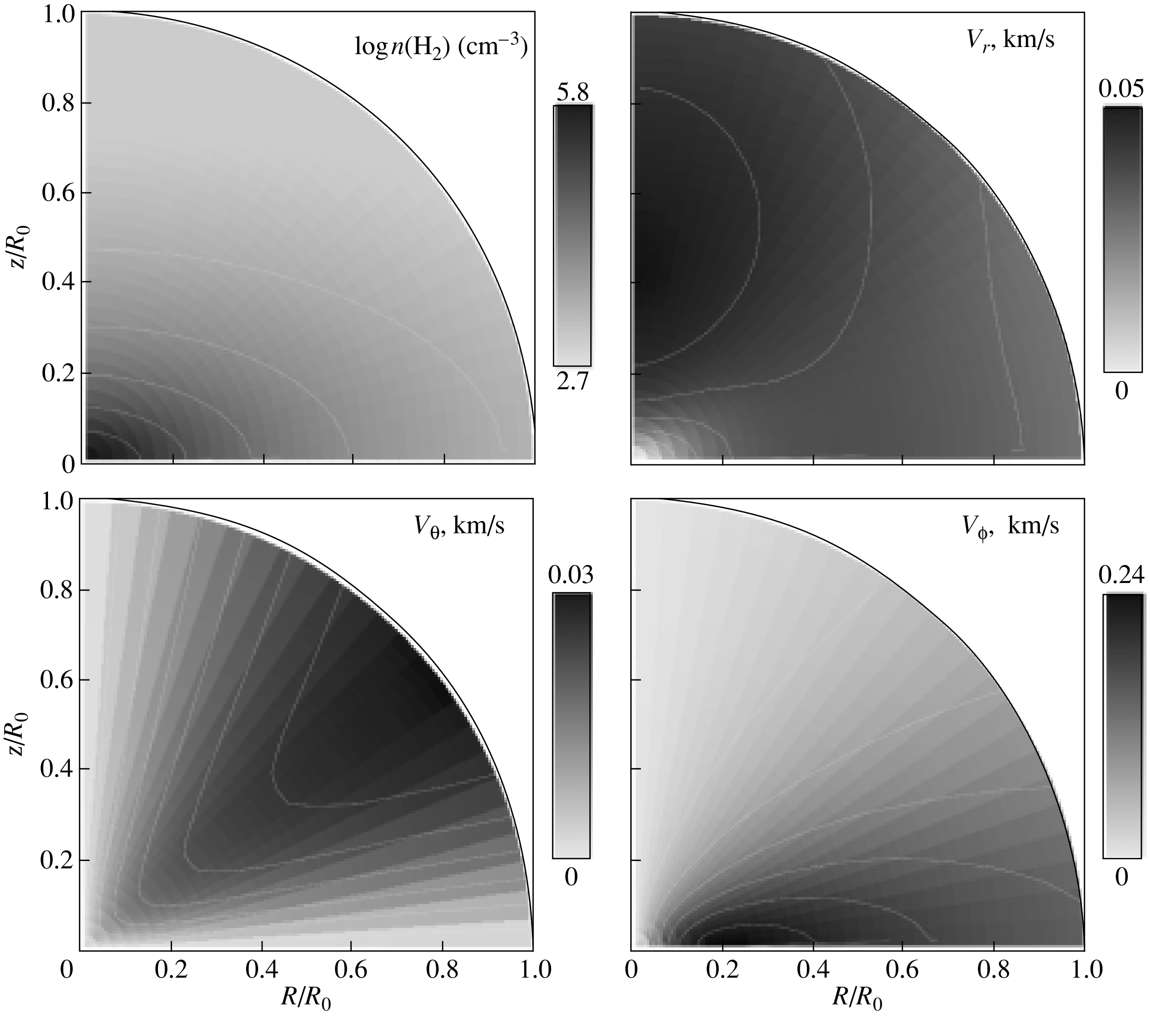

Fig. 4. Distributions of the H_2 density (upper left) and of the components V_r, V_θ, and V_ϕ of the regular velocity (upper right, lower left, and lower right) in the model of L1544. The upper right quadrant of the meridional cross section is shown for each distribution.

mapping of L1544 [16] in various HCO^+ lines are available, which make it possible to trace the spatial and kinematic structure of the cloud. In addition, the modeling of the radiative transfer in the HCO^+ lines is made appreciably easier by the simplicity of the energy levels of this linear molecule.

Radiative-transfer solutions were found for each set of varied parameters t and Ω. The best agreement between the model and observed spectra was obtained for $t = 6$ Myr and $\Omega = 6 \times 10^{-15}$ s^{-1}; this model is discussed in detail below, after which we present the results of the parameter variations.

The radiative-transfer modeling was carried out on a spherical grid with 32×24 cells. We included the first 20 transitions between 21 energy levels of the HCO^+ molecule. The computations used 500 photon packets per cell and an integration step equal to one-tenth of the size of the current cell. The total number of iterations was 16 for absolute errors in the level populations of $\psi_1 = 10^{-3}$ and a fixed set of photons, with the average number of subiterations in the ALI method being 10. The optical depth at the center of the HCO^+(1–0) line was $\tau \sim 50$. The maximum absolute error associated with the Monte Carlo computations of the mean intensity of the radiation was $\psi_2 = 10^{-2}$. This estimate was found by control iterations with sets of photon packets that were different from the specified set. The total computational time was 14 h on a CELERON 700 MHz processor. The molecular constants for HCO^+ and the collisional-excitation coefficients for H_2–HCO^+ were taken from [17, 18].

Figure 5 shows the computed excitation temperatures for the (1–0) and (3–2) transitions. The distributions of the density and excitation temperature clearly show that the excitation of HCO^+

Parameters of the model of L1544

Parameter	Notation	Value	Reference
Mass of the cloud	M	28 $M_\odot$	[5, 12]
Central concentration	n_0^*	0.7×10^6 cm^{-3}	[12]
Radius of the core	r_0	3000 AU	[12]
Index of the density profile	β	2.5	[12]
Degree of contraction	α	2.0	[13, 14], present paper
Initial density	n_u	10^3 cm^{-3}	present paper
Initial angular velocity (var)	Ω	6×10^{-15} s^{-1}	present paper
Evolutionary timescale (var)	t	6 Myr	present paper
Temperature	T_k	8.75 K	[12]
Microturbulence velocity	V_{turb}	0.2 km/s	[12]
HCO$^+$ abundance	ξ	5×10^{-10}	[15]
Inclination of rotational axis	i	75°	[13, 14], present paper
Position angle	PA	135°	[13, 14], present paper

Note: In the first column, parameters that were varied are marked “(var).”

molecules is effective in zones with $n(\mathrm{H_2}) > n_c = 10^4$ cm^{-3}, where n_c is the so-called critical density. In these zones, the excitation temperature for the lower HCO$^+$ transitions approaches the kinetic temperature of the gas. In zones with $n < n_c$, radiative absorption becomes the main mechanism for the excitation. Comparison of the excitation temperatures for HCO$^+$(1–0) and HCO$^+$(3–2) shows that, averaged over the cloud, the excitation temperature for HCO$^+$(1–0) is higher than for HCO$^+$(3–2). A simple physical explanation for this is that the excitation of higher levels requires more intense excitation, in particular, higher density, $n(\mathrm{H_2})$.

Computed spectra and the corresponding HCO$^+$(3–2) line profiles are shown in Fig. 6. The observed spectra of L1544 are taken from [16]. The ranges for all spectra in the map are similar and equal to [−0.3 K, 3.5 K] for the intensity represented by the temperature T$_{mb}$; the velocity range is $[V_{lsr} - 1.25, V_{lsr} + 1.25]$ km/s, where V_{lsr} is the radial velocity of the source. The model HCO$^+$(3–2) spectra shown in Fig. 6 (and the following figures) were convolved with the telescope beam, represented by a Gaussian with HPBW = 26″. The model spectra were computed for a higher velocity resolution than that in the observed spectra.

If theoretical emission spectra are to be computed for a model that is not spherically symmetric, information about the orientation of the cloud relative to the line of sight must be provided. The orientation of the model L1544 cloud was adjusted to provide the best fit between the theoretical and observed spectra. This best fit was obtained when the angle between the symmetry (polar) axis and the line of sight was $i = 75°$ and the positional angle relative to the vertical direction specified by a declination circle was PA = 135° (or 45°, depending on the sign of the cloud’s rotational velocity).

The spectra show that the intensity and width of the model and observed lines agree well over the entire spectral map. We can see that the intensity of the lines varies much more strongly in the direction of the diagonal from the upper left to the lower right corner (along the rotational axis) than in the direction perpendicular to this (in the plane of rotation). This intensity relationship is a consequence of the specified elongated configuration of the cloud and of the fitting of the inclination and positional angle.

The agreement of the shapes of the profiles in the observed and model spectra is an even more important result. Both spectra are characterized by double-peaked profiles. In the model spectra, the dips between the profile peaks are a consequence of self-absorption of optically thick emission in the outer regions of the cloud, where the emission at the line centers arrives from the periphery, while the emission in the line wings arrives from inner regions that have higher excitation temperatures (Fig. 5). Moreover, comparison of the spectra with coordinates [−20″, 20″] and [30″, −30″] shows that the asymmetry of the model lines reproduces the

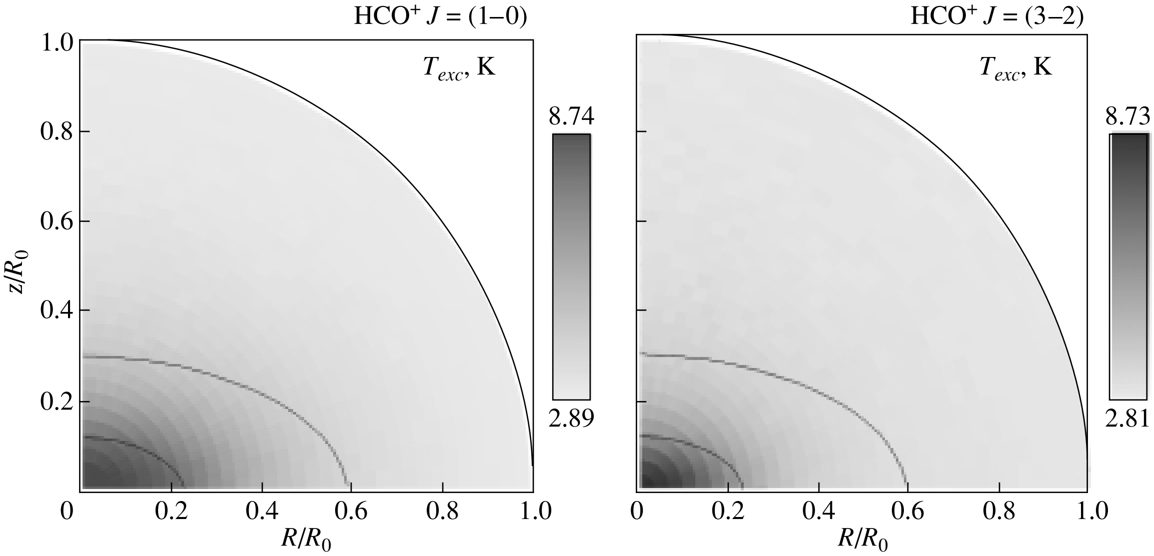

Fig. 5. Distributions of the excitation temperature in the $HCO^+(1-0)$ and $HCO^+(3-2)$ transitions obtained from the radiative-transfer computations for the L1544 model. The solid curves correspond to contours of equal density of $n(H_2) = 10^4$, 10^5 cm^{-3} toward the center of the cloud.

characteristic asymmetry of the observed lines. For example, a typical profile with a dominant blue (left) peak, usually considered to be a signature of collapse, is well represented in the upper right corner of the map, while a profile with a dominant red (right) peak, usually taken to be associated with outflow, is present in the lower left corner. In reality, in our model, this change in the type of asymmetry is due to the differential rotation of the cloud. Differential rotation alone (without compression) results in the formation of antisymmetric spectra placed symmetrically about the rotational axis. Compression alone (without rotation), on the contrary, results in the formation of profiles with dominant blue peak only. In the case of simultaneous rotation and compression of the cloud, their actions are added and a pattern with some predominance of the blue peaks is formed. Precisely this situation is represented in the obtained model map.

Let us now consider the results of varying t and Ω. Figure 7 shows the model and observed emission spectra for the central regions of L1544 for the three values of the evolutionary timescale $t = 1$, 6, and 12 Myr for the fixed angular velocity $\Omega = 0$. A qualitative comparison of the shapes of the spectral lines demonstrates that the model with the shortest time scale, $t = 1$ Myr, yields profiles that are too asymmetric, while the spectra obtained for $t = 6$ and 12 Myr are more symmetrical. However, none of the models with $\Omega = 0$ produce profiles with two types of asymmetry (the spectra at $[-15'', 15'']$ and $[15'', -15'']$).

Figure 8 shows the spectra obtained for initial angular velocities of $\Omega = 0.6 \times 10^{-15}$, and 12×10^{-15} cm^{-1} for the fixed time scale $t = 6$ Myr. We can see that the rotation of the cloud leads to changes in the asymmetry of the lines relative to the projected rotational axis of the cloud. However, the model with the fastest rotation, $\Omega = 12 \times 10^{-15}$ cm^{-1}, produces too asymmetric profiles with dominant left peaks (the position $[-15'', 15'']$ in the right spectral map).

Summarizing our comparison of the observed and model $HCO^+(3-2)$ molecular emission spectra, we see that they are in qualitative agreement and, hence, the starless core L1544 can be well represented by a model with an elongated cloud with $t \sim 6$ Myr and $\Omega \sim 6 \times 10^{-15}$ cm^{-1}.

4. DISCUSSION

The main result of the present study is the creation of the URAN(IA) numerical code for radiative-transfer computations in molecular lines. This code is designed to produce model theoretical spectra and analyze the observed emission spectra of molecular clouds. It can be used to carry out radiative-transfer computations for one-dimensional (spherically symmetric) and two-dimensional (axially symmetric) problems. The axially symmetric situation is probably closer to the structure of real clouds. When any sophisticated code is used, the questions of the trustworthiness of the results, its relative advantages and disadvantages, and prospects for future development inevitably arise. The reliability of the code was already discussed at the end of Section 1; our code gives results that are consistent with those of other one-dimensional codes and with one existing

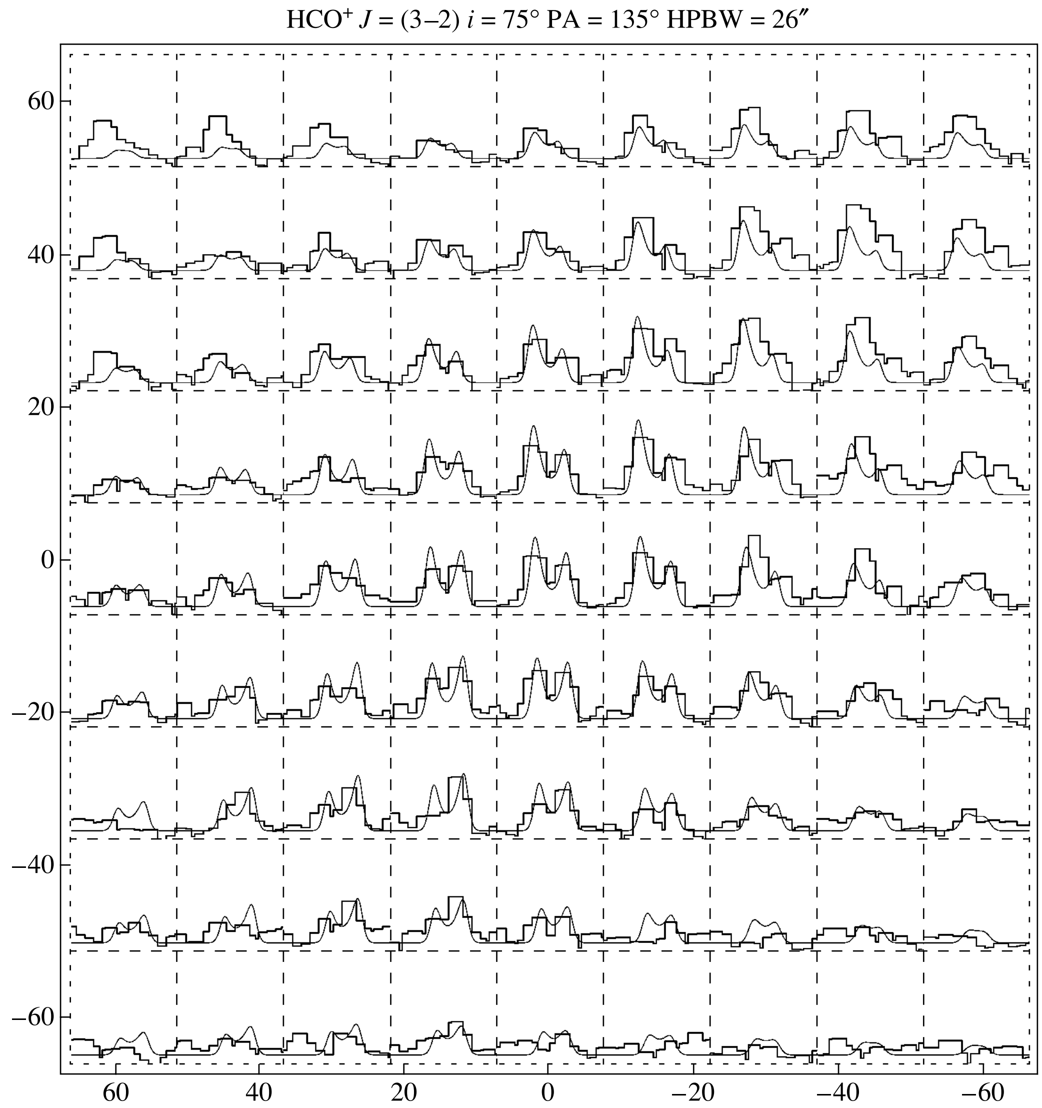

Fig. 6. Comparison of observed (step-wise contours) and model (solid contours) $HCO^+(3-2)$ spectra. Each panel with spectra corresponds to the region in the cloud whose coordinates are indicated on the axes in arcseconds relative to the source center (declination is plotted on the horizontal and right ascension on the vertical axis). The observed line profiles for L1544 are taken from [16]. The theoretical profiles were computed for the model with $t = 6$ Myr and $\Omega = 6 \times 10^{-15}$ cm^{-1}.

two-dimensional code. Comparison of results and practical experience has demonstrated the advantages of the URAN(IA) code: its simplicity, the physical clarity of the algorithm, its high efficiency for problems with large optical depth, its flexibility, and the economy of the code with regard to the organization of the computations. Its main disadvantage is probably the large amount of computer time required for the modeling; however, the time required for real two-dimensional computations is acceptable and does not exceed several tens of hours. We discussed the prospects for the method in our earlier work [8]. One important task is the construction of a self-consistent, chemical–dynamical, two- or three-dimensional evolutionary code, which, combined with the complex of programs for the radiative-transfer computations, would provide a powerful tool for the analysis of observations and studies of the structure, kinematics, and evolutionary state of starless cores.

Another important and as yet unsolved problem is the development of a simple and reliable numerical criterion for judging the consistency of observed and computed spectra. As we showed in Section 2, the most complete observational data on the structure and kinematics of the clouds are "hidden" in spectral maps. In this case, comparisons of results remain a question of naked-eye estimation, since standard numerical criteria are likely not adequate. The reason for this is that it is important to take into account not only deviations of the computed points from the ob-

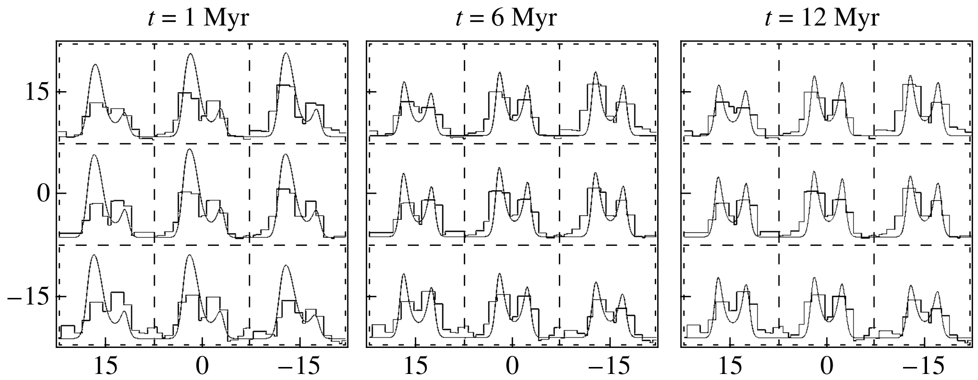

Fig. 7. Results of varying the evolutionary time scale of the cloud t. The observed and computed $HCO^+(3-2)$ emission spectra for the central regions of L1544 are shown. Computed spectra are presented for the models with $t = 1$, 6, and 12 Myr (left, middle, and right spectral maps, respectively). The initial angular velocity of the models was set to $\Omega = 0\ s^{-1}$. The coordinates are as in Fig. 6.

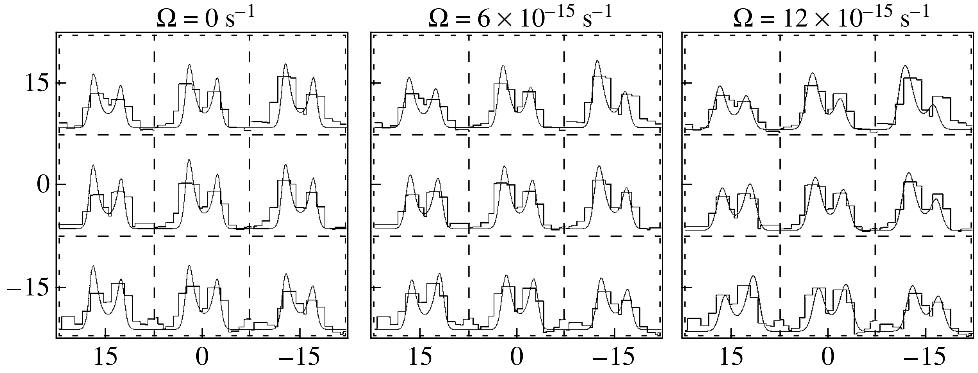

Fig. 8. Results of varying the cloud angular velocity Ω. The observed and computed $HCO^+(3-2)$ emission spectra for the central regions of L1544 are shown. Computed spectra are presented for the models with $\Omega = 0, 6 \times 10^{-15}$, and $12 \times 10^{-15}\ s^{-1}$ (left, middle, and right spectral maps, respectively). The evolutionary time scale for all the models was set to $t = 6$ Myr. The coordinates are as in Fig. 6.

served line profile but also the agreement for different details that have different weights in the evaluation of the overall pattern, such as asymmetries, dips, and regularities in the spatial distribution. In addition, the analysis should not take into account only observations of a single line but all spectral observations available, including lines of other molecules and/or for different transitions of the same molecule.

As an application of our code, we have considered a phenomenological two-dimensional model for the starless core L1544. Despite its simplicity, the model is able to reproduce the main spectral features of L1544 in the $HCO^+(3-2)$ lines. We have not modeled the lines of other molecules, but the observed spectral maps of L1544 in lines of CS [19], N_2H^+ [14], and HCN [20] typically display qualitatively similar features. These features arise in our model under the assumption that the object is a slowly contracting, elongated, differentially rotating cloud.

Our estimate of the age of L1544, $t \sim 6$ Myr, is in good agreement with an estimate based on the “chemistry” of the cloud obtained in the one-dimensional dynamical model of [15], $t \sim 5.7$ Myr. However, the velocity of the compression obtained in the phenomenological model, $V_r \sim 50$ m/s, is appreciably lower than the velocity of the collapse in the dynamical model of [15], where V_r reaches 200 m/s. In this respect, the new results confirm our earlier suggestions [8], which were proposed to obtain consistency between observed and theoretical spectra based on the dynamical model. Evidence for a low contraction velocity of L1544 is also provided by the observational results of [2, 14], which yielded the estimate $V_r \sim 50$–80 m/s. The mean rotational velocity for the phenomenological model is in good agreement with the value obtained in [13], where $V_\phi \sim 100$ m/s is inferred for the outer regions of L1544. Thus, the two-dimensional model presented in this paper supports the hypothesis that the starless core L1544 is not collapsing. It is possible that L1544 is supported in an almost steady state by its rotation.

ACKNOWLEDGMENTS

The authors are grateful to M. Hogerheijde for his help in testing the two-dimensional code, A. Lapinov for discussions of the nature of the asymmetry of the line profiles in L1544, R. Launhardt and T. Henning for fruitful discussions of problems in interpreting the spectra of protostellar clouds, and the referee for valuable remarks. This work was supported by the Russian Foundation for Basic Research (project codes 01-02-16206, 03-02-06756) and a joint project of the Russian Foundation for Basic Research and the Deutschen Forschungsgemeinschaft (project code 02-02-04008).

REFERENCES

1. P. Andre, D. Ward-Thomson, and M. Barsony, in *Protostars and Planets IV*, Ed. by V. Mannings, A. P. Boss, and S. S. Russell (Univ. of Arizona Press, Tuscon, 2000), p. 59.
2. C. W. Lee, P. C. Myers, and M. Tafalla, Astrophys. J., Suppl. Ser. **136**, 703 (2001).
3. S.-P. Lai, T. Velusamy, W. D. Langer, and T. B. H. Kuiper, Astron. J. **126**, 311 (2003).
4. J. M. C. Rawlings, N. J. Evans, and S. Zhou, Astrophys. Space Sci. **216**, 155 (1994).
5. M. Tafalla, D. Mardones, P. C. Myers, *et al.*, Astrophys. J. **504**, 900 (1998).
6. C. Bernes, Astron. Astrophys. **73**, 67 (1979).
7. G.-J. van Zadelhoff, C. P. Dullemond, F. F. S. van der Tak, *et al.*, Astron. Astrophys. **395**, 373 (2002).
8. Ya. N. Pavlyuchenkov, B. M. Shustov, V. I. Shematovich, *et al.,* Astron. Zh. **80** (3), 1 (2003) [Astron. Rep. **47**, 176 (2003)].
9. C. P. Dullemond and R. Turolla, Astron. Astrophys. **360**, 1187 (2000).
10. P. C. Hogerheide and F. F. S. van der Tak, Astron. Astrophys. **362**, 697 (2000).
11. M. A. Voronkov, Pis'ma Astron. Zh. **25** (3), 186 (1999) [Astron. Lett. **25**, 149 (1999)].
12. M. Tafalla, P. C. Myers, P. Caselli, *et al.*, Astrophys. J. **569**, 815 (2002).
13. N. Ohashi and S. W. Lee, Astrophys. J. **518**, L41 (1999).
14. J. P. Williams, P. C. Myers, D. J. Wilner, and D. J. Francesco, Astrophys. J. **513**, L61 (1999).
15. Z.-Y. Li, V. I. Shematovich, D. S. Wiebe, and B. M. Shustov, Astrophys. J. **569**, 792 (2002).
16. E. Gregersen, N. Evans, D. Mardones, and F. Maers, Astrophys. J. **533**, 440 (2000).
17. T. S. Monteiro, Mon. Not. R. Astron. Soc. **214**, 419 (1985).
18. S. Green, Astrophys. J. **201**, 366 (1975).
19. M. Tafalla, D. Mardones, P. C. Myers, *et al.*, Astrophys. J. **504**, 900 (1998).
20. A. Lapinov, private communication (2003).

Translated by L. Yungel'son

Astronomy Reports, Vol. 48, No. 4, 2004, pp. 327–331. Translated from Astronomicheskiĭ Zhurnal, Vol. 81, No. 4, 2004, pp. 360–364.
Original Russian Text Copyright © 2004 by Yudin.

The Dust Envelope of R CrB in June 2001: Detection of a Compact IR Source

B. F. Yudin

Sternberg Astronomical Institute, Universitetskiĭ pr. 13, Moscow, 119992 Russia

Received March 14, 2003; in final form, November 10, 2003

Abstract—We present the results of a joint analysis of JHK interferometric and $UBVJHKLM$ photometric observations of RCrB acquired in June 2001. The baseline for the IOTA interferometer was 21.18 m. During the observations, the star was in its bright state in the V band and near its maximum brightness in the L band. Our analysis reveals an IR source that is considerably smaller than the extended dust envelope discovered earlier. We identify this compact IR source with the emission from a group of dust clouds. The linear scale (diameter) of the IR source was $d_{in,c} \approx 13.5D_*$ (its angular diameter is $\theta_{in,c} \approx 6.4$ mas). About 7% of the star's radiation was obscured by this group of clouds, which contributed $\sim$14% of the total IR excess of R CrB and $\sim$22% of the K-band flux. The color temperature of the compact source was only $\sim$300 K higher than the color temperature of the extended dust envelope. The inner boundary of the extended dust envelope had a diameter of $d_{in,e} \approx 90D_*$ ($\theta_{in,e} \approx 43$ mas). *© 2004 MAIK "Nauka/Interperiodica".*

1. INTRODUCTION

R CrB is the prototype of a small group of peculiar supergiants with strong hydrogen deficiencies and carbon excesses in their atmospheres. The visual brightness of these stars experience unpredictable dimmings that can be as deep as 8^m, as is the case with R CrB itself. The deep dimmings of the visual brightness are related to the formation of optically thick dust clouds in the line of sight, which screen the star from the observer. While there is currently no doubt that this picture is correct, the distance from the star where these clouds condense remains unknown. In existing models, the clouds are formed either very close to ($\sim 2R_*$ [1]) or at a considerable distance from ($\sim 20R_*$ [2]) the star.

The circumstellar gas envelope of R CrB is filled with dust grains that manifest their presence via the IR excess of the star, which was first detected by Stein *et al.* [3]. It was later shown that the brightness of R CrB in the L band, where the radiation of the dust envelope considerably exceeds that of the star itself, varies with a total amplitude of $\Delta L \approx 1\overset{m}{.}5$ [4–6]. Two harmonics have been reliably identified in these semiregular variations, with periods of $\sim$3.3 yr and $\sim$11.9 yr and total amplitudes of $\sim 0\overset{m}{.}8$ and $0\overset{m}{.}6$ [7]. The IR excess contributes $\sim$25% of the bolometric flux of the star when it has its mean brightness.

The IR excess of R CrB is similar to the IR excesses of normal supergiants from the point of view of its spectral energy distribution (SED) and can be reproduced in a model with an optically thin carbon dust cloud. The envelope condenses at a large distance from the star ($\sim 110R_*$) from the stellar wind, which resembles the stellar winds of normal supergiants. The grain temperature at the inner boundary of the dust envelope is $\sim$860 K when R CrB is at its mean brightness. The dust envelope consists mainly of fine ($a_{gr} \leq 0.01$ μm) grains. The brightness variations of the envelope are not accompanied by significant color changes and are due to variations of its optical depth within the range $\tau(V) = 0.2$–0.4. The optical-depth variations of the extended dust envelope, in turn, are due to changes in the star's mass-loss rate due to changes in its level of activity (see [7] for more detail on the structure of the gas envelope of R CrB).

The dust clouds are generated by activity of an unknown nature at the stellar surface. Without this activity, R CrB would display only the stellar wind of a normal supergiant. The activity at the stellar surface probably first creates dense gas clouds, which are then embedded in the relatively rarefied stellar wind. The dust grains in these clouds condense much closer to the star than those formed in the stellar wind, i.e., in the space between the clouds. Therefore, if the grains in the extended dust envelope and in the dust clouds are similar, the clouds must be much warmer than the extended dust envelope. Accordingly, if there are sufficiently many clouds, a hot component should be present in the IR excess [7].

However, there is no obvious evidence for the presence of hot clouds in the IR spectrum of R CrB. The presence of the dust clouds is clearly manifest during

1063-7729/04/4804-0327$26.00 © 2004 MAIK "Nauka/Interperiodica"

deep dimmings of the star's optical brightness when they form in the line of sight. In 1999, a very deep optical dimming of this kind coincided by chance with a very deep minimum of the IR brightness, so that the background radiation from the star itself and from the extended dust envelope, which usually hinders the detection of radiation from the dust clouds, was minimal. It appeared that it had become possible to detect the hot component of the IR excess in this optimal case. However, its bolometric flux was only $\sim 1\%$ of the bolometric flux of the extended dust envelope at its mean brightness [7].

The existence of the extended dust envelope was directly demonstrated in K-band speckle interferometric observations of R CrB carried out using the 6-m telescope of the Special Astrophysical Observatory (SAO, Russian Academy of Sciences). The spatial resolution [~ 75 milliarcseconds (mas)] corresponded to the telescope's diffraction limit at 2.2 μm. However, this spatial resolution is insufficient to detect even a group of dust clouds. Model computations show that the angular diameter of the dust envelope's inner boundary is ~ 40 mas [8].

We present here an analysis of JHK interferometric and $UBVJHKLM$ photometric observations of R CrB acquired in June 2001, when the star was in its bright state in the optical and close to its maximum brightness in L. The interferometric observations were obtained on June 5, 2001, using the IOTA interferometer with a baseline of 21.18 m. The JHK visibility functions (normalized two-dimensional Fourier transforms of the surface brightness [9]; we will refer to these as the IOTA visibility curves) were 0.97 ± 0.06 (77.2 arcsec^{-1}), 0.78 ± 0.06 (61.5 arcsec^{-1}), and 0.61 ± 0.03 (47.6 arcsec^{-1}), respectively [10]. The corresponding spatial frequencies (q) are given in parentheses. The $UBVJHKLM$ magnitudes of R CrB for June 10, 2001, were taken from [7]: $U \approx 6.71$, $B \approx 6.59$, $V \approx 5.99$, $J \approx 5.05$, $H \approx 4.84$, $K \approx 3.82$, $L \approx 1.88$, and $M \approx 1.30$.

These observations reveal the presence of a compact IR source that contributes appreciably to the total IR excess. We associate this source with the radiation from a group of dust clouds. Based on computations using a semiempirical model for the compact dust structure and an existing model for the extended dust envelope, we were able to simultaneously reproduce the HK visibility curves of R CrB and the SED in the optical and IR. This enabled us to estimate a number of parameters of the compact IR source.

2. DETECTION OF THE COMPACT IR SOURCE

We suppose that the stellar wind of R CrB consists of an ordinary, spherically symmetric wind with parameters typical of the winds of normal supergiants, with embedded gas clouds with a different density [7, 11]. The wind intensity and the number of dust clouds vary in time. An extended dust envelope forms from the stellar-wind material at a considerable distance from the star, while the dust clouds are formed of gas clumps closer to the star.

Figure 1 shows the K visibility curve for R CrB obtained at the SAO 6-m telescope in October 1996 (the SAO visibility curve) together with the IOTA visibility curves for R CrB. This figure also displays the visibility curve computed using a model with a star and extended gas envelope (model 1) for October 1996 together with the individual components of this visibility curve: for the star (a point IR source) and the extended dust envelope (an extended IR source). This model can also reproduce the star's SED at that epoch.

The computations for model 1 were similar to those described in [7] but with the cel1000 grain sample from [12] replaced by the ACAR sample from [13]. The ACAR grains were obtained in a hydrogen-free medium; i.e., they are hydrogen-depleted, like the atmospheres and corresponding envelopes of R CrB stars. This makes them well suited as model dust grains for the envelopes of this type of star. The computed diameter of the inner boundary of the dust envelope was $d_{in,e} \approx 80 D_*$ ($\theta_{in,e} \approx 38$ arcsec).

We can see in Fig. 1 that the star's visibility curve at the spatial frequencies of the 6-m telescope and IOTA interferometer (which we will refer to as low, $q \leq 15$ arcsec^{-1}, and intermediate, $q = 45$–65 arcsec^{-1}, frequencies) is a straight horizontal line. Its amplitude is determined by the star's relative contribution to the corresponding spectral band, which is the K band, in our case. In October 1996, the IR excess was close to its mean value, and the star contributed $\sim 48\%$ of the K-band brightness (Fig. 1). The star's contribution in various bands was estimated in the same way as in [7].

Thus, the computed visibility curve must satisfy two conditions: it must reproduce the observed visibility curve at low frequencies and the star's relative contribution at sufficiently high frequencies, where the contribution of the extended IR source is already negligible but the star remains an unresolved point source. The computed curve does satisfy these conditions (Fig. 1). We can see from Fig. 1 that the visibility curve of the extended dust envelope already ceases to contribute appreciably to the visibility curve of R CrB at the intermediate frequencies. This visibility curve thus forms a wave with decreasing amplitude that "winds around" the star's visibility curve.

The IR excess in June 2001 was close to its maximum value (see the L light curve of R CrB in [7]). Thus, the star's contribution was lower at this epoch than in October 1996 and was ∼38% in the K band. Accordingly, the visibility curve of R CrB in this band for model 1 should be 0.38 ± 0.03 at intermediate frequencies. However, the observed visibility curve was 0.61 ± 0.03 (Fig. 1).

Thus, there is a considerable discrepancy between the computed (for model 1) and observed visibility curves, which considerably exceeds the observational errors and the uncertainties in the estimates of the star's contribution (shown in Fig. 1). We were able to remove this discrepancy by adding a third IR source that was more compact than the extended IR source to the model. This source will increase the visibility curve of R CrB at intermediate frequencies. At appreciably higher frequencies (for example, by an order of magnitude), its contribution will already be negligible, and the visibility curve should correspond purely to the star's contribution. At even higher frequencies, the visibility curve will begin to decrease (the star becomes spatially resolved), reaching zero at a spatial frequency of ∼2500 arcsec^{-1}.

3. FORMULATION OF THE PROBLEM

One of the most important features of the compact IR source is that its near-IR color indices differ little (if at all) from those of the extended IR source. The source therefore cannot be detected from an analysis of the SED of R CrB. Accordingly, we can refer to it as a warm source, like the extended IR source.

The fact that the compact source is warm follows directly from the IOTA JH observations. R CrB was unresolved in the J band; this means that this band is dominated by the star's radiation and that the envelope does not contain a hot clump of dusty material that contributes appreciably to the brightness in this band.

The star contributed ∼81% of the H brightness of R CrB in June 2001, which is equal to the H visibility curve within the observational errors (0.78 ± 0.06). This means that the H visibility curve can be reproduced by model 1. However, this cannot be achieved in the K band, necessitating the introduction of an additional compact source to the model to increase the visibility curve at intermediate frequencies. This increase will be observed in all bands. The hotter the compact IR source, the more it will add to the H visibility curve, increasing the discrepancy between the computed and observed values. Therefore, the compact IR source cannot be hot.

We associate this compact IR source with the radiation from a group of dust clouds. If these are filled with fine grains similar to those in the extended dust envelope, the compact IR source will be considerably hotter than the extended source [7], leading to a disagreement between the computed and observed SEDs and the H visibility curve. The reason the dust clouds are warm rather than hot is unclear. For example, this may be related to the grain size; it was demonstrated in [7] that the grains in the cloud obscuring the star in 1999 were large ($a_{gr} > 0.1$ μm).

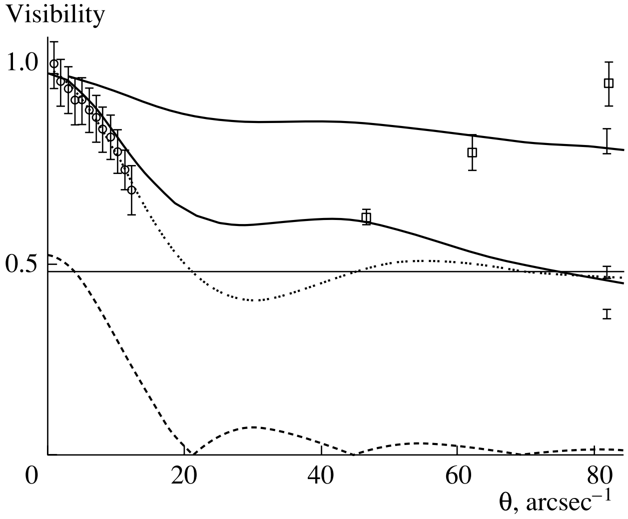

Fig. 1. Visibility functions of R CrB in the K band on October 1, 1996 (circles), and in the JHK bands on June 5, 2001 (squares). The dotted curve is the computed model visibility curve for October 1996. The long-dashed and short-dashed curves show the visibility curves of the star and the extended dust envelope. The solid curves are the H (upper) and K (lower) computed visibility curves for June 2001. The vertical bars show the contribution of the star to the K brightness of R CrB in June 2001 and in October 1996 and to the H brightness in June 2001 (if they are counted from the bottom upward).

In the absence of specific information about the structure and physical properties of dust clouds, they are usually represented as blackbodies in model computations in order to obtain at least reasonable estimates of their parameters. We have done this, since it is unclear why the clouds are warm and their spatial distribution is unknown. We represented the compact IR source as a dust layer centered on the star and filled with blackbody dust grains.

The dust layer is described by its inner diameter ($d_{in,c}$), the grain temperature at its inner boundary, its optical depth at $\lambda = 5500$ Å ($\tau_c(V)$) (and the fraction of the star's bolometric flux it absorbs), and its relative contribution to the bolometric flux of the IR excess and to its K flux. Since the optical depth of an individual cloud varies as $\tau \propto r^{-2}$, we assumed that the dust density distribution varies as $\rho \propto r^{-3}$. The parameter $d_{in,c}$ gives an estimate of the size of the compact source, while $\tau_c(V)$ provides an estimate of the fraction of the sphere around the star that is

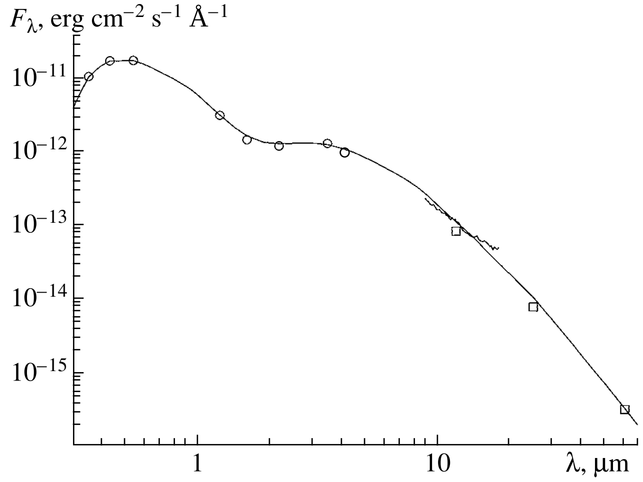

Fig. 2. SED of R CrB on June 10, 2001 (circles). The solid curve is the computed SED. See text for more details.

covered by the clouds if most of them are optically thick. Note also that this model for the compact IR source successfully reproduces the situation when most clouds are optically thin (transparent). Such clouds cause slight but fairly frequent dimmings of the star with no variations of $B-V$ [14]. The neutral extinction in the optical means that the grain size exceeds 0.1 μm.

The modeling of the extended dust envelope and the SED of the star is described in [7]. We adopted the distance to the star presented in that paper, ∼1.44 kpc. A detailed description of the input parameters for the model computations can be found in [15], which also describes the model parameters that are independent of input parameters, such as the star's bolometric luminosity. These include, in particular, the angular size of the dust envelope's inner boundary ($\theta_{in,e}$) and, if the shape of the SED is preserved, the ratio $d_{in,e}/D_*$. We computed the SED for our three-component model using a modified version of the CSDUST3 code [16].

4. COMPUTATIONAL RESULTS

Figure 1 shows the IOTA visibility curve and the HK visibility curves computed in the best of our models. Figure 2 displays the observed and computed June 2001 SEDs for R CrB. The fluxes at 12, 25, 60, and 100 μm were taken from [15], and the low-resolution spectrum at 8–22 μm, from the SDC data base. These data were obtained by the IRAS space observatory in September 1983; we corrected them in accordance with the relative L brightnesses of R CrB in September 1983 and June 2001 [7].

The total optical depth of the two dust envelopes was $\tau(V) \approx 0.5$, distributed in the ratio 1 : 6 between the compact and extended dust envelopes, for which $\tau_c(V) \approx 0.07$ and $\tau_e(V) \approx 0.43$, respectively. Thus, the group of dust clouds observed in 2001 absorbed ∼7% of the star's light. Its contribution to the bolometric flux of the IR excess of R CrB is 14% and, in the K band, 7%. If the dust clouds are predominantly optically thick, they covered ∼7% of the surface of the sphere around the star.

The diameter of the inner boundary of the compact dust envelope, which we identify with the size scale of the compact IR source, was $d_{in,c} \approx 13.5D_*$ ($\theta_{in,c} \approx 6.4$ mas), whereas the inner diameter of the extended dust envelope was $d_{in,e} \approx 90D_*$ ($\theta_{in,e} \approx$ 43 mas). The color temperature of the blackbody radiation from the group of dust clouds was ∼1150 K. The temperature of the blackbody (i.e., the large) dust grains at the inner boundary of the dust envelope was ∼1350 K, whereas the fine grains could have a temperature of ∼1900 K.

5. CONCLUSIONS

Our joint analysis of interferometric JHK observations of R CrB with a baseline of 21.18 m and of $UBVJHKLM$ photometric observations has revealed the presence of an IR source that is more compact than the IR source associated with the extended dust envelope ($\theta_{in,e}/\theta_{in,c} \approx 6.7$). This compact IR source, which we interpret as the radiation from a group of dust clouds, appreciably influences the K visibility curve of R CrB at intermediate spatial frequencies but has little effect in the H band. Consequently, as was expected from IR photometry of R CrB and many other stars of this type, the group of clouds viewed as an integrated source of radiation contributing to the IR excess has a color temperature that exceeds only slightly (in this case, by ∼300 K) the color temperature of the extended dust envelope.

ACKNOWLEDGMENTS

The author is grateful to the referee for helpful remarks. This study was supported by the Russian Foundation for Basic Research (project code 02-02-16235).

REFERENCES

1. G. C. Clayton, Publ. Astron. Soc. Pac. **108**, 225 (1996).
2. Yu. Fadeyev, Mon. Not. R. Astron. Soc. **233**, 65 (1988).
3. W. A. Stein, J. E. Gaustad, F. C. Gillett, and R. F. Knacke, Astrophys. J. **155**, L3 (1969).
4. W. J. Forrest, F. C. Gillett, and W. A. Stein, Astrophys. J. **178**, L129 (1972).
5. D. W. Strecker, Astron. J. **80**, 451 (1975).
6. M. W. Feast, B. S. Carter, G. Roberts, *et al.*, Mon. Not. R. Astron. Soc. **285**, 317 (1997).
7. V. I. Shenavrin, J. D. Ferni, G. Vaigelt, and B. F. Yudin, Astron. Zh. **79**, 894 (2002) [Astron. Rep. **46**, 805 (2002)].
8. K. Ohnaka, Y. Balega, T. Blocker, *et al.*, Astron. Astrophys. **380**, 212 (2001).
9. C. Rogers and P. G. Martin, Astrophys. J. **284**, 327 (1984).
10. K. Ohnaka, U. Beckmann, J. P. Berger, *et al.*, in *Interferometry for Optical Astronomy II*, Ed. Wesley A. Traub; Proc. SPIE **4838**, 1068 (2003).
11. M. W. Feast, Mon. Not. R. Astron. Soc. **285**, 339 (1997).
12. C. Jager, H. Mutschke, and T. Henning, Astron. Astrophys. **332**, 291 (1998).
13. L. Colageli, V. Mennella, P. Palumbo, *et al.*, Astron. Astrophys., Suppl. Ser. **113**, 561 (1995).
14. J. D. Fernie and W. A. Lawson, Mon. Not. R. Astron. Soc. **265**, 899 (1993).
15. B. Yudin, Y. Balega, T. Blocker, *et al.*, Astron. Astrophys. **379**, 229 (2001).
16. M. P. Egan, C. M. Leung, and G. F. Spagna, Comput. Phys. Commun. **48**, 271 (1988).

Translated by N. Samus'

Astronomy Reports, Vol. 48, No. 4, 2004, pp. 332–336. Translated from Astronomicheskiĭ Zhurnal, Vol. 81, No. 4, 2004, pp. 365–369.
Original Russian Text Copyright © 2004 by Gorbatskiĭ.

Thermal Instability in the Envelopes of Wolf–Rayet Stars

V. G. Gorbatskiĭ

St. Petersburg State University (Petrodvorets Branch), Universitetskiĭ pr. 2, Petrodvorets, 198904 Russia

Received May 14, 2003; in final form, August 8, 2003

Abstract—We briefly consider thermal instabilities developing in the expanding envelopes of Wolf–Rayet stars and their possible implications. Due to the specific physical conditions in the gaseous outflow from the star, thermal instabilities are likely to be very important in determining the flow's structure. *© 2004 MAIK "Nauka/Interperiodica".*

1. INTRODUCTION

Processes occurring in gas flowing from a star and forming a so-called envelope are essential for our understanding of the evolution of the interstellar medium (ISM). The primary structural elements from which the Galactic ISM is ultimately formed are produced in stellar envelopes. These elements can originate as condensations in the gas flowing from the star. Evidence for the existence of such condensations ("clouds") have been found in the envelopes of Be stars [1], Wolf–Rayet (WR) stars [2] and red giants [3]. Stellar envelopes with condensations have been modeled in a number of studies. However, the conditions leading to the formation of inhomogeneities in gas envelopes remain unclear. The presence of some kinds of instabilities in the envelopes is often assumed, although no self-consistent theory for their development has been suggested.

The formation of cloud structures in stellar envelopes may be related to the structure of the subphotospheric layers of the corresponding stars. This is probably true of red giants, with their extended convective zones. The inhomogeneity of the velocity field observed in the atmospheres of such stars is an unavoidable consequence of convective motions.

The atmospheres of Be stars are characterized by rapid rotation and the presence of strong magnetic fields. Along with other factors, this may result in inhomogeneity of their envelopes, but the theory of processes occurring in envelopes is not well enough developed to create specific models to compare with observations.

In the case of the envelopes of WR stars, there is no basis to consider magnetic fields and/or convective motions important in the creation of inhomogeneities in the envelope gas. For a long time, the gaseous outflows from these stars were represented as steady-state, spherically symmetrical gas streams whose physical parameters at each point—density, temperature, and velocity—depended only on the distance from the center of the star. Improved photometric and spectral observations have made it possible to detect certain features in the envelope radiation that have been taken as evidence for the existence of clouds on various scales. It is usually supposed in models of the structure of the gaseous outflows that these clouds are embedded in a quasi-homogeneous, high-velocity flow from the center of the star.

The temperatures in the envelopes of WR stars are very high, of the order of 10^5 K. The envelope gas is characterized by a low abundance of hydrogen compared to helium ($\mathrm{H/He} \lesssim 0.1$). We show here that both these characteristics of the envelopes of WR stars should result in thermal instability, which may provide one path for the formation of condensations and chaotic motions in the gas.

2. WR STARS AND THEIR ENVELOPES

The objects constituting the relatively small group of WR stars are distinguished by their very high luminosities ($L_* \gtrsim 10^{38}$ erg/s) and peculiar spectra, dominated by very broad (50–100 Å) emission lines of H I, He I, He II, C II, C III, C IV, N II, N III, and other elements in various ionization states. The emission lines are formed via fluorescence, and their widths are due to the high expansion velocity of the envelope, commonly considered to be the result of radiation pressure.

WR stars display high mass-loss rates ($\dot{\mathfrak{M}}_* \approx 10^{-5}\mathfrak{M}_\odot$/year), making this evolutionary stage very short. This has increased interest in studies of WR stars in recent years. The low hydrogen abundance in their atmospheres is also related to their evolution. There are two sequences of WR stars, with their spectra dominated by nitrogen emission lines (WR N) or carbon lines (WR C). The following discussion will refer primarily to WR N stars.

1063-7729/04/4804-0332$26.00 © 2004 MAIK "Nauka/Interperiodica"

Studies of the spatial and dynamical structure of the outer layers of WR stars are complicated by the opacity of the deep layers of the extended envelopes of these stars. It is generally assumed that the radius R of the "surface" of a star is the radius of a sphere corresponding to optical depth $\tau = 1$. Since τ depends on frequency, this value is to some degree arbitrary.

One of the most thoroughly studied WR stars is V444 Cyg, a component of a close binary. The parameters of its core ($R_C \approx 2.6R_\odot, T_C \approx 10^5$ K) and envelope were derived with relatively high accuracy from observations during eclipses (see [4] and later studies).

The gas density at the core level in V444 Cyg is $\rho|_{r=R_c} \approx 5 \times 10^{-11}\mathrm{cm}^{-3}$, the helium density is $n_{\mathrm{He}} \gg n_{\mathrm{H}}$, the free-electron density is $n_e|_{r=R_c} \approx 10^{13}\mathrm{cm}^{-3}$, and the expansion velocity of the envelope at this level is $v|_{r=R_c} \approx 300$–400 km/s. These data are fairly typical for WR N stars.

3. DE-EXCITATION FUNCTION FOR THE HELIUM MEDIUM

A region occupied with a gaseous medium ("a system") is in a state of thermal equilibrium if, at each point and at any time, the outflow of thermal energy $\mathfrak{L}^-$ is balanced by the energy inflow $\mathfrak{L}^+$, i.e., if

$$\mathfrak{L}^-(\rho_0, T_0) - \mathfrak{L}^+(\rho_0, T_0) \equiv \mathfrak{L}(\rho_0, T_0) = 0, \qquad (1)$$

where ρ_0 and T_0 are the density and temperature of the gas at the given point. If a small variation of one or more of the values $(\rho_0, T_0) \to (\rho_1, T_1)$, $\mathfrak{L}(\rho_1, T_1) \neq 0$ occurs and increases with time, local thermal instability arises in the system, which should evolve to a stationary state (ρ_2, T_2) such that $\mathfrak{L}(\rho_2, T_2) = 0$. The evolution of the state of the gas and of the parameters of its final state depend on the initial state and the type of perturbation.

Assuming that the gas pressure in the system is constant ($P = \mathrm{const}$), even when the state varies (the isobaric case), the medium will be unstable when

$$\left.\frac{\partial \mathfrak{L}(\rho, T)}{\partial T}\right|_P < 0. \qquad (2)$$

Physically, this condition is rather simple. If the amount of convective heat transfer in the system decreases with increasing temperature, the gas should be further heated, resulting in even higher temperatures and, consequently, in a decrease in the density. If the system is in a state of unstable equilibrium, a decrease in temperature will result in an increase in the convective heat transfer, and the medium will undergo further cooling.

This approach was used in [5] to investigate the state of a homogeneous medium whose chemical composition corresponded to the composition of interstellar gas heated by X rays or cosmic rays. When nT, which is proportional to the pressure, was calculated as a function of the temperature for a medium with Galactic chemical composition, zones of instability were found to be located between two regions (ρ, T) in which the medium was stable. Due to the instability, the medium should separate into two phases, with $T \approx 5000$ K and $T \approx 50$ K. This study also suggested that this separation of the medium results in the observed cloudy structure of the ISM. Later observations indicated that the interstellar molecular clouds are secondary structures; i.e., they are formed from gas ejected from stars, and the real process with which structure is imparted to the ISM is much more complex.

The transition from an unstable state of the system with (ρ_1, T_1) to a stable state with (ρ_2, T_2) is described by a system of gas dynamical equations. The energy equation contains the function $\mathfrak{L}(\rho, T)$, which is specified by sources of gas heating and the physics of various microprocesses—interactions between atoms, ions, electrons, and radiation. It is generally assumed that the medium is transparent to radiation, at least within some frequency intervals, and that the outflow of energy is via the radiation emitted by atoms and ions excitated by collisions with free electrons. In addition, radiation is emitted in recombinational (free–bound, "fb"), free–free ("ff"), and two-photon ("2ph") transitions. When the medium consists of only one element and its density is n, $\mathfrak{L}^-(\rho, T)$ can be written in the form

$$\mathfrak{L}^- = n^2 \Lambda(T), \qquad (3)$$

where $\Lambda(T)$ is the so-called de-excitation function:

$$\Lambda(T) = \sum_z \sum_j \Lambda_z^j + \Lambda_{fb} + \Lambda_{ff} + \Lambda_{2ph}. \qquad (4)$$

The summation in (4) is over all ionization states of the atoms and all excitated levels j. If the gas consists of more than one element, $\mathfrak{L}^-$ is combined from the values determined from (4) for each element and weighted according to the elemental abundances. Expression (4) is called the partial de-excitation function.

Further, we will use the partial de-excitation function for a helium medium. This has been calculated many times; the figure presents the results of recent calculations in an isochoric approximation [6]. $\Lambda(T)$ was calculated at individual points; the values of T are spaced by 0.1 on a logarithmic scale. To avoid interpolation, we will use in place of $\Lambda(T)$ the approximation

$$\Lambda(T) = \Lambda(T_m) e^{-5\left(\frac{T_m - T}{T}\right)^2}, \qquad (5)$$

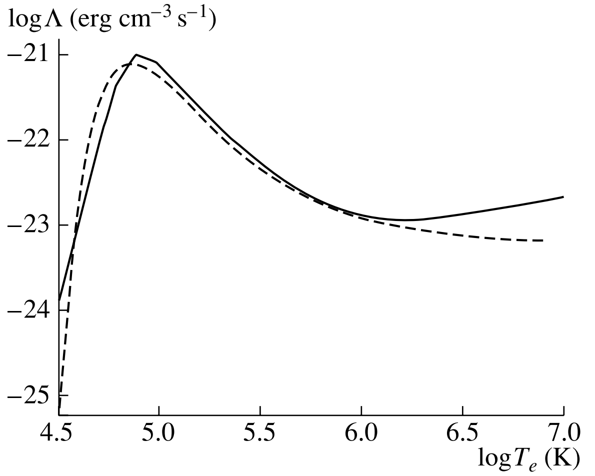

Partial de-excitation function for helium as a function of temperature. The solid curve presents the calculations of [6], and the dotted curve, the $\Lambda(T)$ approximation (5).

which, for $T_m = 7.5 \times 10^4$ K, is consistent with calculations in the broad temperature interval $3.5 \times 10^4 \lesssim T \lesssim 10^6$ K (see the figure). Note that the calculated function is close to the isobaric function calculated in [7].

When the presented calculated values of $\Lambda(T)$ are compared with the thermal-instability condition (2), it is obvious that pure helium is unstable at temperatures of 8×10^4–10^6 K for a constant $\mathfrak{L}^+$, while it is stable for $T \lesssim 7 \times 10^4$ K. This conclusion is also consistent with the dependence between the stability of the gas and its degree of ionization. In highly ionized gas, the ionization energy constitutes a substantial part of the internal energy. This substantially affects the stability of the gaseous medium. For a degree of ionization of the atoms of $\chi \equiv n_{\rm H}^+/n_{\rm H} \approx 0.9$, pure hydrogen gas remains stable until $T < 17.5 \times 10^4$ K [8]. If $\mathfrak{L}^+$ does not vary with time, the outflow of thermal energy due to de-excitation is partially compensated by the ionization energy. $\mathfrak{L}^- - \mathfrak{L}^+$ can become positive only after this compensation becomes insufficient.

The content of the ionization energy in ionized helium is higher than in a hydrogen medium; therefore, the critical temperature below which the gas remains stable should be higher than that for hydrogen. The internal energy in a unit volume of helium U is specified by the expression

$$U = \frac{3}{2}k\left[n_eT_e + nT_i\right] + n_{\rm He\,II}\chi_1 + n_{\rm He\,III}\chi_2, \quad (6)$$

where T_e and T_i are the kinetic temperatures of the electrons and helium in all their states, $(n_{\rm He\,I}, n_{\rm He\,II}, n_{\rm He\,III})$,

$$n = n_{\rm He\,I} + n_{\rm He\,II} + n_{\rm He\,III}, \quad (7)$$

and χ_1 and χ_2 are the ionization potentials of He I and He II from the ground state. Since only electrons play an active role in the excitation of the medium and its ionization, while heavy particles represent only a "reservoir" of thermal energy, generally speaking, $T_e \neq T_i$.

Calculations of the critical temperature $T_{\rm cr}$ for the onset of instability of a hydrogen–helium medium [9] indicate that $T_{\rm cr}$ increases with the helium abundance in the medium and that $T_{\rm cr} = 31\,600$ K for $n_{\rm He}/(n_{\rm H} + n_{\rm He}) = 0.2$. For $n_{\rm H} = 0$ (pure helium), $T_{\rm cr} = 45\,000$ K. This latter value is probably substantially underestimated, since it was assumed in the calculations that only the term $n_{\rm He\,III}\chi_2$ was important in (6) and the energy corresponding to $n_{\rm He\,II}\chi_1$ was not included. An estimate of the resulting error implies that, for pure helium, the temperature $T_{\rm cr}$ should be (2.0–2.5)10^4 K higher and close to the value for T_m derived from calculations of $\Lambda(T)$; i.e., $T_{\rm cr} \approx 7 \times 10^4$ K.

4. TRANSITION OF THE HELIUM MEDIUM TO A STABLE STATE

The function $\Lambda(T)$ for helium is distinguished by the presence of a maximum at $T_m \approx 75\,000$ K, which makes it possible for two regions where the gas can be in a state of equilibrium to exist when $\mathfrak{L}^+ = $ const. In one, with $T < T_m$, the gas state is stable. In the other, with $T > T_m$, the thermal equilibrium turns out to be unstable. As a result, even a small perturbation should lead to a transition of the gas to a stable equilibrium. The kinetics of this transition are described by equations specifying the variations of the electron (T_e) and ion (T_i) temperatures and the degree of ionization of the atoms.

During the transition to the stable state, for which $T < T_m$, the decrease in the energy of the heavy particles follows the variation of the energy of the free electrons; therefore, $T_e < T_i$. The thermal energy per unit volume of the gas is

$$E_{\rm therm} = \frac{3}{2}k\left(n_eT_e + nT_i\right), \quad (8)$$

where n is specified by (7) and the gas pressure is $P = \dfrac{2}{3}E$.

The time variation of $E_{\rm therm}$ in an isochoric approximation is specified by the equation

$$\frac{dE_{\rm therm}}{dt} = \mathfrak{L}^+ - \mathfrak{L}^-. \quad (9)$$

Assuming the process to be isobaric,

$$\frac{dE_{\rm therm}}{dt} = \frac{5}{3}E_{\rm therm}\frac{1}{n}\frac{dn}{dt} + \mathfrak{L}^+ - \mathfrak{L}^-. \quad (10)$$

Heavy particles transfer an energy E_{ie} to electrons per unit time, which for $n_{\mathrm{He\,I}} \ll n_{\mathrm{He\,II}} + n_{\mathrm{He\,III}}$ is approximately [10]

$$E_{ie} \approx 10^{-18} T_e^{-3/2} (T_i - T_e) n n_e. \quad (11)$$

The rate of variation of T_i is given by the relation

$$\frac{d\left(\frac{3}{2} n k T_i\right)}{dt} = -E_{ie}, \quad (12)$$

while, using (8), (10), and (12), the equation for the electron temperature (for the isobaric case) can be written as

$$\frac{d\left(\frac{3}{2} n k T_i\right)}{dt} \quad (13)$$

$$= E_{ie} - \frac{5}{2}\left\{k\left(nT_i + n_e T_e\right)\frac{d\ln n}{dt} + \mathfrak{L}^{+} - \mathfrak{L}^{-}\right\}.$$

Here, we have not taken into account the variation of the molecular weight μ with time, which may introduce errors; however, these errors are smaller than the uncertainty in the factor adopted in (11), up to 50%. The isochoric nature of the process requires that $d\ln n/dt = 0$. The time variation of the degree of ionization of the gas can be found from the equations

$$\frac{dn_{\mathrm{He\,I}}}{dt} = C_{\mathrm{He\,I}}(T_e) n_e n_{\mathrm{He\,I}} - b_{\mathrm{He\,I}}(T_e) n_e n_{\mathrm{He\,I}}, \quad (14)$$

$$\frac{dn_{\mathrm{He\,II}}}{dt} = C_{\mathrm{He\,II}}(T_e) n_e n_{\mathrm{He\,II}} \quad (15)$$

$$+ b_{\mathrm{He\,I}}(T_e) n_e n_{\mathrm{He\,I}} - b_{\mathrm{He\,II}}(T_e) n_e n_{\mathrm{He\,II}}.$$

Here, $C_{\mathrm{He\,I}}(T_e)$ and $C_{\mathrm{He\,II}}(T_e)$ denote the total recombination coefficients (to all levels), while $b_{\mathrm{He\,I}}(T_e)$ and $b_{\mathrm{He\,II}}(T_e)$ are the collisional-ionization coefficients. For $T \approx 10^5$ K and $n_{\mathrm{He\,III}} > n_{\mathrm{He\,II}} \gg n_{\mathrm{He\,I}}$, bound–bound transitions cannot play an important role in the interactions of electrons with heavy particles.

Supplemented by the obvious relation

$$n_e = n_{\mathrm{He\,II}} + 2n_{\mathrm{He\,III}}, \quad (16)$$

equality (7), and the specified initial conditions, system of equations (12)–(15) fully describes the transition from the state corresponding to $T_1 > T_m$ to an equilibrium state for which

$$T_e = T_i = T_2 < T_m \quad \text{and} \quad \mathfrak{L}(T_2) = \mathfrak{L}(T_1). \quad (17)$$

In addition, in this state,

$$\frac{dn_{\mathrm{He\,I}}}{dt} = 0, \quad \frac{dn_{\mathrm{He\,II}}}{dt} = 0.$$

It follows from (17) that, in an isobaric approximation,

$$\Lambda(T_1)\frac{n_1^2}{n_2^2} = \Lambda(T_2). \quad (18)$$

Assuming the process is isochoric, $\Lambda(T_1) = \Lambda(T_2)$.

Using the approximate expression (5) for $\Lambda(T)$, we obtain from (17) the following relation between T_1 and T_2:

$$\frac{T_m}{T_2} = 2 - \frac{T_m}{T_1}, \quad (19)$$

which indicates that T_2 is always in the region of stability.

In the case of an isobaric process, the relation between T_1 and T_2 is derived from (18) and has the more complex form

$$\left(\frac{T_m - T_2}{T_2}\right)^2 - \left(\frac{T_1 - T_m}{T_1}\right)^2 + \frac{1}{5}\ln\frac{T_2}{T_1} = 0. \quad (20)$$

For any $T_1 > T_m$, the solution of (20) for T_2 yields values smaller than are obtained assuming the process is isochoric. For this T_2, the gas density exceeds its initial value by a factor of T_1/T_2. For example, for $T_1 = 10^5$ K and $n = \mathrm{const}$, $T_2 = 6 \times 10^4$ K, whereas, assuming $P = \mathrm{const}$, we obtain $T_2 \approx 5 \times 10^4$ K and, hence, $n = 2$. Thus, as the instability develops, the gas becomes inhomogeneous and condensations begin to form in it.

These condensations form if a perturbation is accompanied by a decrease in the initial temperature of the gas T_1. When a perturbation has $\delta T_1 > 0$, condition (2) for $\mathfrak{L}^{+} = \mathrm{const}$ is fulfilled and the temperature decrease should continue. This possibility seems unlikely, since, for large T, de-excitation of the medium is determined by the presence of other elements in the stellar envelope, in particular, N and O, which determine to a considerable extent the gas de-excitation for temperatures of the order of 3×10^7 K and higher.

5. CONCLUSION

Our conclusions concerning the development of local thermal instabilities in a helium envelope have been obtained assuming that the unperturbed gas has a homogeneous density and that the sources of heating are independent of the state of the gas and of time. The possibility that this process can be realized in the envelopes of WR N stars depends, in particular, on the extent to which it is affected by the expansion of the envelope. This question can only be clarified via computations, which have already been begun.

If thermal instabilities do arise in the envelopes of WR stars, their effect should be reflected in various observed spectral features. One of the observational facts related to gas instability may be the simultaneous presence of He I and He II emission lines in the spectra of WR stars. As was shown in [2], this cannot be due to stratification of the radiation. When the temperature exceeds 8×10^4 K, helium is primarily in the He III state, while it is predominantly He II when $T < 7 \times 10^4$ K. When $T \approx (7–8) \times 10^4$ K, both states occur and $n_{\mathrm{He\,III}} \approx n_{\mathrm{He\,II}}$.

The thermal instability of the gas may also affect dynamical parameters of the stellar envelope. Calculations indicate [11] that thermal instability in a homogeneous interstellar medium results in the formation of a multiphase state and the development of chaotic motions. In this case, 1–2% of the thermal energy should be transformed into energy of gas motions. Such studies could also be of interest for our understanding of stellar envelopes.

REFERENCES

1. V. G. Gorbatskiĭ, Pis'ma Astron. Zh. **1**, 36 (1975) [Sov. Astron. Lett. **1**, 62 (1975)].
2. I. I. Antokhin, A. F. Kholtygin, and A. M. Cherepashchyuk, Astron. Zh. **65**, 558 (1988) [Sov. Astron. **32**, 285 (1988)].
3. P. A. Crowther, Astron. Astrophys. **356**, 191 (2000).
4. A. M. Cherepashchyuk and Kh. F. Khaliullin, Astron. Rep. **52**, 121 (1975) [Sov. Astron. **19**, 727 (1975)].
5. S. B. Pikel'ner, Astron. Zh. **44**, 915 (1967) [Sov. Astron. **11**, 737 (1967)].
6. A. F. Kholtygin, B. F. Brattsev, and V. I. Ochkur, Astrofizika **45**, 45 (1999).
7. A. B. Kirienko, Pis'ma Astron. Zh. **19**, 401 (1993) [Astron. Lett. **19**, 11 (1993)].
8. T. Yoneyama, Publ. Astron. Soc. Jpn. **25**, 349 (1973).
9. A. V. Shamraĭ, Diplom (M. S. Equivalent) (St. Petersburg, 1996).
10. S. B. Pikel'ner, Izv. Krymsk. Astrofiz. Obs. **12**, 93 (1954).
11. A. G. Kritsuk and M. L. Norman, Astrophys. J. **569**, L127 (2002).

Translated by K. Maslennikov

Astronomy Reports, Vol. 48, No. 4, 2004, pp. 337–341. Translated from Astronomicheskiĭ Zhurnal, Vol. 81, No. 4, 2004, pp. 370–374.
Original Russian Text Copyright © 2004 by Malov.

A Spindown Mechanism for Short-Period Radio Pulsars

I. F. Malov

Astro Space Center, Lebedev Institute of Physics, Russian Academy of Sciences, Profsoyuznaya ul. 84/32, Moscow, 117997 Russia

Received July 15, 2001; in final form, November 10, 2003

Abstract—It is shown that a model with accretion in a "quasi-propeller" mode can explain the observed spindown of pulsars with periods $P < 0.1$ s. The mean accretion rate for 39 selected objects is $\dot{M} = 5.6 \times 10^{-11} M_\odot$/year. If $\dot{M}$ is constant during the pulsar's lifetime, the neutron star will stop rotating after 10^7 years. The mean magnetic field at the neutron-star surface calculated in this model, $\bar{H}_0 = 6.8 \times 10^8$ G, is consistent to an order of magnitude with the values of H_0 for millisecond pulsars from known catalogs. However, the actual value of H_0 for particular objects can differ from the catalog values by appreciable factors, and these quantities must be recalculated using more adequate models. The accretion disk around the neutron star should not impede the escape of the pulsar's radiation, since this radiation is generated near the light cylinder in pulsars with $P < 0.1$ s. Pulsars such as PSR 0531+21 and PSR 0833−45 have probably spun down due to the effect of magnetic-dipole radiation. If the difference in the braking indices for these objects from $n = 3$ is due to the effect of accretion, the accretion rate must be of the order of 10^{18} g/s.

1. INTRODUCTION

Throughout the time radio pulsars have been studied, it has been thought that the main mechanism slowing the neutron star's rotation is magnetic-dipole radiation. This process leads to the time dependence for the increase in the period

$$\dot{P} \propto P^{-1} \tag{1}$$

if the pulsar magnetic field remains constant. However, we showed in [1] that it is not possible to describe all the collected observational data on a $\dot{P} - P$ plot using formula (1) alone, and other mechanisms for the loss of angular momentum must be taken into account. We also found that the location of pulsars with $P < 0.1$ s on the $\dot{P} - P$ plot cannot be explained by any of the mechanisms considered in [1] associated with processes inside the neutron star or in its magnetosphere. For 41 pulsars from the catalog [2] with such short periods and measured positive values of $\dot{P}$, the $\dot{P}(P)$ dependence can be described by the relation

$$\log \dot{P} = (3.32 \pm 0.46) \log P + 3.54 \pm 0.94, \tag{2}$$

where the $\log \dot{P} - \log P$ correlation coefficient is $\rho = 0.76 \pm 0.10$.

In this paper, we suggest that relationship (2) can be explained by the accretion of material onto the neutron star from a surrounding disk.

2. MODEL. RESULTS

Of the 41 pulsars with $P < 0.1$ s used to derive (2), 25 objects are members of binary systems. We expect the presence of accreting material in such systems, either associated with a wind from the companion or remaining after the formation of the system. Assuming that most of the remaining short-period pulsars were also formed in binary systems and became single objects after their decay, there may exist relic disks around such neutron stars. The 41 pulsars with $P < 0.1$ s can also include some objects that were formed as single neutron stars. The Crab (PSR 0531+21) and Vela (PSR 0833−45) pulsars probably belong to this group. Excluding these two pulsars from the sample leaves relationship (2) unchanged within the errors:

$$\log \dot{P} = (2.93 \pm 0.43) \log P + 2.59 \pm 0.91, \tag{3}$$
$$\rho = 0.74 \pm 0.11.$$

Therefore, if the remaining pulsars include other such objects, the results obtained below should not change considerably.

Illarionov and Sunyaev [3] present the following equation describing angular-momentum loss in a regime that is close to a "propeller" mode (when accretion onto the neutron star from the surrounding disk begins):

$$I\Omega \frac{d\Omega}{dt} = -\dot{M} \frac{GM_*}{r_{eq}}, \tag{4}$$

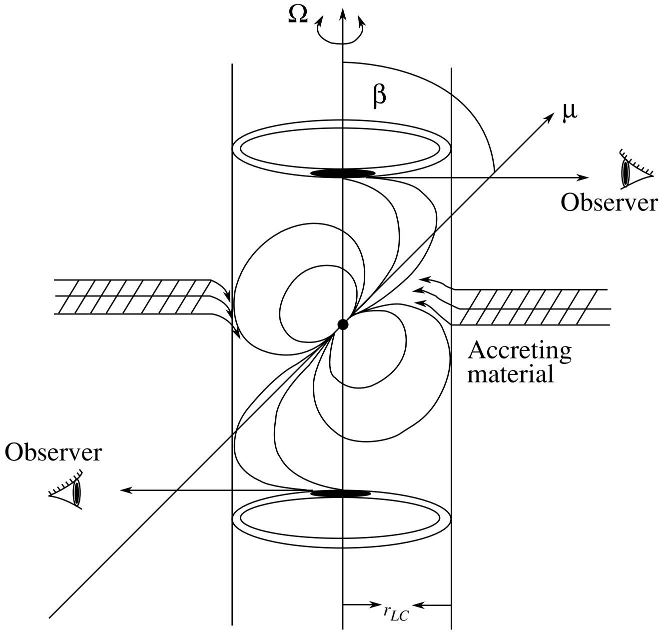

Fig. 1. Schematic of the model; $\boldsymbol{\mu}$ is the magnetic-moment vector and $r_{LC} = c/\Omega$ is the light-cylinder radius.

where $\dot{M}$ is the rate of accretion onto the neutron star, $\Omega = 2\pi/P$, M_* is the mass of the neutron star, I is its moment of inertia, and $r_{eq} = \left(GM_*/\Omega^2\right)^{1/3}$ is the distance at which the rotational velocity is equal to the Keplerian velocity.

In pulsars with periods of $P \leq 0.1$ s, radiation is generated near the light cylinder [4], and the accreting material does not impede it's escape from the magnetosphere (Fig. 1). A similar picture is probably observed in active galactic nuclei and quasars, where material is accreting onto the central body and radiation in different wavebands is observed only in certain directions that are not screened from the observer by the accreting material.

An example of an object of this type is the binary system containing the millisecond pulsar PSR J1740−5340 [5], in which the neutron-star companion has a mass of $\sim 0.2\, M_\odot$ and fills its Roche lobe. In this case, the interaction of the neutron-star magnetosphere and the surrounding material and, consequently, a change in the rotation period due to this interaction are inevitable.

Using the formula for r_{eq}, (4) can be written as

$$\dot{\Omega} = -\frac{\dot{M}(GM_*)^{2/3}}{I\Omega^{1/3}}. \tag{5}$$

The most important implication of this relation is that the braking index n for pulsars with $P < 0.1$ s, found from the relation

$$\dot{\Omega} = k\Omega^n, \tag{6}$$

is $-1/3$; this is consistent with the conclusions of [1], where negative values of n were obtained for this group of objects.

Formula (5) can be expressed in terms of the period and its derivative:

$$\dot{P} = a_1 P^{7/3}, \tag{7}$$

where $a_1 = (\dot{M}/I)\left(GM_*/4\pi^2\right)^{2/3}$. Using the data of [2] yields the most probable value $\log a_1 = -13.10 \pm 1.99$. Adopting the standard values $I = 10^{45}$ g cm^2 and $M_* = M_\odot$, we find that the observations are consistent with an accretion rate of $\dot{M} = 3.53 \times 10^{15}$ g/s $= 5.56 \times 10^{-11}\, M_\odot$/year. If this value of $\dot{M}$ remains constant during the lifetime of the pulsar, the period evolution, described by (7),

$$P = \left(\frac{1}{P_0^{4/3}} - \frac{4a_1 t}{3}\right)^{-3/4}, \tag{8}$$

results in a timescale for complete spindown of the pulsar ($P = \infty$)

$$t = \frac{3}{4a_1 P_0^{4/3}} = \frac{3 \times 10^5 \text{ years}}{P_0^{4/3}}. \tag{9}$$

Setting the initial pulsar period equal to $P_0 = 100$ ms, we find that the rotation ceases after 6.5 million years.

Note that other braking mechanisms can come into operation as the pulsar period increases [1], causing the $P(t)$ dependence to change. It is important for us that the mechanism considered here can work over a sufficiently long time to explain the observed distribution of points in the $\dot{P}(P)$ plot.

As was already noted in [1], the unsuitability of the magnetic-dipole spindown model implies that the pulsar magnetic-field strengths given in published catalogs must be corrected based on the dependences between the pulsar magnetic field H_0 and other parameters using an adequate model. We can use the equality of r_{eq} and the magnetospheric radius at which the accreting material stops to estimate H_0 in our model [3]

$$\left(\frac{2H_0^4R_*^{12}}{\dot{M}^2GM_*}\right)^{1/7}=\left(\frac{GM_*}{\Omega^2}\right)^{1/3}, \qquad (10)$$

from which it follows that

$$H_0=\frac{(GM_*)^{5/6}\dot{M}^{1/2}P^{7/6}}{2^{5/12}\pi^{7/6}R_*^3}. \qquad (11)$$

For $R_*=10$ km, $\dot{M}=3.53\times10^{15}$ g/s, and $\bar{P}=$ 19 ms (for a sample of 39 pulsars), we obtain $\bar{H}_0=$ 6.80×10^8 G, which agrees to order of magnitude with the magnetic-field strengths of millisecond pulsars found for the magnetic-dipole model [2]. However, the value of H_0 for particular objects can differ from the catalog values. For example, for PSR 1257+12, which is in a binary system and has a period of $P=6.22$ ms, the value of $\log H_0$ calculated from formula (11) with the same parameters is 8.27, whereas the value given catalog [2] is $\log H_0=8.93$ and becomes 9.23 after correction by the factor of two discussed in Section 3; i.e., the magnetic field at the pulsar surface differs in these two models by an order of magnitude.

3. CRAB- AND VELA-TYPE PULSARS

As is noted above, some short-period pulsars could evolve outside binary systems, with the main mechanism for their spindown being associated with magnetic-dipole radiation. The magnetic fields of these objects are in no way related to processes in binary systems and are much stronger than the fields in pulsars spun up by interaction with a companion. In particular, the catalog values of $\log H_0$ for PSR 0531+21 and PSR 0833−45 are 12.58 and 12.53, respectively [2].

However, it is possible that, in objects of this type, a certain role is also played by accretion onto the neutron star. In this case, the evolution of the rotational velocity will be described by the combined equation

$$\dot{\Omega}=-\frac{a}{\Omega^{1/3}}-b\Omega^3, \qquad (12)$$

$$a=\frac{\dot{M}(GM_*)^{2/3}}{I}, \qquad (13)$$

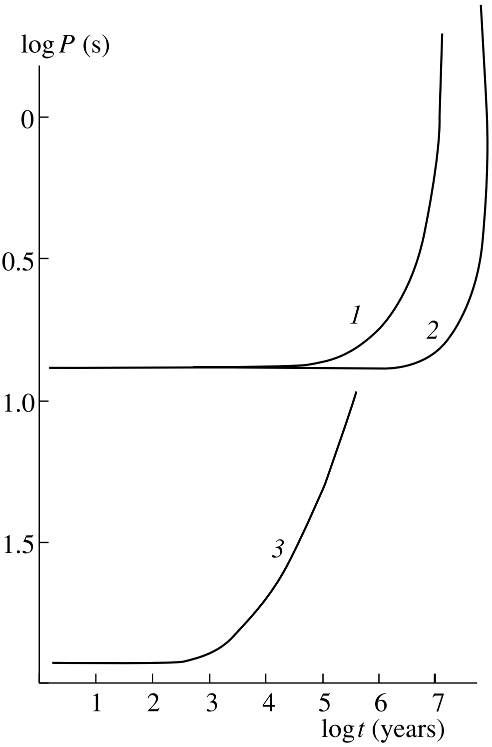

Fig. 2. Period as a function of age for the general case, Eq. (15). See text for details.

$$b=\frac{H_0^2R_*^6\sin^2\beta}{6c^3I}. \qquad (14)$$

Equation (14) takes into account the fact that the pulsar magnetic moment is determined by the expression $\mu=H_pR_*^3/2$, where H_p is the magnetic field at the pole (see, e.g., [6]). Therefore, the catalog values of $H_0\sin\beta$ (β is the angle between the magnetic moment and the rotational axis) should be multiplied by two. The $\log H_0$ values for PSR 0531+21 and PSR 0833−45 are 12.88 and 12.83, respectively.

The solution of (12) has a cumbersome form [7]:

$$-\frac{1}{3}a^{3/5}b^{2/5}t+A=-\frac{1}{10} \qquad (15)$$
$$\times\sum_{k=1}^{5}\cos\frac{2\pi(2k-1)}{5}$$
$$\times\ln\left[1-2y\cos\frac{(2k-1)\pi}{10}+y^2\right]$$
$$+\frac{1}{5}\sum_{k=1}^{5}\sin\frac{2\pi(2k-1)}{5}\arctan\frac{y-\cos\frac{2k-1}{10}\pi}{\sin\frac{2k-1}{10}\pi}.$$

Here, $y=(b/a)^{1/10}\,\Omega^{1/3}$ and A is a constant that is equal to the value of the right-hand side at time $t=0$.

Figure 2 shows the period $P = 2\pi/\Omega$ as a function of the pulsar age for $H_0 \sin\beta = 10^{12}$ G (curves *1* and *3*) and $H_0 \sin\beta = 10^9$ G (curve *2*), based on the solution of (15). Curves *1* and *2* correspond to $\Omega_0 = 62$ s^{-1}, and curve *3*, to $\Omega_0 = 620$ s^{-1}. We can see that, beginning from a certain time, magnetic-dipole spindown becomes the dominant process.

Let us determine the conditions under which (12) will be consistent with the observational data for PSR 0531+21 and PSR 0833−45.

The braking index is defined observationally as

$$n = \ddot{\Omega}\Omega/\dot{\Omega}^2. \tag{16}$$

In our case, it follows from (12) that

$$n = \frac{9\frac{b}{a}\Omega^{10/3} - 1}{3(\frac{b}{a}\Omega^{10/3} + 1)}. \tag{17}$$

Adopting for the neutron-star mass the average value $M_* = 1.35\,M_\odot$ [8], we obtain from (13) and (14)

$$\frac{b}{a} = 1.94 \times 10^{10}\frac{H_{12}^2}{\dot{M}}, \tag{18}$$

where $H_{12} = H_0/10^{12}$.

The braking indices n for the Crab and Vela pulsars are 2.51 and 1.4, respectively [9]. With these n values and the corrected magnetic fields, we can use (17) and (18) to calculate the accretion rate required to explain the observed deviation of n at the present epoch from the magnetic-dipole value, $n = 3$. This yields $|\dot{M}| = 7.7 \times 10^{18}$ g/s for PSR 0531+21 and $|\dot{M}| = 1.2 \times 10^{18}$ g/s for PSR 0833−45.

Future studies will require a detailed analysis of the interactions of these pulsars with the surrounding supernova remnants and with relic presupernova material, as well as investigation of the possible influence of the clumpy structure of the interstellar medium.

4. DISCUSSION. CONCLUSIONS

At present there is no rigorous theory describing the interaction of a magnetized neutron star with the surrounding plasma. Therefore, the estimates obtained in this paper should be treated only as a demonstration of the fundamental possibility of explaining the observed separation of short-period pulsars on the $\dot{P} - P$ plot based on the idea that material is being accreted onto the neutron stars.

The estimated accretion rate $|\dot{M}| \sim 6 \times 10^{-11}\,M_\odot$/year seems reasonable, since stars can lose mass at rates exceeding this value. The mass-loss rates of OB supergiants reach $10^{-6}\,M_\odot$/year [10]. In the case of the weaker winds from T Tauri stars, values of $|\dot{M}| \approx 4 \times 10^{-8}\,M_\odot$/year are typical [11]. Only the solar wind is less intense: $|\dot{M}| \sim 10^{-14}\,M_\odot$/year [12].

Using the formula

$$\dot{M} = 4\pi r^2 N m_H V \tag{19}$$

(where we adopt for the distance r the light-cylinder radius $r_{LC} = cP/2\pi$ and write the velocity of the material as $V = c\alpha$) and supposing that the accreting material consists of atomic hydrogen, we can estimate the density N of this material:

$$N = \frac{\pi}{m_H c^3}\frac{|\dot{M}|}{P^2\alpha}. \tag{20}$$

We obtain for the value $|\dot{M}| = 3.53 \times 10^{15}$ g/s

$$N = \frac{2.5 \times 10^8}{P^2\alpha}. \tag{21}$$

If a disk with density (21) can exist in the vicinity of a neutron star, all the estimates we have obtained are described by the accretion model.

The estimates and arguments presented in this paper lead to the following conclusions.

(1) The $\dot{P} \propto P^{7/3}$ dependence predicted by a model with the accretion of material from a disk onto the neutron star in a mode that is close to a propeller regime is consistent with the observed relationship ($\dot{P} \propto P^{2.93\pm0.43}$) [3]. It is possible that this agreement will become even better if we exclude from the sample pulsars that were formed and evolved as single neutron stars (such as the Crab pulsar, PSR 0531+21, and Vela pulsar, PSR 0833−45).

(2) The best agreement with the observational data in the model considered requires a mean accretion rate $|\dot{M}| = 3.5 \times 10^{15}$ g/s $= 5.6 \times 10^{-11}\,M_\odot$/year, which can be provided by the wind from a companion or material falling in from a relic disk around the neutron star.

(3) If this accretion rate remains constant during the lifetime of the pulsar, the neutron star will spin down on a timescale of the order of 10^7 years (for an initial period of $P_0 \sim 100$ ms). However, we emphasize that other spindown mechanisms could be activated as the pulsar period increases, and the evolution of the period will be described by an equation that differs from (8).

(4) The mean magnetic-field intensity H_0 at the neutron-star surface that is necessary for the operation of the mechanism considered is 6.8×10^8 G, which is of the same order of magnitude as the fields that are usually attributed to millisecond pulsars. In accordance with (11), we must know the accretion rate for a particular pulsar if we wish to calculate H_0 specifically for that pulsar. We again point out that the H_0 values given for pulsars with $P < 0.1$ s in

known catalogs calculated assuming the magnetic-dipole model require correction and should be used only as order-of-magnitude estimates.

(5) We suggest that the effect of accretion can explain the observed values of the braking index for PSR 0531+21 and PSR 0833−45; the accretion rates in these pulsars should reach $\dot{M} = 7.7 \times 10^{18}$ and 1.2×10^{18} g/s, respectively. Estimates show that the effect of the accretion term on the magnitude of the magnetic field is insignificant for these pulsars.

ACKNOWLEDGMENTS

This work was supported by the Russian Foundation for Basic Research (project code 03-02-16509) and the National Science Foundation (grant 00-98685). The author thanks L.B. Potapova for help with the preparation of the manuscript.

REFERENCES

1. I. F. Malov, Astron. Zh. **78**, 452 (2001) [Astron. Rep. **45**, 389 (2001)].
2. J. H. Taylor, R. N. Manchester, A. J. Lyne, and F. Camilo, private communication (1995).
3. A. F. Illarionov and R. A. Sunyaev, Astron. Astrophys. **39**, 185 (1975).
4. I. F. Malov, Astron. Zh. **74**, 697 (1997) [Astron. Rep. **45**, 389 (2001)].
5. N. D'Amico, A. Possenti, R. N. Manchester, *et al.*, Astrophys. J. **561**, L89 (2001).
6. S. L. Shapiro and S. A. Teukolsky, *Black Holes, White Dwarfs, and Neutron Stars: the Physics of Compact Objects* (Wiley, New York, 1983; Mir, Moscow, 1985), Vol. 2.
7. I. S. Gradshtein and I. M. Ryzhik, *Tables of Integrals, Sums, Series, and Products* (Nauka, Moscow, 1971), p. 78 [in Russian].
8. A. M. Cherepashchuk, *Physics of Neutron Stars* (St. Peterburg, 2001), p. 16 [in Russian].
9. F. Camilo, *IAU Coll. 160: Pulsars: Problems and Progress,* Ed. by S. Johnston, M. A. Walker, and M. Bailes, ASP Conf. Ser. **105**, 39 (1996).
10. D. C. Morton, Astrophys. J. **150**, 535 (1967).
11. L. V. Kuhi, Astrophys. J. **143**, 991 (1966).
12. A. Deich, in *Cosmic Gas Dynamics* (*Atti del IV symposium sulla dinamica del Gas Cosmico, Varenna sul Lago di Como, 1960*) [in Italian].

Translated by G. Rudnitskiĭ

Astronomy Reports, Vol. 48, No. 4, 2004, pp. 342–351. Translated from Astronomicheskiĭ Zhurnal, Vol. 81, No. 4, 2004, pp. 375–384.
Original Russian Text Copyright © 2004 by Ostryakov, Stovpyuk, Shevel'ko.

Acceleration of Multiply Charged Ions of the Anomalous Cosmic-Ray Component at the Heliosphere Boundary

V. M. Ostryakov[1], **M. F. Stovpyuk**[1], **and V. P. Shevel'ko**[2]

[1]*St. Petersburg State Polytechnical University, St. Petersburg, Russia*
[2]*Lebedev Physical Institute, Russian Academy of Sciences, Leninskiĭ pr. 53, Moscow, 117924 Russia*

Received March 21, 2003; in final form, November 10, 2003

Abstract—The formation of the energy spectra of heavy ions at the front of a parallel shock is considered taking into account ionization and recombination during the acceleration. An analytic solution for ions with three possible charge states is obtained and applied to the acceleration of the anomalous cosmic-ray component at the boundary of the heliosphere. In addition, a more general numerical model for such acceleration at a spherical shock front is developed and used to obtain the energy dependence of the mean charges for C, N, O, Ne, Si, S, Ar, and Fe ions. The model implies that highly excited ions begin to dominate over ions with low charges at energies above 1 MeV/nucleon, in agreement with observational data. © *2004 MAIK "Nauka/Interperiodica"*.

1. INTRODUCTION

The anomalous component of the cosmic rays (CRs) accelerated at the boundary of the heliosphere was considered until recently to be made up of particles with low charges (with a mean charge of $q = +1$, or sometimes $q = +2$). A number of theoretical arguments and experimental data supported this point of view [1, 2]. However, anomalous-component fluxes with ionization states $q > 2$ have recently been measured, and, in fact, particles with large q were found to be the most numerous at certain energies. Such data were initially obtained for oxygen ions [3] and later for carbon, nitrogen, and neon [4, 5], although the errors of the measurements in [4, 5] were large.

It is currently believed that the main source of the anomalous CR component is neutral interstellar gas flowing into the heliosphere [1, 6]. Elements with high ionization potentials (for example, $I_{\rm N} = 14.5$ eV and $I_{\rm O} = 13.6$ eV) are neutral in the local interstellar medium and, in contrast to charged particles, can enter the heliosphere freely. These neutrals experience a single ionization at small heliospheric distances (<5 AU) via solar ultraviolet radiation or charge-exchange reactions with solar-wind protons. The ions formed are picked up by the solar wind and carried to the heliospheric boundary (∼100 AU), where they are accelerated by shock waves. Elements with low ionization potentials can also be present in the anomalous CR component, but this happens via other mechanisms. For example, carbon atoms ($I_{\rm C} = 11.3$ eV) can be knocked out during collisions of solar-wind particles with interplanetary dust [7, 8]. This source of pick-up ions probably makes a smaller contribution to the anomalous component than does neutral gas: according to observations by the WIND spacecraft, N/C > 12 and O/C > 100 at energies of ∼5 MeV/nucleon [9]. In data on the charge composition of the anomalous CR component measured by SAMPEX [3–6, 9], the fluxes of O^{2+} and O^{3+} considerably exceed the fluxes of O^{+} at energies above 10 MeV/nucleon. Therefore, it is likely that the acceleration (and subsequent propagation inside the heliosphere) is accompanied by ion stripping.

Theoretical models simultaneously taking into account the acceleration of particles and changes in their charges (charge-consistent models) were first presented in [10, 11] for regular and stochastic mechanisms, respectively. Although these works were analytical and based on a number of simplifications, they provided a qualitatively correct description of the observed phenomena, in particular, the increase of the mean ion charge with energy. This effect will be demonstrated in Section 2 of the present paper for the particular case of ions with three charge states. We obtained a solution to this problem in analytic form applying the same approach used for doubly charged ions in [10]. The subsequent application of more realistic charge-consistent numerical models to explain the available experimental data on the mean charges of heavy ions (C, O, Ne, Mg, Si, and Fe) in the solar cosmic rays [12] has become an important tool for diagnostics of the solar plasma. This is possible because the main parameters of the numerical modeling are the density and temperature of the background plasma.

A charge-consistent numerical model for the generation of the anomalous component in which the particles are accelerated at a spherical shock front due to regular acceleration will be presented in Section 3. Such calculations were carried out earlier for ions of oxygen [13], carbon [14], and a number of heavy elements [15]. However, in those studies, only stripping by atomic hydrogen (in [13, 15]) and helium (in [15]) were taken into account, while collisional ionization by free protons and electrons and recombination were neglected. A finite-differences method was used in [13, 15]. The model we develop in the present work is based on Monte Carlo computations, which enables us to easily take into account adiabatic losses and the finite thickness of the shock front, for example, as well as to consider the spherically symmetric rather than the planar case. Another difference from earlier studies is our use of the latest data for the cross sections of atomic reactions [16, 17].

Thus, we derive here the energy dependence of the mean charges of C, N, O, Ne, Si, S, Ar, and Fe ions in the anomalous CR component taking into account stripping reactions, as well as reactions involving the capture of electrons from interstellar neutral hydrogen and helium by C and O ions.

2. ANALYTIC CONSIDERATION

Let us consider the regular acceleration of ions (for example, oxygen) at the boundary of the heliosphere. Measurements show that ions with charges $q > 3$ are almost absent up to energies of about 10 MeV/nucleon [3–6]. Therefore, we will take into consideration only the charge states +1, +2, and +3 and assume that O$^+$ ions are formed from neutral atoms of interstellar gas. The set of steady-state equations describing the diffusion of particles near a plane-parallel shock is very similar to the system presented in [10]:

$$\frac{\partial}{\partial x}\chi_{1i}^{||}\frac{\partial}{\partial x}n_{1i} - u_i\frac{\partial n_{1i}}{\partial x} - \frac{n_{1i}}{\tau_{10}} - \frac{n_{1i}}{\tau_{12}} + \frac{n_{2i}}{\tau_{21}} = 0, \tag{1}$$

$$\frac{\partial}{\partial x}\chi_{2i}^{||}\frac{\partial}{\partial x}n_{2i} - u_i\frac{\partial n_{2i}}{\partial x} - \frac{n_{2i}}{\tau_{21}} - \frac{n_{2i}}{\tau_{23}} + \frac{n_{1i}}{\tau_{12}} + \frac{n_{3i}}{\tau_{32}} = 0,$$

$$\frac{\partial}{\partial x}\chi_{3i}^{||}\frac{\partial}{\partial x}n_{3i} - u_i\frac{\partial n_{3i}}{\partial x} - \frac{n_{3i}}{\tau_{32}} - \frac{n_{3i}}{\tau_{34}} + \frac{n_{2i}}{\tau_{23}} = 0,$$

where the subscript $i = 1, 2$ corresponds to the regions in front of and behind the shock front ($x < 0$ and $x > 0$). For brevity, the dependence on the coordinate x and momentum p is not written in the required distribution functions n_{qi}, and the subscript $q = +1, +2, +3$ describes the ion charge. According to [18, 19], the spatial diffusion coefficient for ions along the regular magnetic field in the case of Alfvenic turbulence is

$$\chi_{qi}^{||} = \chi_{0i}^{||}(q/A)^{a-2}E^{(3-a)/2}, \tag{2}$$

where α is the spectral index of the turbulence; A, the mass number of the particle; and $\chi_{0i}^{||}$, a constant coefficient. It is assumed in (1) that u_i is the hydrodynamic plasma velocity in front of and behind the shock:

$$u_i = \begin{cases} u_1 = u_0, \quad x < 0, \\ u_2 = \dfrac{2 + M_1^2(\kappa - 1)}{M_1^2(\kappa + 1)}u_0 = \dfrac{u_0}{\sigma}, \quad x > 0, \end{cases} \tag{3}$$

where κ is the adiabatic index; $M_1 = u_1/V_s$, the Mach number (V_s is the speed of sound); and σ, the degree of compression of the shock. We can see in (1) that changes of the ion charges are taken into account via the characteristic transition times $\tau_{q(q\pm1)}$ from one charge state to another due to ionization (for the subscript $q(q+1)$) or recombination (for the most part, by electron capture, for the subscript $q(q-1)$). We will assume in this section that all quantities $\tau_{q(q\pm1)}$ are averaged over the energy E and, consequently, do not depend on the energy. The diffusion coefficients $\chi_{qi}^{||}$ are also assumed to be independent of E and the subscript i; i.e. $\chi_{qi}^{||} \equiv \chi_q$ (for brevity, the superscript || will be omitted further in this section). These restrictions will be removed in the numerical model considered in the next section.

It is clear from the structure of Eqs. (1) that we should seek a solution in exponential form ($\sim e^{\lambda x}$). As a result, we obtain a system of three quadratic equations for λ. Equating the determinant of this system to zero and knowing χ_q and $\tau_{q(q\pm1)}$, we can obtain numerically the quantities $\lambda_{1,2,3} > 0$ (for $x < 0$) and $\lambda_{4,5,6} \le 0$ (for $x > 0$) for which the solutions are finite in the corresponding regions. Therefore, the total solution of (1) can be written as

$$\begin{cases} n_{11} = C_1e^{\lambda_1 x} + C_2e^{\lambda_2 x} + C_3e^{\lambda_3 x} \\ n_{21} = AC_1e^{\lambda_1 x} + BC_2e^{\lambda_2 x} + DC_3e^{\lambda_3 x} \\ n_{31} = FC_1e^{\lambda_1 x} + GC_2e^{\lambda_2 x} + HC_3e^{\lambda_3 x} \end{cases} \tag{4}$$
$$\text{at} \quad x < 0,$$

$$\begin{cases} n_{12} = C_1^*e^{\lambda_4 x} + C_2^*e^{\lambda_5 x} + C_3^*e^{\lambda_6 x} \\ n_{22} = A^*C_1^*e^{\lambda_4 x} + B^*C_2^*e^{\lambda_5 x} + D^*C_3^*e^{\lambda_6 x} \\ n_{32} = F^*C_1^*e^{\lambda_4 x} + G^*C_2^*e^{\lambda_5 x} + H^*C_3^*e^{\lambda_6 x} \end{cases}$$
$$\text{at} \quad x > 0.$$

The coefficients A, B, D, F, G, H, A^*, B^*, D^*, F^*, G^*, and H^* can be found by substituting (4) into (1) and equating coefficients of corresponding exponents to zero. As a result, we obtain

$$A \equiv A(\lambda_1) = \tau_{21}\left(\frac{1}{\tau_{12}} + \frac{1}{\tau_{10}} + u_1\lambda_1 - D\lambda_1^2\right), \tag{5}$$

$$B = A(\lambda_2), \quad D = A(\lambda_3),$$

$$F(\lambda_1) = \frac{A(\lambda_1)/\tau_{23}}{\tau_{32}^{-1} + \tau_{34}^{-1} + u_1\lambda_1 - \lambda_1^2 D_1},$$

$$G = F(\lambda_2), \quad H = F(\lambda_3), \quad A^* = A(\lambda_4),$$

$$B^* = A(\lambda_5), \quad D^* = A(\lambda_6), \quad F^* = F(\lambda_4),$$

$$G^* = F(\lambda_5), \quad H^* = F(\lambda_6).$$

Here and below, quantities with asterisks refer to the region behind the shock front ($x > 0$) and therefore contain the corresponding velocity from (3). Now, let us take into consideration the fact that the densities of the various charge components n_{qi} must be continuous at the front (see, for example, [20]). Consequently, using (4), we can write

$$C_1^* = \varphi C_1 + \xi C_2 + \psi C_3, \quad C_2^* = \eta C_1 + \mu C_2 + \nu C_3,$$

$$C_3^* = \alpha C_1 + \beta C_2 + \gamma C_3.$$

All the coefficients denoted by Greek letters can be found easily using the method of Gauss:

$$\alpha \equiv \alpha(F, A) \tag{6}$$

$$= \frac{(F - F^*)(B^* - A^*) - (A - A^*)(G^* - F^*)}{(B^* - A^*)(H^* - F^*) - (D^* - A^*)(G^* - F^*)},$$

$$\beta = \alpha(G, B), \quad \gamma = \alpha(H, D),$$

$$\varphi(A, \alpha) = \frac{B^* - A - \alpha(B^* - D^*)}{B^* - A^*}, \quad \xi = \varphi(B, \beta),$$

$$\psi = \varphi(D, \gamma), \quad \eta(A, \alpha) = \frac{A - A^* - \alpha(D^* - A^*)}{B^* - A^*},$$

$$\mu = \eta(B, \beta), \quad \nu = \eta(D, \gamma).$$

To obtain the energy spectrum at the front, let us use the condition imposed on the fluxes of the accelerated particles [20]:

$$\chi_q\left(\left.\frac{\partial n_{q1}}{\partial x}\right|_{x\to-0} - \left.\frac{\partial n_{q2}}{\partial x}\right|_{x\to+0}\right) - \Delta u n_{q1}\Big|_{x=0} \tag{7}$$

$$= -\frac{\Delta u}{3}\frac{\partial(n_{q1}p)}{\partial p}, \quad q = 1, 2, 3,$$

where p is the momentum of the particles and $\Delta u = u_1 - u_2$ is the velocity jump at the shock front. Substituting (4) into (7), we obtain a system of homogeneous differential equations for the variable p:

$$\Lambda_1' C_1 + \Lambda_2' C_2 + \Lambda_3' C_3 \tag{8}$$

$$= -\frac{\Delta u}{3\chi_1} p \frac{\partial(C_1 + C_2 + C_3)}{\partial p},$$

$$\Lambda_4' C_1 + \Lambda_5' C_2 + \Lambda_6' C_3$$

$$= -\frac{\Delta u}{3\chi_2} p \frac{\partial(AC_1 + BC_2 + DC_3)}{\partial p},$$

$$\Lambda_7' C_1 + \Lambda_8' C_2 + \Lambda_9' C_3$$

$$= -\frac{\Delta u}{3\chi_3} p \frac{\partial(FC_1 + GC_2 + HC_3)}{\partial p},$$

where $\Lambda_m' = \Lambda_m - \frac{2}{3}\frac{\Delta u}{\chi_1}$ for $m = 1$–3, $\Lambda_m' = \Lambda_m - \frac{2}{3}\frac{\Delta u}{\chi_2}\begin{pmatrix} A \\ B \\ D \end{pmatrix}$ for $m = 4$–6, and $\Lambda_m' = \Lambda_m - \frac{2}{3}\frac{\Delta u}{\chi_3}\begin{pmatrix} F \\ G \\ H \end{pmatrix}$ for $m = 7$–9. The functions Λ_m are expressed via the coefficients α, β, ... and A, B, ... as follows:

$$\begin{pmatrix} \Lambda_1 \\ \Lambda_2 \\ \Lambda_3 \\ \Lambda_4 \\ \Lambda_5 \\ \Lambda_6 \\ \Lambda_7 \\ \Lambda_8 \\ \Lambda_9 \end{pmatrix} = \begin{pmatrix} \lambda_1 \\ \lambda_2 \\ \lambda_3 \\ A\lambda_1 \\ B\lambda_2 \\ D\lambda_3 \\ F\lambda_1 \\ G\lambda_2 \\ H\lambda_3 \end{pmatrix} - \lambda_4 \begin{pmatrix} \varphi \\ \chi \\ \psi \\ A^*\varphi \\ A^*\xi \\ A^*\psi \\ F^*\varphi \\ F^*\xi \\ F^*\psi \end{pmatrix}$$

$$- \lambda_5 \begin{pmatrix} \eta \\ \mu \\ \nu \\ B^*\eta \\ B^*\mu \\ B^*\nu \\ G^*\eta \\ G^*\mu \\ G^*\nu \end{pmatrix} - \lambda_6 \begin{pmatrix} \alpha \\ \beta \\ \gamma \\ D^*\alpha \\ D^*\beta \\ D^*\gamma \\ H^*\alpha \\ H^*\beta \\ H^*\gamma \end{pmatrix}.$$

Equations (8) can be solved using a Mellin transformation with respect to the dimensionless momentum p/p_o (where p_o is the injection momentum for various ions, assumed to be independent of the ion species):

$$\bar{Y}(s) = \int\limits_0^\infty y(t)t^{s-1}dt,$$

$$y(t) = \frac{1}{2\pi i} \int\limits_{\sigma_0 - i\infty}^{\sigma_0 + i\infty} \bar{Y}(s) t^{-s} ds.$$

Let N_{qo} be the injection density of the ions for $p = p_o$. System (8) can then be rewritten in the form

$$\begin{gathered} \bar{C}_1(\Lambda_1' - U_1 s) + \bar{C}_2(\Lambda_2' - U_1 s) \\ + \bar{C}_3(\Lambda_3' - U_1 s) = -U_1 N_{10}, \\ \bar{C}_1(\Lambda_4' - AU_2 s) + \bar{C}_2(\Lambda_5' - BU_2 s) \\ + \bar{C}_3(\Lambda_6' - DU_2 s) = -U_2 N_{20}, \\ \bar{C}_1(\Lambda_7' - FU_3 s) + \bar{C}_2(\Lambda_8' - GU_3 s) \\ + \bar{C}_3(\Lambda_9' - HU_3 s) = -U_3 N_{30}, \end{gathered} \tag{9}$$

where the transformed quantities are marked by bars, $U_q = \Delta u / (3\chi_q)$, and s is the parameter of the Mellin transformation. The solution of (9) will be

$$\bar{C}_k(s) = \frac{f_k(s)}{\Omega(s - s_1)(s - s_2)(s - s_3)}, \quad k = 1, 2, 3, \tag{10}$$

where $\Omega = U_1 U_2 U_3 (AH + DG + BF - BH - DF - AG)$ and the functions $f_k(s)$ can be easily determined from (9). Here, s_1, s_2, and s_3 are the real roots of the cubic equation obtained by setting the determinant of (9) equal to zero.

The form of solution (10) is very important for understanding the resulting energy spectrum of the ions. Since the singular points in (10) are simple poles, their contribution to $C_k(p)$ is additive. As a result, the solution is a sum of power-law functions with indices s_1, s_2, and s_3:

$$C_k(p) = \frac{1}{\Omega} \sum_{i=1}^{3} \frac{f_k(s_i) p^{-s_i}}{\Pi'(s_i - s_j)}, \quad k = 1, 2, 3. \tag{11}$$

Here, Π' is the product of the multipliers (over the subscripts $i = 1$–3) with the term $i = j$ omitted. If the indices s_1, s_2, and s_3 are close to each other, the spectrum of the individual ionization state is also formed by these neighboring states; i.e., processes that change the charge are important. In the opposite case (for example, at $s_1 \gg s_2 \gg s_3$), the spectra will be similar to those obtained in a test-particle approximation, since charge transitions between the neighboring states will be negligible.

Let us briefly discuss the effect of charge variations on the formation of the spectra of the anomalous CR component. The characteristic times for the charge transitions $\tau_{q(q\pm1)}$ for the oxygen ions were estimated using the cross sections presented in [16, 17, 21–25]. (We do not discuss the data on the cross sections in detail here; this will be done in the next section.) These times were averaged over several energy intervals, so that the $\tau_{qq\pm1}$ are approximately constant within each of them. This enabled us to calculate the spectra in each interval using the formulas of the present section and then match the fluxes at the boundaries of these intervals. The plot in Fig. 1 shows that the dominance of highly charged ions is evident at energies above 10 MeV/nucleon. Although the capture cross section at energies of 10–100 keV/nucleon is an order of magnitude greater than the ionization cross section, taking electron capture into consideration does not appreciably affect the shape of the spectrum. The differences at these energies are only ~20%, and the high-energy part of the spectrum is not affected at all. We emphasize once again that the distributions obtained refer to the region near the shock front.

3. NUMERICAL MODELING

Let us consider the regular acceleration of multiply charged ions at the front of a stationary spherically symmetric shock (where the coordinate r is measured from the center of the Sun). We take into account here all possible charge states (unlike the previous section, where only the first three states were considered). The corresponding set of equations for the spatial diffusion of the ions with distribution function $n_{qi}(r, E) \equiv n_{qi}$ is

$$\begin{gathered} \frac{1}{r^2} \frac{\partial}{\partial r} \left(r^2 \chi_{qi} \frac{\partial n_{qi}}{\partial r} \right) - w_i(r) \frac{\partial n_{qi}}{\partial r} \\ + \frac{1}{r^2} \frac{\partial}{\partial r} (r^2 w_i(r)) \left(\frac{2E}{3} \frac{\partial n_{qi}}{\partial E} - \frac{n_{qi}}{3} \right) \\ + (n_{(q-1)i} S_{(q-1)i} - n_{qi}(S_{qi} + \alpha_{qi}) \\ + n_{(q+1)i} \alpha_{(q+1)i}) = \frac{\partial n_{qi}}{\partial t}, \end{gathered} \tag{12}$$

where $q = 0, +1, \ldots + Z$ and Z is the charge of the nucleus. The diffusion coefficients were taken in accordance with [14]:

$$\chi_{qi} = \chi_{qi}^{||} \cos^2 \theta + \chi_{qi}^{\perp} \sin^2 \theta, \tag{13}$$

where θ is the angle between the magnetic field and a unit vector perpendicular to the shock front and the $\chi_{qi}^{||}$ are given by (2). Both the energy dependence of the diffusion coefficients and their difference in the regions $i = 1$ and $i = 2$ was taken into account in the numerical modeling. The inequality $\chi_{qi}^{||} \gg \chi_{qi}^{\perp}$ is usually satisfied and was used in our calculations. The solar-wind velocity $w_i(r)$ in front of and behind the shock will be

$$w_i(r) = \begin{cases} W, & i = 1, \quad r \le R - \delta/2, \\ W/\sigma, & i = 2, \quad r \ge R + \delta/2, \end{cases} \tag{14}$$

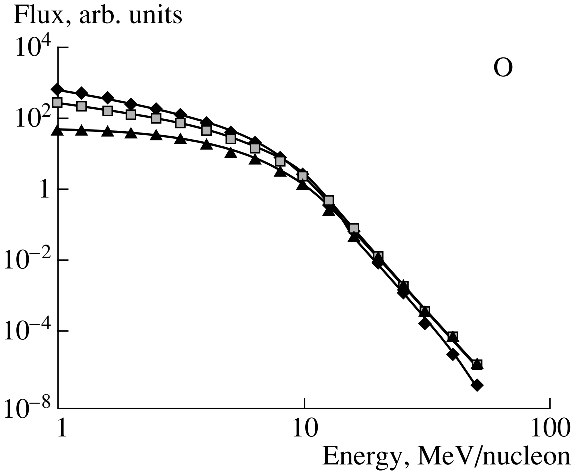

Fig. 1. Steady-state energy spectra of O^+ (diamonds), O^{+2} (squares), and O^{+3} (triangles) ions accelerated at the heliospheric boundary. The modeling parameters were $\chi_1 = \chi_2 = \chi_3 = 3 \times 10^{19}$ cm^2/s, $a = 1.7$, $\sigma = 3$, $N_e = N_p = N_{\rm H} = 0.1$ cm^{-3}, and $N_{\rm He} = 0.01$ cm^{-3}.

where W is the hydrodynamic plasma velocity in the inner heliosphere (in front of the shock), which is assumed at such distances to be constant and equal to 400 km/s; R is the radius of the shock; and δ is the width of the front. We assume also that the variation of the hydrodynamic velocity over the distance δ is described by the law

$$w(r) = \frac{W(\sigma+1)}{2\sigma} - \frac{W(\sigma-1)}{2\sigma}\,\mathrm{th}\left(\frac{r-R}{\delta}\right), \quad (15)$$

which differs from (3) (see [20] and references therein).

The ionization rates

$$S_{qi} = \sum_k N_{ki} V_{\rm ion} \sigma_{q(q+1)}(E) \quad (16)$$

and recombination rates

$$\alpha_{qi} = \sum_k N_{ki} V_{\rm ion} \sigma_{q(q-1)}(E) \quad (17)$$

were used in (12) instead of the characteristic transition times introduced in (1). Here, $\sigma_{q(q+1)}(E)$ and $\sigma_{q(q-1)}(E)$ are the corresponding cross sections, which depend on the energy E of the accelerated ion, and $V_{\rm ion} = \sqrt{2E/Am_p}$. The summation in (16) and (17) is carried out over all components with densities N_{ki} whose reactions contribute substantially to the variations of the anomalous-component ion charges. Note also that the injection of particles of each kind occurs in our model at time $t = 0$ at energy E_o at the shock front ($r = R$). Any energy at which the anomalous-component ions are still singly charged (for example, $E_o = 50$ keV/nucleon) can be chosen as the initial energy. We do not consider here the more general problem of particle acceleration directly from thermal energies, as was done in [32], since in that case we must inevitably deal with the problem of the particle injection (see, for example, [20]).

Let us briefly outline the approaches to solving system (12). Mathematically, this is very similar to the problem of the acceleration of solar cosmic-ray ions by a shock moving in the solar corona [26]. As in [26], we can write for each time step Δt a change in the particle coordinate

$$r_k = r_{k-1} \quad (18)$$
$$+ \left(w_i(r_{k-1}) - \frac{\chi_{qi}(r_{k-1})}{r_{k-1}} - \left.\frac{\partial \chi_{qi}(r)}{\partial r}\right|_{r=r_{k-1}} \right)\Delta t + \eta$$

(where η is a random Gaussian variable). The change in the particle energy obtained from (12) is then

$$E_k = E_{k-1}\left(1 - \frac{2}{3}\nu_{ik}\Delta t\right), \quad (19)$$

where

$$\nu_{ik} \equiv \left(\frac{1}{r^2}\frac{\partial(r^2 w_i(r))}{\partial r}\right)_{r=r_{k-1}}. \quad (20)$$

The sign of the coefficient ν_{ik} depends on which region relative to the front is considered. For example, in regions far from the front, $r_k \gg R + \delta/2$ and $r_k \ll R - \delta/2$ [see dependence (14)], the coefficient ν_{ik} describes the adiabatic energy-loss rate of the particles due to their propagation in the expanding solar wind: $\nu_{1k} = 2W/r_k$ and $\nu_{2k} = 2W/(\sigma r_k)$. In and near the region of the shock transition at $r_k \in [R - \delta/2, R + \delta/2]$ [see (15)], the coefficient ν_{ik} also includes the rate of the regular increase in energy due to sequential collisions of the particles with plasma irregularities: $\nu_{ik} = \dfrac{2w_i(r_k)}{r_k} - \dfrac{W(\sigma-1)}{2\sigma\delta}\cosh^{-2}\left(\dfrac{r_k - R}{\delta}\right)$. The coefficients ν_{1k} and ν_{2k} become negative near the front, while the corresponding increase in energy (19) becomes positive and equal to $\Delta E_k = -2\nu_{ik}E_{k-1}/3$.

Let us now discuss the method used to count the particles in our procedure. In the theory of regular acceleration at a shock front, the characteristic acceleration time for particles with energy E is given by [27]

$$T_a^q(E) = \frac{3}{2(u_1 - u_2)}\left(\frac{\chi_{q1}^{||}}{u_1} + \frac{\chi_{q2}^{||}}{u_2}\right). \quad (21)$$

If we take $u_1 = w_1 = 400$ km/s, $\sigma = 2.6$, and $\chi_{0i}^{||} = 10^{19}$ cm^2/s, this time will be $T_a^q(E) \leq 1$ yr for $E = 20$ MeV/nucleon. Let us assume that the time during which the particles are trapped, when their charges can be changed (including the propagation time inside the heliosphere), is of the same order of magnitude, $T_{\mathrm{cap}} \sim 1$ yr. Precisely this quantity was adopted as the typical time for counting the particles.

3.1. Changes in the Charges of the Anomalous-Component Ions during Interactions with the Local Interstellar Medium

The probabilities of the ionization and recombination of a heavy ion during each time step Δt were computed in the same way as in [26]. Let us consider the atomic processes that must be taken into account. The following are the main candidate processes:

(1) ionization via collisions with protons and electrons of the local interstellar medium, whose density near the shock is $N_p \approx N_e \approx 0.1$–$0.3$ cm^{-3} [28];

(2) dielectron and radiative recombination;

(3) ionization via collisions with neutral interstellar hydrogen and helium, whose densities are $N_{\mathrm{H}} \approx 0.15$–$0.34$ cm^{-3} [28] and $N_{\mathrm{He}} \approx 0.005$–$0.01$ cm^{-3} [29];

(4) charge-exchange reactions with neutral hydrogen and helium.

The cross sections of the first two processes for the elements considered here were calculated using the same method that was used in [12, 30, 31] for a variety of ions. The parameters required for the calculations were taken from [21–23]. The averaging over the Maxwellian distribution of the background particles was carried out for plasma parameters characteristic of solar flares. However, at distances of ∼100 AU from the Sun (where the shock accelerating the particles is located), the temperature of the surrounding medium and the corresponding thermal velocities are considerably lower than in solar flares. For example, according to [32], $T_p = 535$ K at a distance of ∼85 AU. Therefore, it is not necessary to average the reaction rates over the Maxwellian distribution for the background particles [31], and we can simply use approximation (16), (17). The calculations show that the mean rates of stripping in collisions between heavy ions and the protons in the plasma are about twice the rate of collisions with electrons. The radiative and dielectron recombination rates are substantially lower than the rates of capture due to charge exchange. Therefore, the second type of process will not be taken into account here.

Next, let us consider the third type of process. As was mentioned in our earlier work [14], the cross sections for the ionization of O by neutral hydrogen used by Jokipii [13] were overestimated by one to two orders of magnitude. This fact was revealed by comparing the old data with a number of mutually consistent independent results [16, 17, 24, 33]. Here, we use the latest calculations available [16, 17], in which the cross sections for stripping by neutral hydrogen were obtained for nearly all the elements represented in the anomalous CR component. These results were computed using the LOSS software based on a modification of the first Born approximation in a partial-wave representation. The wave functions of the optical electron (the electron undergoing a transition) were found via a numerical solution of the radial Schrödinger equation in the effective field of the atomic core (for more details, see [17]).

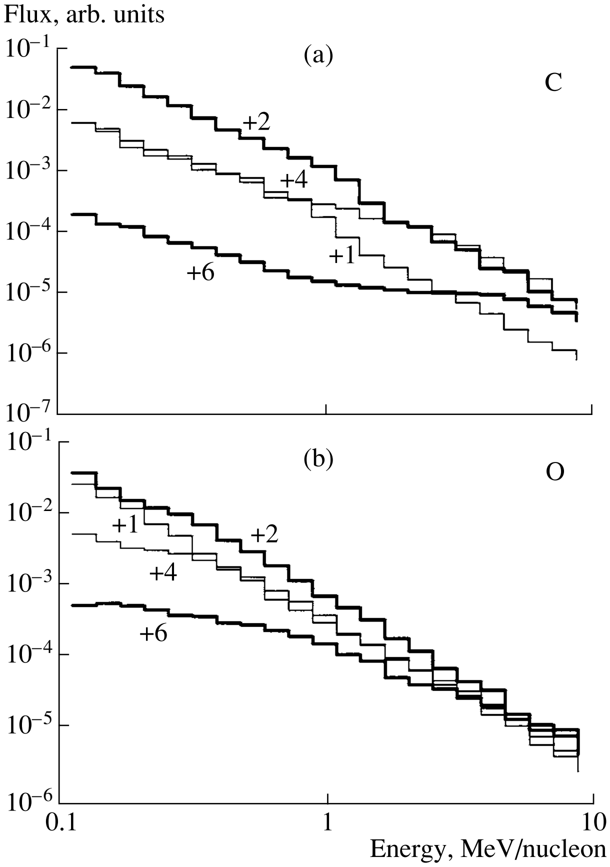

Fig. 2. Energy spectra of (a) carbon and (b) oxygen in the anomalous CR component calculated for $\chi_{0i}^{||}\cos^2\theta = 10^{19}$ cm^2/s, $u_1 = 4 \times 10^7$ cm/s, $a = 1.5$, $\sigma = 2.6$, $\delta = 10^5$ km, $T_{cap} = 1$ yr, $N_e = N_p = 0.1$ cm^{-3}, $N_{\mathrm{H}} = 0.15$ cm^{-3}, and $N_{\mathrm{He}} = 0.01$ cm^{-3}. The ion charges q are shown near the curves.

Finally, let us turn to the capture of electrons from atoms of hydrogen and helium. Interpolation formulas for C and O ions obtained at the Oak Ridge National Laboratory were used for the cross sections of such processes [25]. These calculations indicate that the cross sections for electron capture from H and He by C and O are comparable. However, data from the

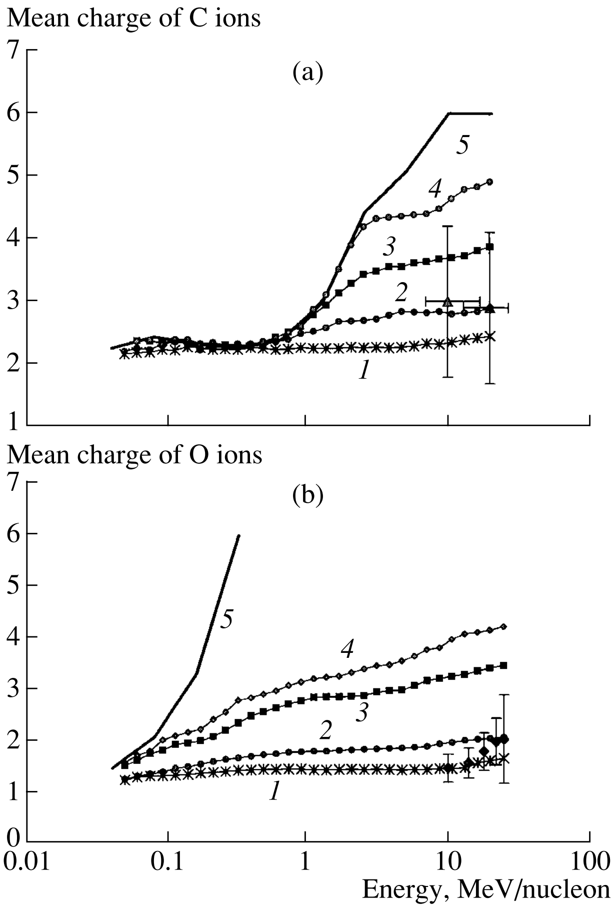

Fig. 3. Mean charges of the accelerated ions of (a) carbon and (b) oxygen calculated for $u_1 = 4 \times 10^7$ cm/s, $a = 1.5$, $\sigma = 2.6$, $\delta = 10^5$ km, $N_e = N_p = 0.1$ cm^{-3}, $N_{\rm H} = 0.15$ cm^{-3}, $N_{\rm He} = 0.01$ cm^{-3}; $\chi_{0i}^{||} \cos^2\theta = 3 \times 10^{19}$ cm^2/s (curve *1*), 10^{19} cm^2/s (curves *2* and *3*), and 5×10^{18} cm^2/s (curve *4*); $T_{\rm cap} = 0.5$ yr (curves *1* and *2*) and 1 yr (curves *3* and *4*). The bold solid curves *5* correspond to the case of equilibrium charge; the filled triangles and diamonds represent the data from the SAMPEX satellite [4, 5].

ULYSSES spacecraft show that the density of He is approximately an order of magnitude lower than the density of H [29], so that the contribution from charge-exchange reactions with He is small ($\leq 10\%$). In general, the contribution of such processes for C and O was small in the energy range under consideration (0.05–25 MeV/nucleon), and we did not include electron capture when calculating the mean charges of other elements.

The characteristic time scale for photoionization at distances of ~ 100 AU estimated from the data of [34] turned out to be very large (> 60 yr) compared to the time scales for acceleration and the other processes involved. However, photoionization is important for the formation of singly charged ions at heliocentric distances of ~ 3–5 AU, i.e., for the formation of the injection distributions of the anomalous CR component.

Let us summarize the processes to be considered. These are (i) collisional ionization by interstellar atomic hydrogen and helium, (ii) collisional ionization by free electrons and protons (except for Ar, see below), and (iii) electron capture from atomic hydrogen and helium (only for C and O).

3.2. Results of Numerical Computations

This subsection is devoted to the basic results of the computations. Since the characteristic time scales for the ionization and recombination of all the ions—C, N, O, Ne, Si, S, Ar, and Fe—are known, we can calculate the charge and energy distributions for these elements formed during their acceleration by a shock near the boundary of the heliosphere due to the action of the atomic processes listed above. The only exception is Ar, for which only collisional ionization by H and He was taken into account, while interactions with free electrons and protons were neglected. Therefore, the results for this element were obtained for the case when the density of free electrons and protons was considerably lower than the density of neutral gas.

The energy spectra of the accelerated C and O ions computed taking into account the above atomic processes for a degree of compression of the shock of $\sigma = 2.6$ [35] are shown in Fig. 2. All the plots show a tendency for a gradual increase in the fraction of highly charged ions with increasing energy. Figure 3 presents dependences of the mean charges of C and O for various values of the product of the particle-acceleration time and the density of reagents in the background plasma $T_a^q N$ for time scales for trapping of the particles near the shock of $T_{\rm cap} \approx 1$ yr (curves *3* and *4*) and $T_{\rm cap} \approx 0.5$ yr (curves *1* and *2*). We also calculated equilibrium curves for the mean charges of both elements (curves *5*; see, for example, [12]). These curves correspond to the case when the energetic ions reside in the plasma long enough that their mean charges at a fixed energy do not depend on the density of the surrounding plasma. The following two tendencies can be clearly traced in Fig. 3:

(1) the longer the particles reside in the acceleration region or are trapped there after acceleration, the greater their mean charge at a given energy, i.e., the closer the mean-charge curve of the accelerated ions is to its equilibrium curve (cf. curves *2* and *3*);

(2) for equal times of residence in the region of changing charge (i.e., for equal values of $T_{\rm cap}$, cf. curves *1* and *2* or *3* and *4*), the mean charge of the ions increases with their acceleration rate.

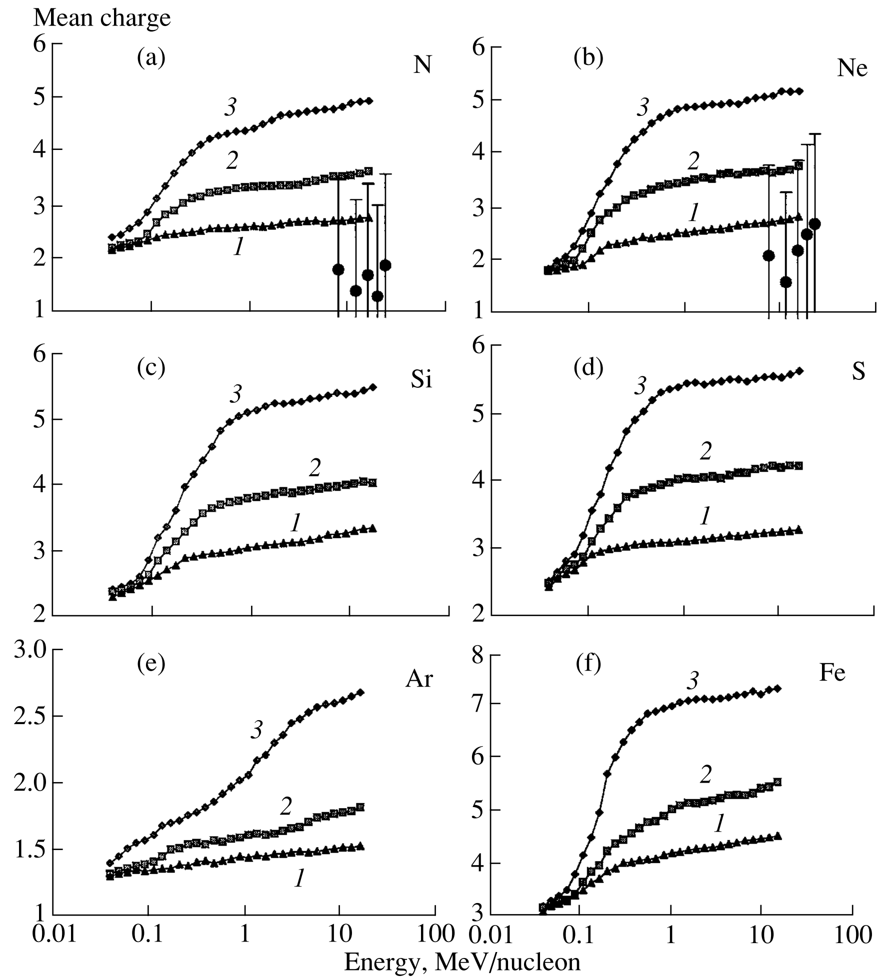

Fig. 4. Mean charges of the accelerated ions of (a) N, (b) Ne, (c) Si, (d) S, (e) Ar, and (f) Fe calculated for $u_1 = 4 \times 10^7$ cm/s, $a = 1.5$, $\sigma = 2.6$, $\delta = 10^5$ km, $N_e = N_p = 0.1$ cm^{-3}, $N_{\rm H} = 0.15$ cm^{-3}, $N_{\rm He} = 0.01$ cm^{-3}; $\chi^{||}_{0i} \cos^2\theta = 3 \times 10^{19}$ cm^2/s (curve *1*) and 10^{19} cm^2/s (curves *2* and *3*); $T_{\rm cap} = 0.5$ yr (curves *1* and *2*) and 1 yr (curve *3*).

The mean charges we have obtained are approximately one unit higher than the charges we obtained in [14] for the same parameters. This is because we considered in [14] a stationary problem, and the numerical scheme in the finite-difference method was constructed so that the time for acceleration to any energy automatically coincided with the time for the escape of the particles with that energy from the acceleration region. We have considered here the more realistic case when particles can change their charges even after leaving the shock front. This explains, in particular, why the mean-charge curves for the accelerated particles nearly coincide with the equilibrium curves in both of the plots in Fig. 3 for low energies. Finally, the mean charges computed for other elements represented in the anomalous CR component—N, Ne, Si, S, Ar, and Fe—are presented in Figs. 4a–4f. All these plots exhibit the same characteristic features as the plots in Fig. 3.

Let us consider now the main differences of our new results from those presented recently by Cummings *et al.* [15].

(1) Collisional ionization by free electrons and protons of the local interstellar medium was not taken into account in [15]. On the other hand, as we showed in [14], the contribution of such processes to the formation of the mean charges is comparable to the contribution from stripping by neutral hydrogen. Indirect evidence for this fact can also be obtained from Fig. 4, which shows that the mean charge of Ar (computed taking into account only ionization by neutrals) is a factor of two to three lower than the mean charges of even the lighter elements.

(2) Cummings *et al.* [15] claim that collisional ionization by helium increases the total ionization rate by 85% compared to the case when only hydrogen is taken into account. However, as follows from a formula presented in that paper for the ionization

rate, the increase in the total ionization rate is $\delta = Z^2 n_{\rm He}/n_{\rm H} = 32\%$, where $Z = 2$ (the charge of the He nucleus), $n_{\rm H} = 0.2$ cm^{-3}, and $n_{\rm He} = 0.016$ cm^{-3} [15]. Unfortunately, Cummings *et al.* [15] do not state the differences in the mean charges resulting from this increase in the ionization rate, but it would seem that they should be higher than the value of 10% we have obtained. Note that the formulas of [36] were used in [15] to calculate the reaction rates derived in a rougher approximation and giving overestimated cross sections for the corresponding reactions.

Finally, we emphasize that we did not use any model for the propagation of the anomalous CR component particles to the Earth's orbit after their acceleration at the boundary of the heliosphere. The energy and charge spectra of the ions were obtained *in situ* taking into account their subsequent stripping over the characteristic time $T_{\rm cap}$. Therefore, the total time for the transport of the particles to the observer is equal to $T_{\rm cap}$, with the density of the surrounding plasma corresponding to some average value. Taking into consideration the many specific features of the propagation of ions in interplanetary space is a more difficult problem that is beyond the scope of the present paper.

4. CONCLUSIONS

Let us summarize the main results of our analysis.

(1) We have presented an analytic model for the charge-consistent acceleration of triply charged heavy ions. This has enabled us to demonstrate qualitatively a tendency for the mean charge of the ions to increase with energy.

(2) A numerical model for the acceleration of the anomalous CR component ions by a spherical shock at the heliospheric boundary was developed based on Monte Carlo computations. This model incorporates the latest data on the cross sections of all important processes that can change the charges of ions due to their interaction with the local interstellar medium.

(3) The energy dependences of the mean charges of C, N, O, Ne, Si, S, Ar, and Fe ions near the shock at the heliospheric boundary were obtained. These dependences are influenced by the characteristic time for the residence (trapping) of particles in the region where their charges can be changed after their acceleration.

ACKNOWLEDGMENTS

This work was supported by the Russian Foundation for Basic Research (project codes 00-02-17031, 01-02-16139, and 02-02-06922 (IAU)).

REFERENCES

1. L. A. Fisk, B. Kozlovsky, and R. Ramaty, Astrophys. J. **190**, L35 (1974).
2. B. Klecker, M. C. McNab, J. B. Blake, *et al.*, Astrophys. J. **442**, L69 (1995).
3. R. A. Mewaldt, R. S. Selesnick, J. R. Cummings, *et al.*, Astrophys. J. **466**, L43 (1996).
4. B. Klecker, M. Oetliker, J. B. Blake, *et al., Proc. 25th Intl. Cosmic Ray Conf.,* **2**, 273 (1997).
5. M. Oetliker, B. Klecker, G. M. Mason, *et al., Proc. 25th Intl. Cosmic Ray Conf.,* **2**, 277 (1997).
6. B. Klecker, R. A. Mewaldt, J. W. Bieber, *et al.*, Space Sci. Rev. **83**, 259 (1998).
7. J. Geiss, G. Gloeckler, L. A. Fisk, and R. von Steiger, J. Geophys. Res. **100**, 23373 (1995).
8. V. M. Osryakov, Izv. Ross. Akad. Nauk, Ser. Fiz. **61**, 1074 (1997).
9. D. V. Reames, Astrophys. J. **518**, 473 (1999).
10. I. G. Kurganov and V. M. Osryakov, Pis'ma Astron. Zh. **17**, 177 (1991) [Sov. Astron. Lett. **17**, 77 (1991)].
11. V. M. Osryakov and M. F. Stovpyuk, Astron. Zh. **74**, 440 (1997) [Astron. Rep. **41**, 386 (1997)].
12. M. F. Stovpyuk and V. M. Ostryakov, Sol. Phys. **198**, 163 (2001).
13. J. R. Jokipii, Astrophys. J. **466**, L47 (1996).
14. M. F. Stovpyuk and V. M. Ostryakov, Adv. Space Res. **27**, 503 (2001).
15. A. C. Cummings, E. C. Stone, and C. D Steenberg, Astrophys. J. **578**, 194 (2002).
16. A. V. Bakaldin, S. A. Voronov, S. V. Koldashov, and V. P. Shevel'ko, Zh. Teor. Fiz. **70**, 17 (2000).
17. V. P. Shevelko, I. Yu. Tolstikhina, and Th. Stöhlker, Nucl. Instrum. Methods Phys. Res. B **184**, 295 (2001).
18. K. Hasselmann and G. Wibberenz, Z. Geophys. **34**, 353 (1968).
19. R. Schlickeiser, Astrophys. J. **336**, 264 (1989).
20. I. N. Toptygin, *Cosmic Rays in Interplanetary Magnetic Fields* (Nauka, Moscow, 1983) [in Russian].
21. M. Arnaud and R. Rothenflug, Astron. Astrophys., Suppl. Ser. **60**, 425 (1985).
22. A. M. Luhn and D. Hovestadt, Astrophys. J. **317**, 852 (1987).
23. M. Arnaud and J. Raymond, Astrophys. J. **398**, 394 (1992).
24. H. Tawara, Research Report NIFS-DATA-17 (Nagoya, Japan, 1992).
25. Oak Ridge National Laboratory, Atomic Data for Fusion **5**, 48 (1987).
26. M. F. Stovpyuk and V. M. Ostryakov, Astron. Zh. **80**, 374 (2003) [Astron. Rep. **47**, 343 (2003)].
27. E. G. Berezhko, V. K. Elshin, G. F. Krymskiĭ, and S. N. Petukhov, *Generation of Cosmic Rays by Shock Waves* (Nauka, Novosibirsk, 1988) [in Russian].
28. R. Lallement, Space Sci. Rev. **78**, 361 (1996).
29. M. Witte, H. Rosenbauer, M. Banaszkiewicz, and H. Fahr, Adv. Space Res. **13**, 121 (1993).
30. V. M. Ostryakov and M. F. Stovpyuk, Sol. Phys. **189**, 357 (1999).

31. V. M. Ostryakov, Yu. Yu. Kartavykh, D. Ruffolo, *et al.*, J. Geophys. Res. **105** (A12), 27315 (2000).
32. D. C. Ellison, F. C. Jones, and M. G. Baring, Astrophys. J. **512**, 403 (1999).
33. A. F. Barghouty, *Proc. 26th Intl. Cosmic Ray Conf.*, **7**, 555 (1999).
34. D. Rucinski, A. C. Cummings, G. Gloeckler, *et al.*, Space Sci. Rev. **78** (1-2), 73 (1996).
35. G. P. Zank, Space Sci. Rev. **89**, 413 (1999).
36. A. F. Barghouty, J. R. Jokipii, and R. A. Mewaldt, *In the Outer Heliosphere: The Next Frontiers*, Ed. by K. Scherer, H. Fichtner, H. J. Fahr, and E. Marsch (Pergamon, Amsterdam, 2001), p. 203.

Translated by Yu. Dumin